Abstract

Kenneth Jacobs, Development of a Diffraction Imaging Flow Cytometer for Study of Biological Cells (Under the direction of Dr. Xin-Hua Hu) Department of Physics, April 2010

Visible light interacts with biological cells primarily through elastic scattering. With coherent excitation the scattered light is coherent as well and contains much information about the cells morphology but with the notable difficulty of interpreting the complex diffraction pattern. One option is to develop by experimentation a library of diffraction image patterns with each pattern associated with some cell characteristic and without attempting a physical interpretation. To achieve this goal for rapid analysis of a large cell population, we have designed and built a diffraction imaging flow cytometer with the ability to efficiently acquire high-contrast diffraction images from individual flowing cells. A series of experimental and modeling studies have been carried out to build this instrument including fabrication of square microchannels with optical surfaces, a three fluid focusing chamber, and optical isolation of target particles. Diffraction images were acquired of six cell lines: the Jurkat cells, the Tramp C1 cells, the NALM-6 cells, the U937 cells, the B16F10 mouse melanoma cells, and the MCF-7 cells. From these preliminary image sets both the potential and the problems are apparent. Cell line images are clearly differentiable among the different cell lines in aggregate but the intra cell line variability in certain cell lines, such as the Jurkat and NALM-6 cell, may be too great for discrimination. The experiments of fluidics and chamber construction performed so far clearly indicate that the intra cell line variability can be reduced and therefore demonstrate the significant potential of the new imaging flow cytometer method to discriminate cells from diffraction images.

Development of a Diffraction Imaging Flow Cytometer for Study of Biological Cells

A Dissertation

Presented To

The Faculty of the Department of Physics

East Carolina University

In Partial Fulfillment

of the Requirements for the Degree

Doctor of Philosophy Biomedical Physics

by

Kenneth Jacobs

April, 2010

Development of a Diffraction Imaging Flow Cytometer for Study of Biological Cells

By

KENNETH JACOBS

APPROVED BY:

ADVISOR OF DISSERTATION: _____

XIN-HUA HU, PH.D

COMMITTEE MEMBER: _____

ARTHUR P. BODE, PH. D.

COMMITTEE MEMBER:_____

JAMES JOYCE, PH.D.

COMMITTEE MEMBER: _____

MARY A. FARWELL, PH.D.

COMMITTEE MEMBER: _____

ZI-WEI LIN, PH.D.

CHAIR OF PHYSICS DEPARTMENT: _____

JOHN SUTHERLAND, PH.D.

DEAN OF THE GRADUATE SCHOOL: _____

PAUL J. GEMPERLINE, PH.D.

ACKNOWLEDGEMENT

First I would like to thank Dr. Xin-Hua Hu for his patience with me and his accommodation of my shortcomings to get me through this long project. His work and steady discipline is a necessity in any undertaking like this.

I thank the ECU Physics Department for allowing me the freedom and resources to bring this project to completion.

Also I would like to thank Dr. Li Yang of Dept. of Internal Medicine, Dr. Ted Bertrand of Dept. of Internal Medicine, and Dr. Mary Farwell of Dept. of Biology for graciously supplying cell samples for testing our flow cytometer.

Finally I want to thank my children for always thinking I'm a hero. And most gratefully I thank my wife for believing I could accomplish this.

Table of Contents

Chapter 1 Introduction

In this chapter we will provide a brief review of flow cytometry related to the study of cell optics followed by a description of dissertation organization.

§1.1 Historical development of flow cytometry

Study of living biological cells often requires measurements on a large population to generate statistically significant results. In the late 1940s automated measurement and analysis of large numbers of cells was first attempted with the Coulter counter in which blood cells were passed through a capillary between intercepting electrodes [Coulter 1949]. This allows cell sizing and counting since the impedance depends on cell volume. By the early 1950s the principle of hydrodynamic focusing was applied to facilitate liquid flow and optical measurement [Crosland-Taylor 1953]. In the 1950s another approach has been investigated in which multiple cells on a glass slide were interrogated with a microscopic spectrophotometer at UV wavelengths and served as a precursor to fluorescence detection of cells in liquid flow stream. Later an effort was made to automate discernment between cells based on their nuclear size and index of refraction as biomarkers for cell malignancy [Shapiro 1985]. Further efforts, accompanying the advent of rapid computing, were undertaken to process cell data of large sample populations. Also at this time fluorescence stain of acridine orange (AO) was first used to generate and quantify cell RNA concentration [Armstrong 1956]. By the late 1960s an attempt was underway use a laser scanning microscopy method to automatically extract cellular features, such as cell and nuclear size and texture using pattern recognition analysis of the acquired images. Vibrating mirrors were used to scan a laser beam over the cells on a slide in the object plane of a microscope [Stein

1969]. Specifically, features extracted were cell and nuclear size, basophilia and fine structure based on the image texture due to the dye concentration variation. This method is also capable of extracting image patterns related to the intracellular variation in refractive index. In these capacities, a laser scanning cytometer often takes two minutes or more to scan and analyze one cell [Shapiro 1971]. Another approach that proved more practical for analyzing large cell population was the flow cytometer which capitalized on the correlation of 260nm excited fluorescence with pulse height of forward light scatter signals to differentiate between leucocytes [Melamed1990]. By the early 1970s researchers in the Los Alamos National Laboratory had applied the ink jet principle to cell sorting by charging droplets, each containing a cell, which are steered electrostatically into containers based on results of optical interrogation [Hulett 1969].

For the remainder of the last century, major development was witnessed toward multiply stained cells being interrogated sequentially by several laser beams of different wavelengths for excitation of different fluorescence signals [Curbello 1976]. Thus a combination of fluorescence detection at different wavelengths of excitation and emission targeting different proteins inside a cell generates multiple measured signals. These in turn are processed by software that identifies significant combinations of those molecular distributions related to the fluorescence signals. All the signals are integrated over an angular range with point detectors, with a speed of data acquisition and processing much faster than the cases of imaging microscopes, but carry very limited morphology information about the cells.

Image acquisition (as compared to integrated light detection) for analysis of interrogated cells has been investigated and commercialized [Ong 1987, Aptowicz 2005, Ortyn 2007]. High speed cameras and electronic tracking (time delay integration) enable image capture of fast moving cells with no motion blurring. Coupled with advanced flow chamber designed for high flow

stability this new flow cytometer method with an imaging approach acquires more information than the non-imaging detector systems of the past. Limited feature extraction algorithms have been developed to process these images [Genter 1979]. Other configurations of light detection have been developed, such as acquiring coherent scatter signals in the time domain. This generates angle-resolved measurement of light scatters instead of just the forward and side scatters [Maltsev 2000].

§1.2 Overview of cell optics study

Despite the many developments discussed above and the potential to classify cells based on their morphology, imaging of coherently scattered light signals from flowing cells and useful interpretation of the gathered data remain challenging subjects. Microscopy and current imaging flow cytometry study of biological cells seeks to determine shape, position, and composition of intracellular components through spatially resolved detection of light signals. This morphological information finds its optical basis in the spatial distribution of complex refractive index, with its imaginary part related to absorption, and fluorescence as functions of wavelength and polarization of the illuminating light. In cases where absorption and fluorescence are negligible, it is the mismatch in real refractive index that leads to scattered light as dominant signals and can be used to extract 3D morphological information if a coherent imaging method can be developed. Bright field and dark field microscopy exhibit morphology through utilization of absorption based contrast whereas phase contrast microscopy produces image contrast based on index mismatch induced phase difference. For most animal cells, the contrasts of these noncoherent imaging modalities of bright field and dark field microscopy are often insufficient for detailed structural investigations. Various dyes will lend absorptivity or fluorescence to cell

components, increasing significantly the image contrast of otherwise barely visible cellular structures under noncoherent illumination, but are invasive.

Different from conventional microscopy described above, confocal microscopy illuminates a sample with a tightly focused light and then blocks out all emitted light except that from the focal point in its detector. By scanning the focal point of the incident beam within the object plane, the produced 2D imaging can thus have a very small focal depth. A stack of the 2D image slices can be obtained by translating the sample in the direction perpendicular to the object plane which altogether yields the 3D structural information of an imaged cell. However, this method needs considerable time to develop the image stack and extracted image. In digital holographic microscopy, the interference between scattered light from a sample and a coherent reference light is detected, yielding the 3D structure if holograms are acquired at multiple angles by rotating the sample relative to the incident beam [Cheong 2009]. But this approach requires time-consuming acquisition of multiple images as well and computing intensive processing for 3D reconstruction.

Thus it remains a challenging and attractive research topic to develop rapid method based on elastic light scattering to classify cell based on their 3D morphology. It was once considered that just a few point detectors placed at several angles of scattering would provide sufficient information equivalent to that from a complete angle-resolved measurement of scatter [Salzman 1990]. However recent theoretical and experimental studies of clustered cells have shown that angle-resolved measurement of light scatter can provide much more information related to the cell morphology [Lu 2005, Brock 2006]. Other researches have shown that correlation exists between forward, side, and angle resolved scatter and cell size [Steen 1985], nuclear size [Genter 1979], organelle membrane smoothness [Wilson 2005], mitochondria swelling [Wilson

2005], mitochondria distribution [Su 2009] and intracellular distributions of refractive index [Drezek 1999, Lu 2005, Brock 2005, Brock 2006, Ding 2007].

To be able to image large numbers of cells, they must pass through a predetermined focal point relative to a microscope objective rapidly. Although this presents technical challenges, rapid, label-free, noninvasive analysis of large numbers of biological cells could be very useful. Rapidly moving cells means the imaging time must be short, requiring exposure times of 10^{-4} to10^{-6} seconds to reduce motion blurring. If side scatter is to be measured then irradiance at microscope input is diminished by up to 10^{-4} over the irradiance of forward light scatter. Therefore a sensitive light detector such as photomultiplier tube (PMT) is often used, integrating the scattered signal over a large solid angle so forward and side scatter information takes the form of a single pulse signal from each direction. The forward scatter (FS) signal irradiance depends on cell size while the side scatter (SS) signal irradiance can relate to cell granularity or gradient of intracellular refractive index. In the measurement scheme of signal integration over a solid angle, the fluorescence signals of stained cells are much more useful to detect conditions of intracellular components since they are proportional to the number of fluorophore attached to a targeted component. An improvement over the measurement of forward and side scatter is to place an array of PMT detectors in a ring around the illuminated cell, resulting in many scattered signal pulses at different scattering angles in the scattering plane. Thus more angular information is obtained than with two (perpendicular) PMT detectors but less than an image would provide.

A step further is to generate from streaming biological cells an image of scattered light in an angular range. That is the objective of this dissertation study. It entails three main difficulties. One is positioning cells accurately at the desired focal volume at low flow speed. The second is to generate high contrast diffraction images with minimal scattered light background due to the

optical interfaces around the flowing particles. And the third is to develop automated image analysis software based on certain pattern recognition algorithms for rapid cell classifications without need for computing-intensive optical modeling as an inverse scattering problem. This dissertation is aimed to solve the problems related to the first two difficulties and yield sufficient diffraction image data of different biological cells that can be used in future research to solve the last problem.

§1.3 Organization of dissertation

Chapter 2 deals with the theoretical and experimental consideration underlying the design of flow cytometers for particle positioning through fluid dynamics and image acquisition. Chapter 3 describes in detail various designs of flow cytometers developed and tested during this dissertation research and related results of fabrication processes and performance. These cytometers have the capability of producing laminar flow consisting of core and sheath fluids enclosed in a microchannel flow chamber. Chapter 4 describes a more successful submerged jet design concept of the flow chamber and validation results with polystyrene microspheres. The submerged jet design employs a water filled flow chamber into which the sheath and core fluids are coaxially jetted to position the flowing cells by the core fluid and permit a background free environment for diffraction imaging. Chapter 5 presents results with spheres and biological cells and possible classification of some cell characteristics. Chapter 6 summarizes this dissertation research with a discussion on future development plans.

Chapter 2 Background

This chapter will discuss the theoretical and experimental development in fluidics, optics, and data analysis related to the diffraction imaging flow cytometer developed through this dissertation study.

§2.1 The principle of flow cytometry

In a typical flow cytometer individual cells pass through an illumination zone in single file, usually at a rate up to 5000 cells per second, and appropriate detectors measure scattered and fluorescence light signals in the form of pulsed signals [Shapiro, Melamed]. Pulse magnitudes are then sorted by a multichannel analyzer, permitting the display of histograms of the number of cells having a specific pulse height versus the values of height. The utility of the histogram data is in quantifying statistically some cell characteristic versus its prevalence in the sample [Maddox 1994]. Additionally the angular dependence of scattered signal provides further information on the structure of the cells. Appropriate fluorophores may be added to the cell suspension to bind to particular molecules such as DNA, RNA, or proteins for determination of their concentrations or conditions. Other fluorescence reagents can be used to probe various biochemical processes which include fluorogenic substrates showing distributions in enzymatic activity; compounds for changing their property as a function of pH; or antibodies tagged with a fluorescent probe [Davey 1996]. The histograms may be presented as multivariate data sets with, for example, scattering versus fluorescence from both a DNA stain and a protein stain. Thus conclusions can be obtained about the distribution of several properties among the cells in the population as a whole.

There are three main components in a flow cytometer: a fluidic means to bring a cell suspension into a fast moving fluid column that is ideally only one cell wide; an optical system to provide one or more light beams for excitation of the flowing cells and detect the scattered and/or fluorescence light signals; and a data analysis module to interpret data for cell classification and sorting if needed. The flow cytometer developed in this study requires several improvements over state-of-the-art instruments. One is that speed of cells needs to be several orders of magnitude slower to reduce motion blurring in image data while maintaining a stable stream of laminar flow. Secondly sample flow must be either further than usual from the nearest optically interfering surfaces or else a method of refractive index matching implemented to prevent undesired scattered light as imaging noise. The light collection optics must be configured to allow easy transition from system alignment under non coherent illumination to data acquisition under coherent illumination for diffraction imaging. The information available or encoded in the particles' scattered light must appear at the detector in an undistorted or at least consistent mapping and then the detector must be sufficiently sensitive and fast. And finally the utility of the diffraction image depends upon correlating image with cell morphology.

A number of these technical requirements have been investigated previously [Seger 1977, Genter 1979, Stovel 1978, Pinkel 1982] but for our research purpose integrating these components for study of diffraction imaging remains a significant challenge. Several examples can be mentioned: hydrodynamic focusing with particle velocities less than 20mm/s have been accomplished using an integrated reservoir and flow cell [Ludlow 1978]; quartz flow chambers having a microchannel with optically flat surfaces, inside and outside, have given relatively good image data from scattered signals received by a light intensified CCD camera [Neukammer 2003]. The rapidly developing field of microfluidics has enabled flow cytometry functions to be

performed on a disposable device complete with all fluidics. For example the excitation light beam can be brought in through chip-integrated waveguides, the small angle scatter can be detected with several other waveguides, and side scatter detected by a viewing microscope [Kummrow 2009]. Camera technology, using time delay integration or an intensified ICCD, has advanced to enable either high speed image capture or low light level with long exposure time [Ortyn 2007]. We will consider each of the discussed design challenges in this chapter followed with our solutions in Chapters 3 and 4, and results in Chapters 5.

§2.2 Fluid dynamics of flow cytometry

The purpose of maintaining a laminar flow condition in a flow cytometer is to force the particles without clogging into a single file motion for optical interrogation. Furthermore they must move at sufficiently high speed for high throughput to a few thousand cells per second. The positioning of the particle at interrogation point needs to be accurate in all three spatial dimensions with an error desirably less than 50μm. This last requirement is particularly critical for this study since an image is to be acquired. In addition, and unlike integrated light measurements or non-coherent imaging, it is not acceptable to have index-mismatched interfaces near the imaged particle. This is because the information to be extracted from diffraction image data only relates to coherently scattered light from the illuminated cell and light scatters from extracellular interfaces comprise to noise which can be very strong if the curvatures of the interfaces are large.

A flow is either turbulent or laminar. A particle suspension injected into a turbulent flow will diffuse progressively in complex streamlines and eventually lead to an even distribution of the particles over the entire volume of flow. By comparison a laminar flow is characterized by non-

mixing of streamlines such that in a long tube, in which laminar flow has been established, a thin line of particle carrying flow, which I term flow stream, will remain stable without mixing. As the flow speed or tube dimensions increase or as viscosity decreases the tendency toward turbulent flow increases. The transition is characterized by the Reynolds number Re defined as

$$\mathrm{Re} = \frac{d \cdot \rho \cdot u}{\mu} = \frac{d \cdot u}{\nu}. \qquad (2.1)$$

in which d is the characteristic size of the channel, ρ is fluid's density, μ is dynamic viscosity, $\nu = \mu/\rho$ is kinematic viscosity, and u is flow speed. When the dimensionless Reynolds number Re falls below a critical value of about 2300 the flow will remain laminar since the viscous forces, proportional to $\mu(u)/d^2$, will dominate the inertial forces proportional to $\rho(u^2)/d$.

According to the potential flow theory [Pnueli 1992] the flow velocity vector field **u** can be described by streamlines which are orthogonal to equipotential lines. The scalar velocity potential φ is defined by $\mathbf{u} = \nabla\varphi$ since the curl of a gradient is zero for a laminar flow. For incompressible flow, $\nabla \cdot \mathbf{u} = 0$ and so the scalar potential φ must also satisfy Laplace's equation, $\nabla^2 \varphi = 0$. Thus, an accelerating, incompressible fluid flow inside a nozzle, as shown in Fig. 2-4, can be represented by a set of focused streamlines perpendicular to the equipotential surfaces. Let's consider two cross sections in a tube with area A_i and pressure p_i of same height with i=1 and 2. The conservation laws of mass and energy give, respectively,

$$\begin{aligned} u_1 A_1 &= u_2 A_2 \\ \Delta p &= \frac{\rho}{2} \left(A_1 u_1^2 - A_2 u_2^2 \right) \end{aligned} \qquad (2.2)$$

with the second equation also known as Bernoulli's equation without the gravity terms.

To consider momentum conservation we need to imagine a small cube of fluid with dimensions of Δx, Δy, Δz, and with six outward surface normals denoted by the unit vectors of $\pm\mathbf{i}$, $\pm\mathbf{j}$, $\pm\mathbf{k}$ [Pnueli 1992]**.** Newton's second law for the cube can be written as

$$m\mathbf{a} = \mathbf{G} + \mathbf{S} \tag{2.3}$$

where **G** is the body mass force and **S** is the total contact force on its respective surfaces. The stress on any surface will be represented by T_{ij} in which the first subscript i denotes which of the six surfaces is acted upon by corresponding stress vector, and j indicates its component direction. Thus a force acting on the surface of normal **i** is given by

$$\begin{aligned} \mathbf{F}_x &= \mathbf{T}_x \Delta y \Delta z \\ &= \left[\mathbf{i}T_{xx} + \mathbf{j}T_{xy} + \mathbf{k}T_{xz} \right] \Delta y \Delta z \end{aligned} \tag{2.4}$$

In this case T_{xx} is the normal stress component along the surface normal direction and the other two stress components are shear forces in y and z directions. The sum of all forces in the x direction due to all six surfaces will be

$$S_x = \left[T_{xx} \Big|_{x+\Delta x} - T_{xx} \Big|_x \right] \Delta y \Delta z + \left[T_{yx} \Big|_{y+\Delta y} - T_{yx} \Big|_y \right] \Delta x \Delta z + \left[T_{zx} \Big|_{z+\Delta z} - T_{zx} \Big|_z \right] \Delta x \Delta y \tag{2.5}$$

Here the first subscript indicates the normal direction of the surface a force acts upon and the second subscript indicates the component of that force. The subscript following the vertical bar indicates the surface (position) in question, for example the [x] and [x + Δx] positions are opposite each other and normal to x axis. From equation (2.3), and concerning only a general body force per unit mass, g_x, acting on the cube,

$$\begin{aligned} G_x &= g_x \rho \Delta x \Delta y \Delta z \\ ma_x &= a_x \rho \Delta x \Delta y \Delta z \end{aligned} \tag{2.6}$$

Combining surface and body forces in the x direction in the limit as $\Delta x \rightarrow 0$, $\Delta \rightarrow 0$, $\Delta z \rightarrow 0$ gives the x components of forces and rate of momentum change as

$$\rho a_x = \rho g_x + \frac{\partial T_{xx}}{\partial x} + \frac{\partial T_{yx}}{\partial y} + \frac{\partial T_{zx}}{\partial z} \tag{2.7}$$

Similar equations can be written for the other two components of the acceleration.

2.2.1 Poiseuille flow

The velocity distribution in a simple confined flow of an incompressible fluid of dynamic viscosity μ, is schematically shown in Fig. 2-1 [Pnueli 1992]. Here we consider the case of laminar flow streaming in the positive y direction under uniform pressure gradient, $\Delta P/\Delta y$, through a straight channel of radius R with a fluid speed profile given by u(r). The channel is considered cylindrically symmetric without obstructions and sufficiently long that dynamic equilibrium has been reached. Equilibrium in the speed profile is reached after the tube length exceeds R(0.058)(Re) where Re is Reynolds number [Schiller 1922]. Consider a cylindrical fluid element of length ΔL and radius r and centered in the stream as in Fig. 2-1. The longitudinal pressure difference, ΔP_L, between top and bottom surfaces, ignoring gravity, is therefore

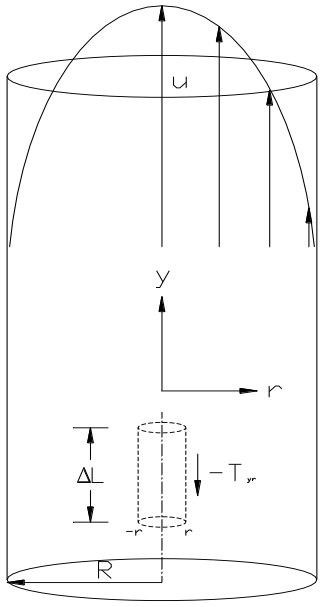

Fig. 2-1 Simple Poiseuille flow in cylinder of radius R moving in the +y direction with speed u(r). A fluid element of radius r and length ΔL experiences shear force $-T_{ry}$.

$$\Delta P_L = \frac{\Delta P}{\Delta y} \Delta L \tag{2.8}$$

so the net force resulting from the differential pressure is

$$F_P = \Delta P_L \pi r^2 = -\frac{\Delta P}{\Delta y} \Delta L \pi r^2 \tag{2.9}$$

with $\Delta P/\Delta y$ negative since pressure decreases as y increases. This force is opposed by a shear force of $-T_{ry}(2\pi r \Delta L)$, which is the viscous drag on the cylinder. Equating these two forces yields

$$T_{ry} = -\left(-\frac{\Delta P}{\Delta y} \right) \frac{r}{2} \tag{2.10}$$

and using Newton's law of viscous flow gives

$$\mu \frac{du}{dr} = -\frac{-\Delta P}{\Delta y} \frac{r}{2} \tag{2.11}$$

Subject to the speed boundary condition at channel wall of u(R) =0, the above equation can be solved to find

$$u(r) = \frac{-\Delta P}{\Delta y} \frac{R^2}{4\mu} \left(1 - \left(\frac{r}{R} \right)^2 \right) \tag{2.12}$$

Therefore laminar flow through a circular channel has a parabolic speed profile starting from zero at walls and reaching the maximum speed $u_{\max} = \frac{-\Delta P}{\Delta y} \frac{R^2}{4\mu} = 2\bar{u}$ at the center with curvature inversely proportional to viscosity. The maximum speed, at center, is twice the average speed ū, and this profile characterizes what is called Poiseuille flow [Pnueli 1992].

Two phase Poiseuille flow

Next consider a two fluid, coaxial, steady state, laminar flow as shown in Fig. 2-2 in which the outer sheath fluid has a viscosity of $\mu_{Sh} = k\mu$, k is core to sheath viscosity ratio, and the water core has μ as its viscosity. The absolute value of the water viscosity μ is 1.0 centipoise or the dynamic viscosity $\nu=\mu/\rho$ is 0.001 stokes. Assume the two liquids are in laminar flow and do not mix such that velocities at their interface can be considered equal. The volume flow ratios of core flow Q_c to sheath flow Q_{sh} depends on the ratios of their respective radial dimensions r_c and r_{sh}. We seek to express the radius ratio $w = \frac{r_c}{r_{sh}}$ as a function of flow rate ratio $z = \frac{Q_c}{Q_{sh}}$.

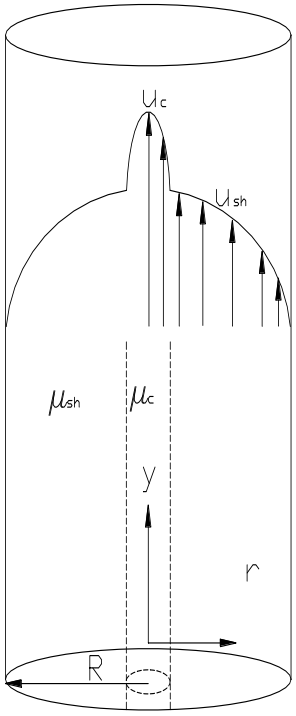

Fig. 2-2 Flow of two dissimilar coaxial fluids with the outer fluid of higher viscosity. Core fluid has speed u_c and viscosity μ_c and sheath u_{sh} and viscosity μ_{sh}.

Using $\mu_{Sh}= k\ \mu_{core}= k\mu$, the sheath speed from Eq.(2.12) will be

$$u_{sh}(r) = \frac{R^2}{4\mu k}\left(\frac{-\Delta p}{\Delta y}\right)\left(1-\left(\frac{r}{R}\right)^2\right). \qquad (2.13)$$

Integrating this speed over a region from r_c to R gives the total sheath volume flow rate as

$$Q_{sh} = \frac{\pi R^4}{8\mu k}\left(\frac{-\Delta p}{\Delta y}\right)\left[1-2\left(\frac{r_c}{R}\right)^2+\left(\frac{r_c}{R}\right)^4\right] \qquad (2.14)$$

To determine the flow rate of the core assume $u_{sh}(r_c) = u_c(r_c)$ which means the differential speed at the interface between core and sheath is zero. Core speed will be of the form

$$u_c(r_c) = -\frac{r_c^2}{4\mu}\left(\frac{-\Delta p}{\Delta y}\right) + C = u_{sh} \quad r_c \quad = \frac{R^2}{4\mu k}\left(\frac{-\Delta p}{\Delta y}\right)\left[1 - \left(\frac{r_c}{R}\right)^2\right] \tag{2.15}$$

with C as an integration constant. Calculating the speed at the fluids interface from the sheath speed at that point and solving for C

$$u_c(r) = -\left(\frac{-\Delta p}{\Delta y}\right)\frac{r^2}{4\mu} + \left(\frac{-\Delta p}{\Delta y}\right)\frac{R^2}{4\mu}\left\{\frac{1}{k} + \left(\frac{k-1}{k}\right)\left(\frac{r_c}{R}\right)^2\right\}. \tag{2.16}$$

Total core volume flow, Q_C, is obtained by integrating the speed over cross-sectional area from r = 0 to r = r_c

$$Q_c = \int_{r=0}^{r=r_c} 2\pi r \; u(r)\, dr \tag{2.17}$$

which provides

$$Q_c = \frac{\pi R^4}{8\mu k}\left(\frac{-\Delta p}{\Delta y}\right)\left\{2\left(\frac{r_c}{R}\right)^2 + \left[2 \;\; k-1 \;\; -1\right]\left(\frac{r_c}{R}\right)^4\right\}. \tag{2.18}$$

The flow rate ratio can now be determined as a function of radius ratio as

$$z = \frac{Q_c}{Q_{sh}} = \frac{\frac{\pi R^4}{8\mu k}\left(\frac{-\Delta p}{\Delta y}\right)\left\{2\left(\frac{r_c}{R}\right)^2 + \left[2 \;\; k-1 \;\; -1\right]\left(\frac{r_c}{R}\right)^4\right\}}{\frac{\pi R^4}{8\mu k}\left(\frac{-\Delta p}{\Delta y}\right)\left[1 - 2\left(\frac{r_c}{R}\right)^2 + \left(\frac{r_c}{R}\right)^4\right]}. \tag{2.19}$$

The inverted function is more useful, giving core radius as a function of core-sheath flow rate ratio z

$$w = \frac{r_c}{R} = \sqrt{\frac{1+z-\sqrt{1-z+3kz}}{3-3k+z}}\,. \qquad (2.20)$$

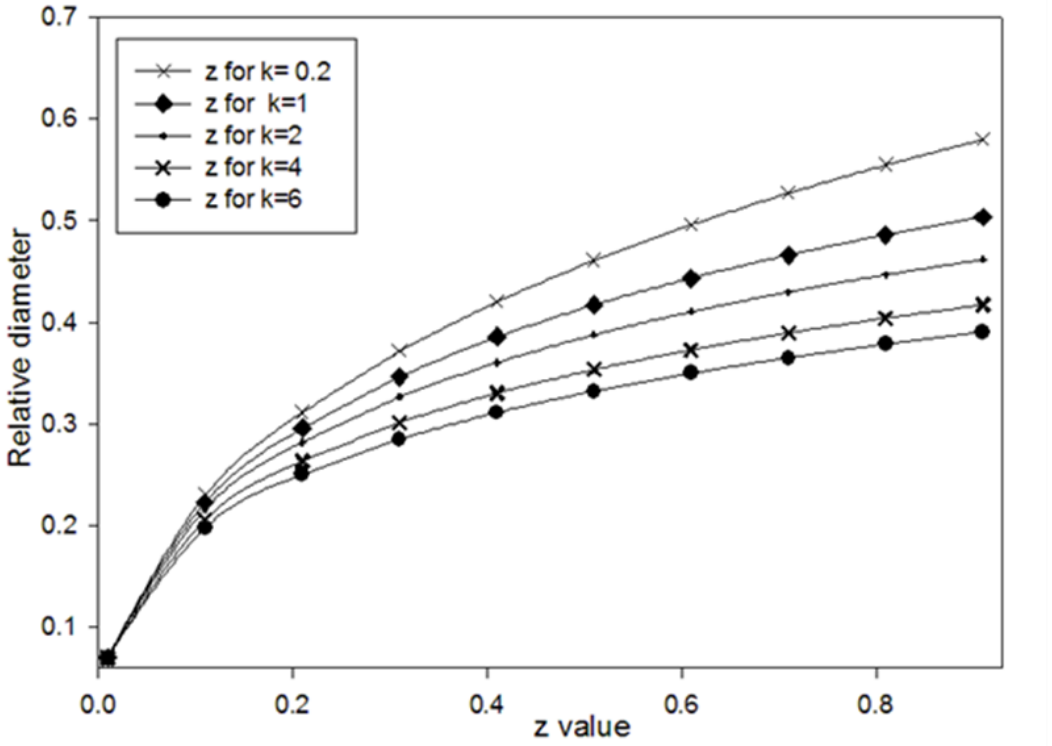

Fig. 2-3 Predicted core radius (normalized to channel radius) versus flow ratio at different values of relative viscosity k.

Fig. 2-3 plots core radius as a function of flow ratio for viscosity values of k from 0.2 to 6.0, showing that as sheath relative viscosity increases the core is reduced in diameter and increased in speed. The maximum k value of six is chosen because it is the viscosity of a selected water-glycerol mixed liquid used for sheath fluid in this study. The use of this liquid allows the match of its refractive index to that of the PDMS made flow chamber wall, which greatly reduce light scattering at the interface. Eq. (2.20) and data in Fig. 2-3 can enable one to estimate the resultant

core diameter from the values of viscosity and flow rate ratio. This diameter must be comparable to diameter of particles being confined by hydrodynamic focusing. Notice that for higher sheath viscosity the core will become smaller and hence propelled at higher flow speeds.

Flow profile in short or tapered pipes: plug flow

Poiseuille flow in a channel is the steady state result only after flow profiles have reached dynamic equilibrium. If the speed profile is square shaped at the entrance of a tube, then the parabolic profile will only develop progressively after a distance of R(0.058)Re [Schiller 1922]. However, it has been shown that the velocity profile in a tube is highly sensitive to convergence of the tubes diameter, such that as little as .001 radius to length ratio results in marked flattening of the parabolic shape [Prandtl 1934]. The nozzles used in this study are of dimensions such that the flow completes transitions from square to parabolic velocity profiles for lower flow speed values used but remains square for higher flow speeds.

2.2.2 Hydrodynamic focusing and jets

Consider two fluids A and B with flow rates of Q_C and Q_{Sh}, respectively, undergoing acceleration by being coaxially injected into a converging tube C, as shown in Fig. 2-4. If the convergent tube is conical then, because fluid is incompressible, velocity as a function of distance s from its convergence point (apex) will be

$$v\ s\ = \frac{-Q}{2\pi s^2(1-\cos\theta)} \tag{2.21}$$

where $Q=Q_{Sh}+Q_C$ is the total flow rate and θ is the cones half angle. The acceleration of the fluid elements as a function of distance towards apex is [Van Dilla 2000]

$$a = \frac{dv}{dt} = -\frac{2}{s^5}\left[\frac{Q}{2\pi\ 1-\cos\theta}\right]^2 \tag{2.22}$$

The velocity gradient will be

$$\frac{dv}{ds} = -\frac{Q}{\pi s^3\ 1-\cos\theta} \tag{2.23}$$

Typical values used in our study of flow nozzles are the outside tube diameter of 8mm and inner tube diameter of 80 um with a convergence distance of 10mm and flow rate of Q_{Sh}= 1 uL/s and Q_C = 0.03 uL/s. From these values the highest acceleration near the apex will be about 500m/s^2. The velocity gradient at the same location will be (0.04m/s)/m at a position about 20 um inside the nozzles peak acceleration range. Stretching of cells due to velocity gradient therefore will be negligible in above example, which is typical for flow conditions in this study. Velocity inside nozzle exit will be less than 50 mm/s. These values are 100 to 1000 times less, than those of typical flow cytometers because of constraints for low flow speeds to allow blur-free image acquisition.

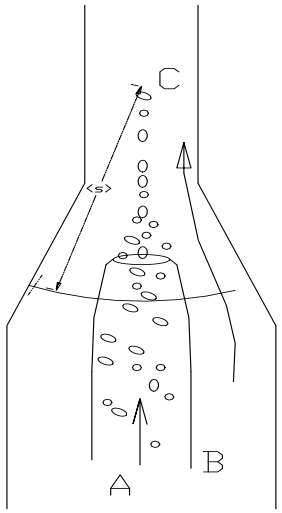

Fig. 2-4 Acceleration of sample particles by sheath in convergence zone of radius s as measured from apex C. Core fluid A is accelerated by sheath fluid B.

Submerged jet calculation

The theoretical behavior of a submerged laminar jet of a viscous, incompressible fluid has been worked out by Schlichting [1951]. It is based on the simplifying assumption that the jet originates from a point source with infinite speed. If the point of origin of the infinite flow is set

inside the actual nozzle upstream a distance y^o from the exit, then experimental agreement with the model can be realized. The value of y^o has been determined empirically as $y^o = 0.216(Re)(a)$ in which Re is Reynolds number and a is nozzle radius [Andrade 1937]

In this case the jet speed u as a function of axial travel $y' = y^o + y$ and radial distance, r, off of the y axis is given by

$$u\ \ y', r\ = A\frac{1}{1+B(r)^{2\ \ 2}} \tag{2.24}$$

where

$$A = \frac{3J}{8\pi\rho\nu y'} \tag{2.25}$$

$$B = \frac{3J}{64\pi\rho\nu^2(y')^2}\ . \tag{2.26}$$

For the above equations, J is the jet momentum transfer per unit time through a plane perpendicular to the y axis, ρ is density in g/mL^3 and ν is kinetic viscosity in Stokes. This model which has good agreement except very close to the nozzle, considers that momentum is conserved between primary and entrained jets.

If the origin, defined as the location with $\bar{u} \to \infty$, of the jet is assigned to a point y^o upstream from the actual jet exit, as presented in Fig. 2-5, then some theoretical speed flow lines are eliminated as nonphysical due to their interference with the nozzle wall. The first flow line which intersects the top edge of the physical nozzle becomes the first real flow line. At this point all moving fluid will have its origin as the jetting fluid.

However, as can be seen in Fig. 2-5 the jet slows in an inverse ratio to its travel distance along the y axis and progressively drags more of the surrounding static fluid along its path. The original jetting fluid is primary jet and surrounding accelerated fluid is entrained jet. In this model momentum is considered conserved within the primary and entrained jets, which agrees well with experimental observation except the part of flow very close to nozzle exit. For a given volume flow rate Q at input the momentum transfer rate J_s at the nozzle exit will be

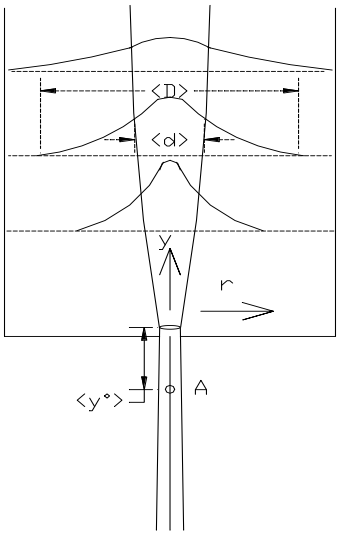

Fig. 2-5 Schematic of flow lines for submerged jet of radius r exiting nozzle at y = 0 upward into a static fluid filled chamber. At point A, $y = -y^o$ and u_y = infinity. Two diameters characterize jet: d is of primary fluid and D is primary plus entrained static fluid.

$$J_S = \frac{\rho Q^2}{\pi a^2} = \pi \nu^2 (\mathrm{Re})^2 \qquad (2.27)$$

In this case the Reynolds number, Re = ū(a/ν), indicates the ratio between dynamic and viscous forces in a fluid. The average speed is ū, a is a characteristic dimension of the pipe, and ν is kinetic viscosity. J_S is the momentum calculated if flow profile at nozzle is assumed to be of a square velocity profile, which becomes $J_P = 4/3\pi\nu^2R^2$ for a parabolic velocity profile. Nozzle shape and length determine whether velocity profile is square or parabolic which in turn affects the velocity profile downstream from the nozzle exit.

It follows therefore that some of the downstream jet is derived from the surrounding static fluid. So there will be two jetting fluids; primary, A (from injector tube), and entrained, C; and two diameters with d as the diameter of the primary fluid jet and d' as diameter of both A and C; describing the stream as in Fig. 2-6. If the primary fluid is dyed or of different refractive index from static fluid, then its interface will be visible and its diameter d can be measured.

Furthermore, if the flow is sufficiently fast, then the interface can become visible because of the density fluctuation between static and moving fluids so d' can be measured.

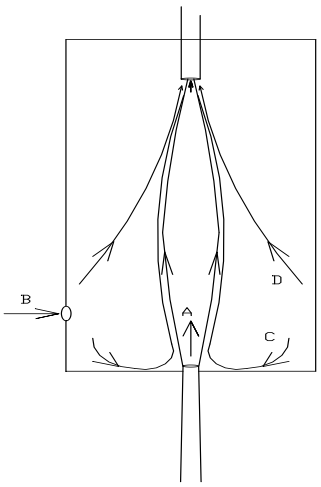

Fig. 2-6 Recirculation flow lines for jet into a static chamber having a single exit orifice. A is primary jet fluid of diameter d. C is entrained fluid. The combination of A and C is of a larger diameter d'. B serves a sheath fluid to confine jet.

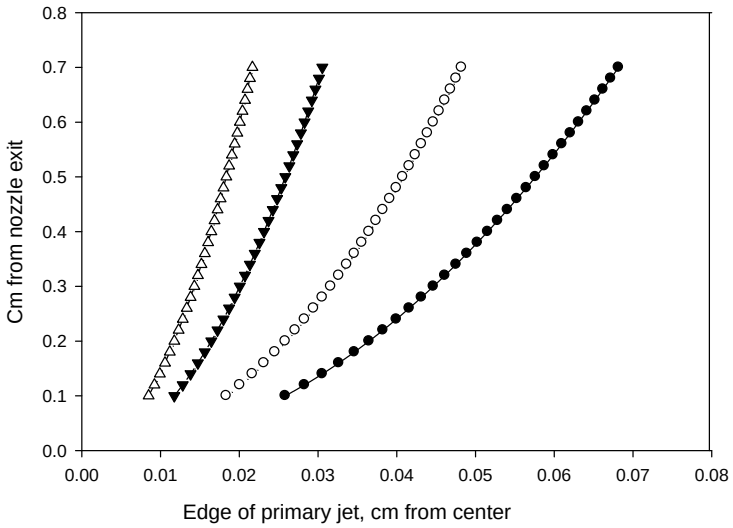

Fig. 2-7 Theoretical plot of primary submerged jet silhouettes (showing just right half side of jet) at different flow rates calculated from Eq. (2.29) and using an 80μm nozzle.

The transfer of momentum from jet to surrounding chamber fluid causes the maximum speed to diminish inversely with y'. Therefore, the flow rate Q of primary fluid remains constant while its momentum decreases although the collective momentum transfer J across a perpendicular plane of all fluids remains constant. We seek the flow speed profile as a function of y, Q, d' or d and also the core fluid diameter. This enables us to obtain knowledge about the particles speed and its confinement within both the microscope objectives depth of field and also within its field of view (FOV).

Because the flow concerned here is laminar, the total original flow Q can be related to speed profile u(r) as discussed before. So it is possible to calculate diameter d as a function of y' from Eq. (2.20)

$$Q = \int_{r=0}^{r=d/2} 2\pi r \;\; u(r)\; dr = \pi \frac{A}{B}\left[1 - \frac{1}{1 + B \;\; d/2 \;^2}\right] \tag{2.28}$$

or

$$d = 2\sqrt{\frac{\pi A}{\pi AB - QB^2} - \frac{1}{B}} \tag{2.29}$$

Fig. 2-6 shows the various sources of flow in the flow chamber and their interactions. Sheath input at B will focus jet at the chambers exit nozzle by competing with nozzle primary flow A for cross section. The streamlines for the primary flow are graphed for typical values in Fig. 2-7 using Eq. (2.29). At very low velocities, such as the cases concerned in this study, the jet expands rapidly upon entering the static environment.

2.2.3 Review of experimental study of flow chamber fluidics

The theoretical considerations discussed in the previous sections can be used to guide the experimental design and development of flow chambers used for flow cytometry. However, for the most part the theory has followed, not preceded, the technological advances. This is because governing equations for a submerged, two phase jet require knowledge of the position of interface between each laminar flow phase [Richards 1994]. Different approximations have been studied and solutions must be obtained numerically. Also accurate measurement of complete flow field speed, position, and direction is difficult. To my knowledge there is no theoretical analysis for a two phase jet injected into static chamber and exiting through nozzle.

Therefore most development efforts on flow chambers have been a mixture of theoretical modeling and empirical results. Fig. 2-9 shows some of the major changes in flow chamber design and appear almost identical though in performance there are important differences. Fig. 2-9A is the most common and simple design in which the core flow stream undergoes rapid acceleration in nozzle with associated streamlines as depicted in the uppermost section of Fig. 2-8. It is possible for core flow stream to change so rapidly at the injector tip that instabilities result. Referring to Fig. 2-9A after focusing by the nozzle the combined streams of sheath and core exit through an orifice with the core confined to a diameter of a little over that of single particles. Optical scattering occurs at the air-fluid interface which means no optical surfaces interfere but the flow stream itself is a cylindrical lens, requiring an obscuration bar in the laser plane.

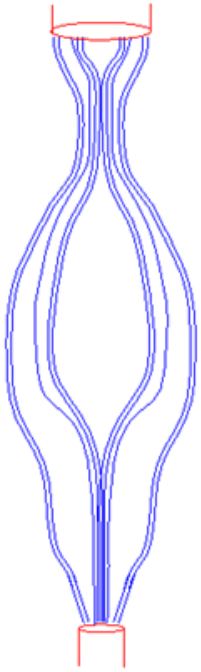

Fig. 2-8 Streamlines resulting from various tube, nozzle, and orifice configurations. At the top, flow lines are focused down and the speed is increased. In middle section the stream expands and at bottom of diagram the exit vortex focuses further.

In Fig. 2-9B a focused stream remains encased in a square flow channel with flat inner and outer walls. Thus the excitation beam and subsequent scatter do not undergo distortions due to large-angle scattering, except specular reflections, as in the case of a cylindrical stream in air. However, sorting particles is more difficult, and channel walls can still cause reflections since the flow cell is quartz. These reflections are tolerable for angularly integrating detectors but a larger problem for imaging detection.

Fig. 2-9C is a design described in [Mullaney 1969]. The nearby channel walls at interrogation point have been eliminated. Instead the focused sheath-sample combined stream is

jetted into a chamber filled with static fluid and then the jet continues on to a small exit orifice. Since the chamber walls are several millimeters from excitation beam and flat, scattering near the flowing particles is eliminated. This comes at a price. The focused jet passing into chamber becomes defocused by friction and momentum exchange with surrounding fluid. This expansion of streamlines as shown in the middle section of Fig. 2-8 reduces positional accuracy of the flowing particles. The expansion increases with slower flow and results in imaged particles being randomly positioned relative to the objective's focal plane and field-of-view. For imaging detection, as opposed to integrating detection, this can be a major problem. However, there is a second focusing involved in this design generated by the exit nozzle. The bottom part of Fig. 2-8 illustrates that vortex focusing not only reduces stream diameter but anchors it from drift which occurs as a result of the large gap between entrance and exit. Most importantly the vortex focusing can be used to further contract the core stream even smaller than the diameter achieved by focus nozzle.

The latter was the concept of Fig. 2-9D, [Crosland-Taylor 1953]. It is a variation of 2-9C and involves two significant differences. Instead of a cone shaped nozzle, the sheath focuses by surrounding core in the non-confined chamber, so that acceleration of core flow stream takes place by momentum exchange but not by pressure (since nozzle walls are absent). This results in a milder focus but there are no optically interfering nozzle walls that stands out as an advantage. The second significant difference is placement of particle interrogation point closer to exit tube. This reaps a benefit of increased focus of the core flow stream. However the design's, limitation is in the reflecting surface of the exit nozzle. Through experiment, we found that the closest distance of the interrogation point from the exit tube without light interference is several hundred micrometers from the tube.

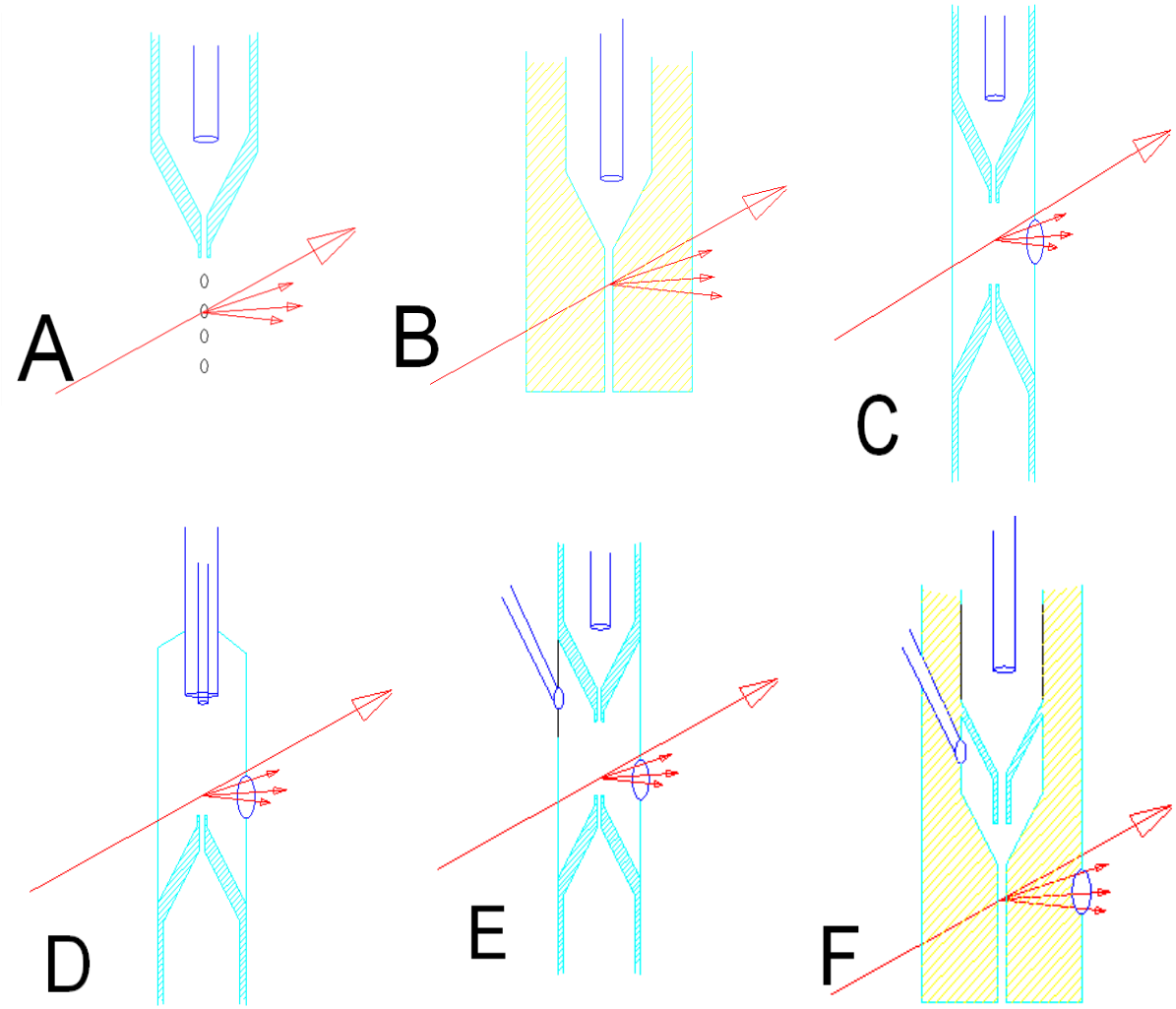

Fig. 2-9 Progression of flow cell designs over several decades. In each picture laser excitation enters flow cell from left side in diagrams and scatters light off a focused particle stream entering from above, with sample stream injected by the smaller tube. Diagram A is sample core injected by ~200um needle into accelerating sheath flow field, passed through ~ 80um orifice into air for laser excitation. In B the combined streams remain inside a channel, usually quartz, of square cross section for excitation and viewing. In C the combined and focused streams are jetted into a larger, ported and fluid filled chamber and, after excitation, stream leaves through small orifice. E is the same as D except a third sheath fluid is injected into viewing chamber with all three fluids exiting though exit orifice. F is two cascaded focus nozzles.

Schuette modified the design of Mullaney et al. by adding a second sheath injected into chamber, as shown in Fig. 9E [Schuette 1984]. The result is more fluid leaving exit tube, compressing and accelerating core to a smaller diameter and doing so at a position further from

exit surfaces. This is termed as the three fluid hydrodynamic focusing or cascaded focusing. This variation was applied in a microfluidic chip design displayed in Fig. 9F [Kummrow 2009]. The advantage of cascaded focusing concerns flow instabilities resulting from too high of a ratio, γ, between sheath speed and core speed.

All of the above design configurations are relevant to this study. We can summarize the requirements for diffraction imaging of cells as: low speed flow for imaging camera to reduce motion blurring; low laser irradiance for avoiding cell damage; no index-mismatched interfaces around flowing particles to generate images with high contrast; low drift and high stability of core positioning because diffraction image pattern vary with focus and position of the incident light beam relative to the particles. In the experimental results section these considerations will be applied to our design of flow chambers and fluid control unit.

§2.3 Light scattering by a particle

Light scattering by small particles is very complex subject and often modeled by various approximations according to different needs and precision related to measurements. Scattering is a result of the variations of refractive index within the particle and from its hosting medium. When a light beam of electromagnetic waves strikes a particle, the excited molecules insides the particle can be represented as a phased array of a large number of induced electric dipoles, as shown in Fig. 2-10. The oscillating electromagnetic field of the incident light drives the dipoles

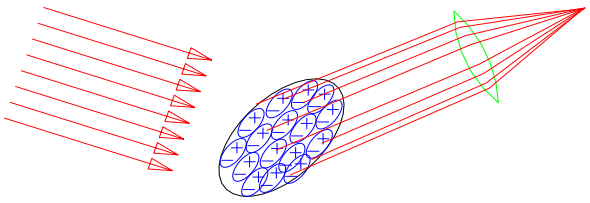

Fig. 2-10 Incident wavefront from left generates a scattered wave which is the phased sum of waves from each dipole.

to radiate and their phased sum is the resultant electromagnetic fields of scattered light. The phased relation among the fields by the molecular dipoles in turn depends on their relative positions and the scattering angles. As a consequence, the scattered light irradiance will change as a function of the scattering angles in space to form characteristic fringe patterns that can be measured as diffraction images.

The simple case of only two possible scatter directions, forward and backward, is shown in Fig. 2-11. Only in the forward direction will re-radiation from any two dipoles be in phase. Furthermore, as the number of dipoles in the particle increases (particle size), their combined forward scatter irradiance increases rapidly. Calculations indicate that the forward scatter increases approximately as the square of the volume [Melamed 1990].

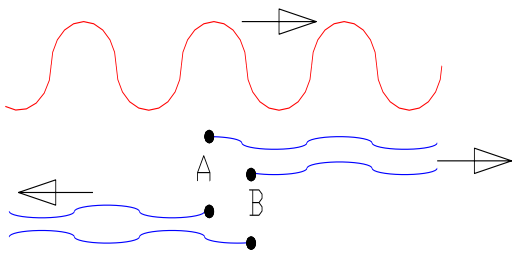

Fig. 2-11 Depiction of wave scatter by particles A and B. Top wave is incident illumination and dipoles A and B reradiate in all directions. For two dipoles of arbitrary position, only in the forward direction will their phases be the same.

At other scattering angles the phased sum from the radiating dipoles will change according to the angle values, generating maxima and minima in the scattering light irradiance distribution as the scattering pattern. It can also be shown that as the particle size increases the number of fringes also increases. If the number of dipoles is kept constant but the shape is changed then the phased sum must change. Hence the resultant scattering pattern must change, but in a complicated way that is very difficult to model. Fig. 4-17, for example, is an image we made of the scatter patterns resulting from a perfect sphere and from a dented sphere, the latter still having some similar fringes as the perfect sphere.

Despite the modeling difficulty, some conclusions can be drawn. The forward scatter wavelets from all dipoles are always in phase independent of their relative positions. So forward

scatter will not contain information about relative positions or internal structure, and scatters far from forward contain much more information on internal structure. As a result, a changed orientation of a particle relative to the incident direction of a light beam will change its scattering pattern. A biological cell has small variations of relative refractive index throughout its volume due to the changing polarizability of its dipoles. Since relative refractive index is close to unity among all of cell components for a cell immersed in a host medium of water or an aqueous solution, biological particles are considered weakly scattering.

2.3.1 Mathematical description of scattering

Consider a particle illuminated by coherent light along the z-axis as shown in Fig. 2-12. A detector at the point **r** from origin and of coordinates x, y, z, receives scattered light along a direction indicated by a unit vector $\mathbf{e}_r$. The scatter plane is defined by $\mathbf{e}_z$ and $\mathbf{e}_r$. The electric field $\mathbf{E}$ is resolved into components as the parallel component $E_{//}\mathbf{e}_{//}$ and perpendicular component $E_{\perp}\mathbf{e}_{\perp}$ relative to the scattering plane.

The incident electric field vector and corresponding irradiance are therefore given by following, respectively,

$$\begin{aligned} \mathbf{E}_i &= E_{//i}\mathbf{e}_{//i} + E_{\perp i}\mathbf{e}_{\perp i} \\ \mathbf{I}_i &= \left\langle E_{//i}E_{//i}^{*} + E_{\perp i}E_{\perp i}^{*} \right\rangle \end{aligned} \tag{2.30}$$

where the angle bracket <…> indicate time averaging. The electric field of the scattered light can also be resolved into two components of $\mathbf{e}_{//s}$ and $\mathbf{e}_{\perp s}$

$$\mathbf{E}_s = E_{//s}\mathbf{e}_{//s} + E_{\perp s}\mathbf{e}_{\perp s} \tag{2.31}$$

The linear relationship between the incident and scattered electric field components can be expressed by a 2x2 amplitude matrix which describes the scatterer's effect

$$\begin{bmatrix} E_{//s} \\ E_{\perp s} \end{bmatrix} = \frac{e^{ik(r-z)}}{-ikr} \begin{bmatrix} S_2 & S_3 \\ S_4 & S_1 \end{bmatrix} \begin{bmatrix} E_{//s} \\ E_{\perp s} \end{bmatrix} \qquad (2.32)$$

where $k=2\pi\, n_{medium}/\lambda_{vacuum}$. The four complex elements S_1 to S_4 yield the amplitude and phase of the scattered fields if the incident fields are given and thus vary as functions of **r** and contain detailed information on the structure of the particle.

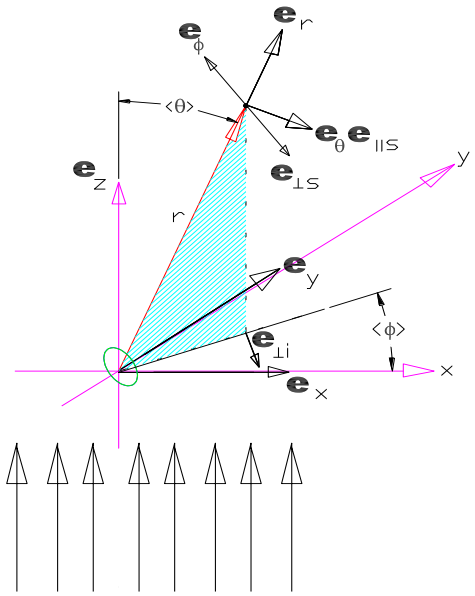

Fig. 2-12 A particle at the origin is illuminated along the z direction resulting in scattered electromagnetic field of **e** components as shown.

We seek to define the incident and scattered light in terms of irradiances which are real quantities, which lead to the definition of the Stokes vector components of I, Q, U, V representing the light intensities related to various combinations of linear and circular polarizations. The Stokes parameters can be expressed in terms the electric field components as [Hecht 1987]

$$
\begin{aligned}
I &= \left\langle E_{//} E_{//}^{*} + E_{\perp} E_{\perp}^{*} \right\rangle \\
Q &= \left\langle E_{//} E_{//}^{*} + E_{\perp} E_{\perp}^{*} \right\rangle \\
U &= \left\langle E_{//} E_{\perp}^{*} + E_{\perp} E_{//}^{*} \right\rangle \\
V &= \left\langle E_{//} E_{\perp}^{*} + E_{\perp} E_{//}^{*} \right\rangle
\end{aligned}
\tag{2.33}
$$

The relationship between the Stokes parameters for incident and scattered light are given by the Mueller scattering matrix which again describes the scatterer's effect

$$
\begin{bmatrix} I_s \\ Q_s \\ U_s \\ V_s \end{bmatrix} = \frac{1}{k^2 r^2} \begin{bmatrix} S_{11} & S_{12} & S_{13} & S_{14} \\ S_{21} & S_{22} & S_{23} & S_{24} \\ S_{31} & S_{32} & S_{33} & S_{34} \\ S_{41} & S_{42} & S_{43} & S_{44} \end{bmatrix} \begin{bmatrix} I_i \\ Q_i \\ U_i \\ V_i \end{bmatrix} \tag{2.34}
$$

Different from the amplitude matrix elements, these sixteen matrix elements are real quantities and also vary with **r** and the wavelength of illumination, containing information on the refractive index distribution throughout the particle.

Fraunhofer diffraction model provides a method to extract structural information from the diffraction images of a planar object. The spatial frequency of various features in an image, computed by their Fourier transform, displays as low frequencies towards center and high at edge. For example Kopp and Pernick [Kopp 1976] produced Fourier transforms of slide sections of human cervical cells.The malignant cells images had chromatin distributions of higher spatial frequencies than normal cells. Other similar studies have been reported [Rozyzck 1982, Seger 1977]. A problem in this Fraunhofer diffraction application is that any small stray object in the object plane will produce the high spatial frequency signal. Also if scattered light passes through a lens, then lens itself distorts pattern received. The placement of a particle in Gaussian distribution beam off-axis will result in a large change in the small angle scattering. [Pernick 1978]

Mie theory provides an exact solution of the vector wave equations of electromagnetic fields for a homogeneous sphere placed in the path of light and in this case Eq. (2.34) reduces to

$$\begin{bmatrix} I_s \\ Q_s \\ U_s \\ V_s \end{bmatrix} = \frac{1}{k^2 r^2} \begin{bmatrix} S_{11} & S_{12} & 0 & 0 \\ S_{21} & S_{22} & 0 & 0 \\ 0 & 0 & S_{33} & S_{34} \\ 0 & 0 & -S_{34} & S_{44} \end{bmatrix} \begin{bmatrix} I_i \\ Q_i \\ U_i \\ V_i \end{bmatrix} \tag{2.35}$$

This study has used Mie calculation software for comparisons on Latex spheres and on spherical biological cells. Brunstig applied the coated sphere model to Chinese hamster cells with good results [Brunstig 1972]. Mie theory can also be applied to non-spherical spheroids of revolution if their aspect ratio is not too large [ref].

2.3.2 Light scattering in flow cytometry studies

Forward and side scatter

Particle discrimination on the basis of forward light scatter can be useful under certain conditions. For angles between 0.5^o and 12.5^o, Steinkamp [1973] showed that the scattered irradiance by polystyrene spheres varies by diameter cubed from 5.8um → 10.5um; varies by diameter squared for over 10.5um; and has a decreasing dependence over 12um. Most notable about these measurements is that, by changing optics from a simple lens of 150mm in focal length to a pair of crossed cylindrical lens, the relations between scattered irradiance and sphere diameter became significantly different. Thus the measurement of scattered light was not independent of the incident beam profile due to different optics used, which is not a desired situation if one is interested to invert the structure of particle from scattered light measurement.

For biological cells, Julius [1975] showed that live and dead murine thymocytes could be differentiated by scattering signals between 1^o and 10^o. The live cells, though of the same

geometric cross section as dead cells, scattered more light. The mechanism for this is that the broken walls of dead cells allow interchange of cytoplasm with the hosting medium, causing a decrease of relative refractive index. Another mechanism for reduction in dead cell refractive index was shown by Braylan [1982] to be associated with cell shrinkage. At the forward direction of 0^o, lost irradiance is the result of absorption and scattering loses, and can be useful in cell discrimination.

Another discrimination tool is in the relation of small angle forward scatter (FS) to the side scatter (SS) along the directions perpendicular to incident light. Salzman showed that subpopulations of leucocytes could be differentiated on the basis of ratios between FS and SS measured simultaneously. Note that the mechanism for this discrimination is not fully understood. Visser [1980] performed FS-SS coincidence measurements on red blood cells, swollen compared to limp. He was able to discriminate between them based upon the smoothness of their surface, the SS being more sensitive to shape than FS. Dubelaar [2006] showed that SS was more sensitive than FS to inside change of refractive index induced by putting air into bacteria vacuoles.

Note that in most of the above cases, discrimination between cells is essentially the issue of gross size or averaged inside gradient of refractive index. Except for the study by Visser, subcellular features are not displaying based upon the angularly integrating detectors located at 0^o, 90^o, and some small forward angles of 2^o to 12^o.

Angle-resolved measurement of light scattering with a flow cytometer

Various methods have been tried to measure angle-resolved scatter from a single cell. Full scatter information of a non-spherical particle requires irradiance measurement at all scattering angles in the polar (θ) and azimuthal (ϕ) directions as shown in Fig. 4-8. Diffraction images of

droplet in air have been acquired and studied by laser levitation [Ashkin 1981]. The optical trapping of the droplet allows its isolation from nearby optical interfaces and acquisition of high-contrast images.

Salzman [1975] arranged a 32-photodiode ring concentrically to detect scattered light at 32 values of θ from 0^o to 30^o. Larger rings for larger angles compensated for rapid irradiance drop-off with increasing θ. A number of high correlation cell discrimination studies which were obtained by integrating over the azimuth angle ϕ. Ludlow [1979] used a similar design with 177 optical fibers each receiving scatter at a different angle and all detected sequentially by a single PMT. Bartholdi [1980] used an ellipsoidal mirror to pass scatter onto 60 photodiodes simultaneously, yielding 60 readings from 4^o to 356^o but only one azimuth angle. Loken [1976] used large-cross-section laser beam to generate scatter for extended travel time, detecting with a single but at increasing angle with particle travel. This arrangement assumes that particle does not tumble or deviate from a straight line during detection period.

Maltsev [Maltsev 2000] developed the flying indicatrix method to measure light scatter at multiple values of the polar angle θ with integrated over the azimuth angles, ϕ (Fig. 2-13A). This was done by streaming particles along the axis of an ellipsoidal mirror coaxial with a laser beam axis. Scattered light intercepted by the mirror is focused through an aperture and thence to a PMT. The geometry is such that the detector output is a plot of integrated scatter as a function of θ as the particle moves along the laser axis. It is necessary for only one particle to be in laser beam at one time. All of the above angle-resolved detection schemes only generate angular scatter measure at fixed or integrated values of azimuth angle ϕ. This of course is due to the use of point detectors around the scattering particle. Mitigating this by stretching time (and space) period of observation puts greater constraints on the particle flow or throughput of processing.

To record all possible angles simultaneously means one choice: use of a very sensitive imaging detector. This approach, however, requires a longer signal acquisition time for exposure reduction or elimination of the optical noise due to the index-mismatched interfaces close to the scatterer.

Several recent experiments have addressed these problems, some of which are illustrated in Fig. 2-13 and Fig. 2-14. A study on angle-resolved scattering of aerosol particles, [Aptowicz 2005], sidestepped the difficulties of flowing cells by imaging airborne spheres and biological cells (spores). Because of the much reduced density and viscosity of gases, a gas stream can be at the focal point of a nearby lens without the intervening space slowing the stream or causing turbulence. Thus there is no need for a flow cell wall and its attendant optical complications. The targets' scattered light passes straight to a collecting lens and an intensified CCD (ICCD) camera. Results showed light interference patterns with some regularity of size and orientation in the diffraction images. Of course this approach cannot have wide applicability for most biological cells which must remain in aqueous solution to be viable. If they are trapped in a spherical droplet in air, then the surrounding air-water interface make its scattered light pattern useless for extraction of structural information about the cell.

Angle-resolved measurement of scattered light by cells in suspension has been done by Neukhammer [2003]. The flow cell used was a 250um square microchannel chamber made of glass and the biological cells were hydro dynamically focused into its center at flowing speed of several meters per second. A laser beam of 1.3W in power and 488nm in wavelength was focused on the flowing cells with microscope objective and a second objective collected the scatters near 90^{o}. With a focused beam of 20μm in diameter excitation beam, the average flux is

$4x10^9$ W/m^2. The scatter signal was passed to an ICCD camera. Images similar to Aptowicz were obtained of blood cells and other particles which are quite noisy and of low contrast.

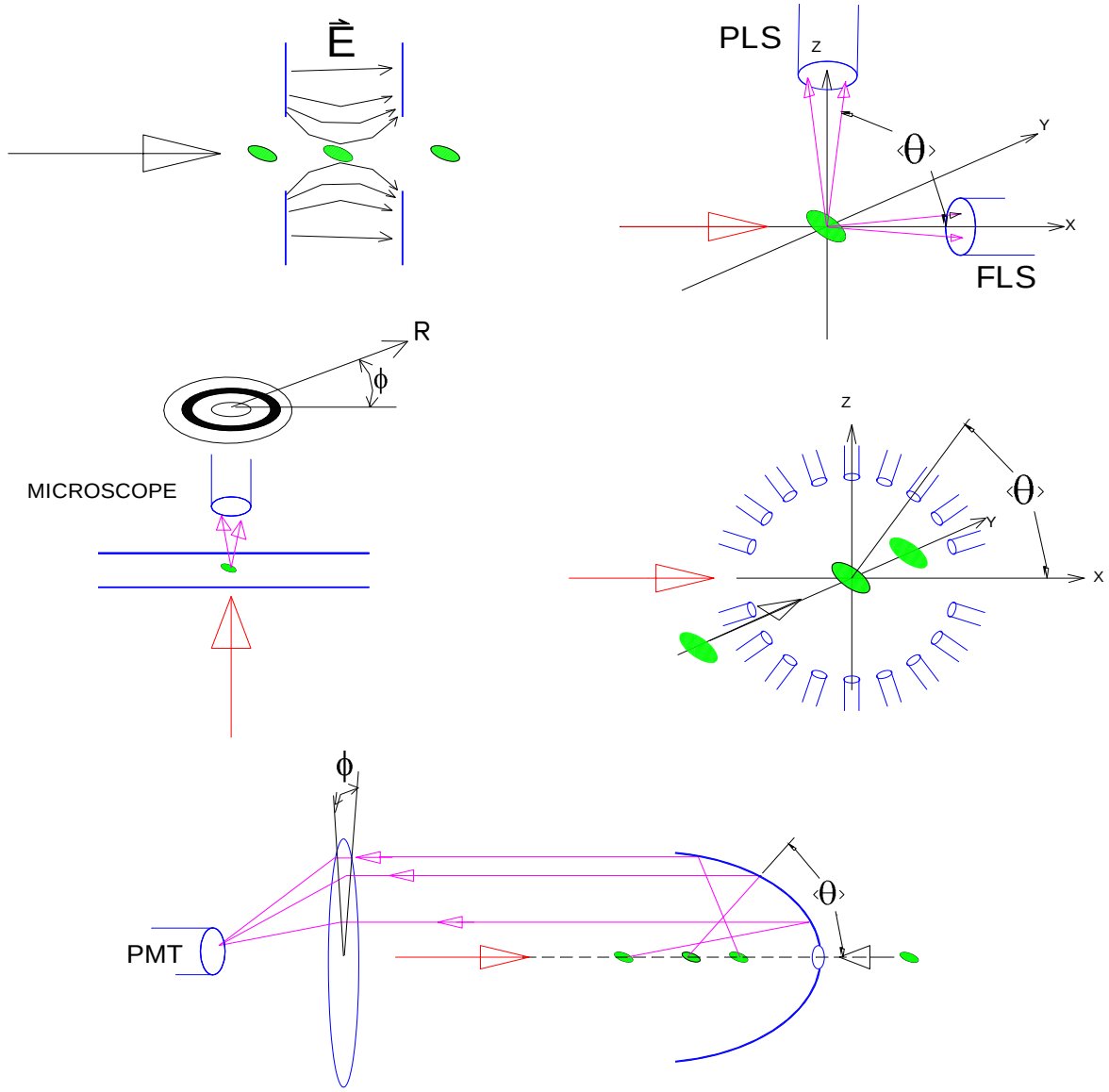

Fig. 2-13 Evolution of scatter imaging designs. Upper left, the original Coulter counter generates a pulse as particle changes field impedance between orifices [Coulter 1953]. Upper right, forward light scatter (FLS) and perpendicular light scatter (PLS), [Visser 1980]. A PMT detector gives pulse size proportional to integrated solid angle. Middle left, a slide contains either dried and flattened cell or a cell falling slowly in viscous fluid [Orvyn 2000], [Seger 1975]. Radial and angular information is collected by microscope camera, not a flowing system. Another variation is to use holographic video microscope and digital processing [Cheong 2009]. Middle right, a 360° array of detectors in plane of laser picks up scatter as a function of θ, but all at only one azimuth angle, ϕ=0°[Salzman 1975, Bartholdi 1980]. Bottom, a flying light-scattering indicatrix configuration in which particle and laser are coaxial. As particle travels along mirror axis, θ progresses from 20° to 160° and PMT generates output accordingly [Maltsev 2000, Loken 1976]. Azimuth scatter, however, is integrated.

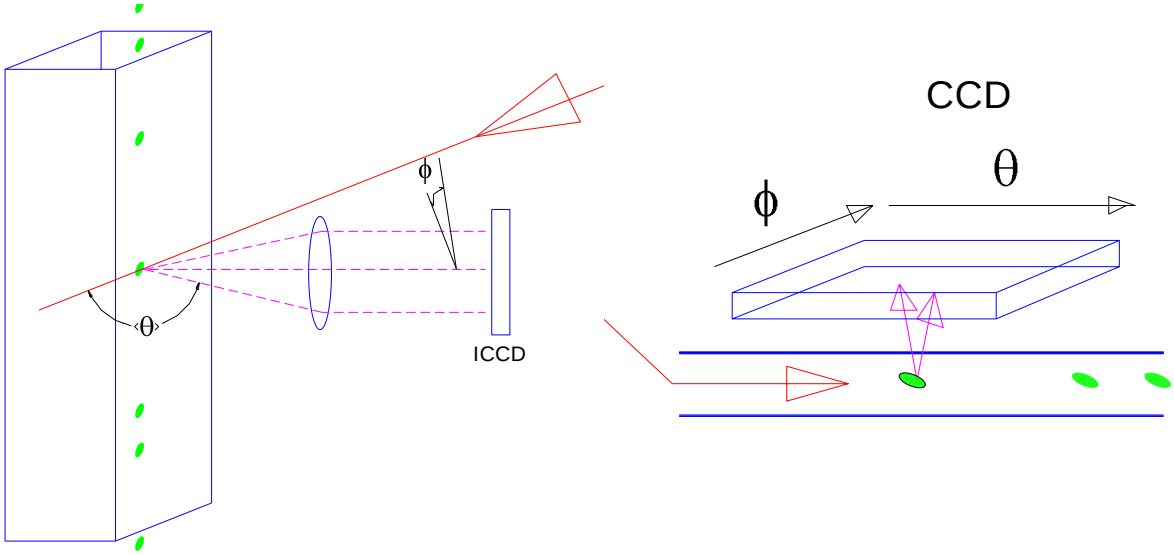

Fig. 2-14 Recent designs giving full angle resolved scatter images. Left: configuration uses quartz flow cell with square, 250um cross section and intensified CCD chip [Neukhammer 2003]. Right: design uses flow cell as a waveguide and CCD chip directly against flow cell wall without lens [Su 2008].

A much less expensive design was tested using a microfluidic design and a simple CCD chip [Su 2008]. The concept is to inject a laser beam coaxially into the flow channel as a waveguide and then place a CCD camera directly against the side of channel through an optical window. No lens is used although a microscope is necessary for alignment purposes. This, however, is only a flowing system when placing the particle into the focusing volume at which time the particle is temporarily immobilized for image acquisition. An instrument developed by [Z Wang 2004] is a miniaturization of a conventional flow cytometer on a microfluidic chip. A very small lens focuses laser beam, from an integral waveguide, onto particle in microchannel. Nevertheless the side scatter signal, received by a microscope objective against the chip, is too weak for imaging detection but a PMT was used for pulse signal detection instead of an image.

Summary of scatter imaging optical configurations

It is useful to bring together the various designs and their limitations to clarify how considerations of different factors compete for a useful instrument design for our study. Fifty years ago the number of detectors started with one PMT for signal detection at a single wavelength and one polarization. With one detector for FS, reflections and refraction of incident light by nearby interfaces is not a big concern since the scattered light signals is integrated over a selected solid angle. The SS signal at 14mm from target is about one ten billionth of incident flux, so when a second detector is added only a small fraction of optical noise from FS will result in saturated SS detectors. Furthermore, much more excitation irradiance is necessary for a reasonable SS signal. A high excitation flux is unacceptable for study of biological cells due to possibility of damage. For imaging detection, any nearby interfaces or particles can lead to significant scattered light noise that is unacceptable for high-contrast image acquisition even though it is tolerable for angle-integrated detection. If the noise-causing interfaces are far from the targeted cell then imaging noise is greatly reduced, but particle trajectories in core flow stream could become unstable. A reduction of particle speed allows longer image exposure time but at some point low particle throughput reduces instrument usefulness. By making diameter of sheath flow large, the stability of core improves but such a large volume of fluid to dispose of could pose a difficulty. For very small flow rates the inside of the core fluid injector tube will be clogged by particles adhering to its wall. A smaller inside diameter for the core fluid tube will reduce adhering to wall by speed increase but the probability of clogging at tube entrance increases.

An example of these design challenge has been discussed in the instrument design of the Neukhammer's report [2003]. It required an incident laser beam power several hundred times

greater than the systems reported by Su et al. [2008] or by our instrument [Jacobs, 2009a, Jacobs, 2009b]. In addition, an intensified CCD camera has to be used for the very weak side scatter signals for imaging and the diffraction images appear to be of reduced contrast perhaps because of the presence of chamber walls 125um away from the particles and of low resolution because of the ICCD's microchannel plate. The imaging study reported by Su et al. [2008] used not only a much lower power laser but an inexpensive CCD camera. Nevertheless these images are of considerable low contrast because of, presumably, the imaging noise from the spurious scattering of the incident laser beam by wave guide.

§2.4 Review of diffraction imaging of biological cells

In the late 1970's (at the Battelle-Frankfurt Research Center) large numbers of diffraction images of biological cells were recorded and submitted to data analysis software with the idea of connecting cell morphology and biology with its associated diffraction image [Seger 1977]. These images were acquired from a dried cell plated on a slide with the forward scattered light imaged through a microscope. A later improvement was to embed the cell in immersion oil so that the relative refractive index between nucleus and cytoplasm was comparable in magnitude to that between the host medium of oil and the cytoplasm. Signals were digitized in a polar plot with the radial variable R expressing the polar scattering angle θ and angular variable φ the azimuth scattering angle ϕ. Combined with the work of Genter [1978] they were able to correlate certain cell characteristics with the dominant frequencies in the polar plot of the scattered light irradiance. Cell size can be determined from the image components of high frequencies, nuclear diameter from those of lower frequencies, and granularity (nuclear substructures) from those of lowest spatial frequencies. Their conclusion was that these wave

frequencies expressed themselves over all scattering angles. However, these polar plots show that radial irradiance for granular and coarse cells suggest that a cell with fine granularity has its peak intensities shifted to high range of scattering angle θ. But the standard deviation of this shift looks to be so large that categorizing a cell on this basis would not be accurate .

In 1985, Steen et al. were able to conduct a more specific imaging study on cell components. He used histograms of peak angular irradiance of blood cells over a range of θ from zero up to 125^{o} to correlate the angle with cell characteristics. Cell diameters of 10 to 30um, and nuclear diameters of 3 to 10um, expressed most scatter in angles $<10^{o}$. The presence of mitochondria (long dimension 1-4um and small diameter 0.2-0.5um) dominated scatter in the range $>13^{o}$. Presumably lysosomes (0.2-0.5um), Golgi apparatus, endoplasmic reticulum and cytoskeleton will be most visible at larger scatter angles.

In another study [Mourant 1998] the researchers used a goniometer to examine cell suspensions. The model used was of a cell as a distribution of various sized spheres, to be analyzed with the Mie theory. They used goniometric results to determine the angular dependence of scattered light, $P(\theta)$, and the reduced scattering coefficient and compare them with modeling results . The conclusions were that most scatter is from inside the cell and progressively smaller structures (as spheres) would yield scattered light over progressively larger scattering angles. A similar study by Drezek et al. [1999] also was done with cell suspensions and a goniometer. Careful study of angle-resolved scattered light irradiance for cells of different parameters (e.g. nuclear diameter, refractive index of organelles, collagen orientation) was done both experimentally and using the Finite-Difference-Time-Domain (FDTD) model. They showed that these cell parameter variations result in corresponding variations in scattering pattern but, most notably, the variation is small. Thus any instrument that would diagnose cells will need to

be both sensitive to the structural variations and yet allow for cell variability in a suspension sample.

The angle-resolved scattering measurement with an imaging camera for single cells in flow by Neukhammer et al. [2003] was able to allow the determination of sizes of spherical cells and also to see a difference between native and sphered red blood cells. Apparently the very high speed of flow through, low resolution of ICCD camera, and perhaps imaging noise from interfaces around a flowing particle resulted in such low contrast images that no other conclusions about biological cells could be made.

Although the study by Aptowicz et al. [2005] is only applicable to aerosols, it is useful for correlating the variability of patterns in the acquired images to the structure of the imaged particle. Essentially the number of bright “islands” by strong light scatter and their eccentricity and relative alignment along their long axis correlate strongly to the gross size of the particle but weakly for internal structures.

Wilson et al. [2005] reported that using scatter analysis of mitochondria suspensions the change in size or surface material of these organelles induced by photodynamic therapy treatment (PDT), could be detected. Applying the coated sphere model to mitochondria before and after treatment revealed an increase of the scattered light toward larger polar scattering angles. Again, the shift is small and would be very difficult to detect in single cells. Su et al. [2009] applied a FDTD model to simulate light scattering variation due to the mitochondria. In this case it is the aggregation of mitochondria either to the nuclear membrane (healthy) or randomly throughout the cell (cancerous) that generates a change in angle-resolved scattered light distributions. This change correlates with a reduction in scattered light irradiance at smallest

scattering angles for cancerous cells. Since this is a simulation, it remains to be seen whether the abundance of noise in an experimental study would conceal this signal.

An instrument has been developed to measure the spectral polar angular (both polar and azimuthal), and polarization dependence of the backscattered light from living tissue [Kim 2003]. Using this instrument Yu et al. [2006] measured the azimuthal light scattering spectra of epithelial cells. They report an asymmetry of the scatter between 0^o and 180^o in azimuth angle. This asymmetry does not appear in non- cancerous epithelial cells, suggesting that, by measuring the scattered light distribution in a full angular range of 360^o in both polar and azimuthal angles more cellular morphology information could be revealed.

Chapter 3 Development of flow units and chambers

The development of a diffraction imaging flow cytometer was initiated by building a fluid handling unit to investigate different flow chamber designs. Two requirements related to imaging flowing particles necessitate a series of changes away from conventional flow cytometer designs. One is that image acquisition requires a longer time than what is needed using light integrating detectors, so the particles to be interrogated must move much slower. The other requirement is that one must eliminate or significantly reduce corruption of the scattered light signal caused by index-mismatched interfaces close to the imaged particle. This chapter presents the evolution of system designs for meeting these requirements.

§3.1 Fluid pump unit

General design considerations

To achieve the goal of low flow speed, tubes and channels of small diameters must be used for fluid transport, and consequently the ultra low rate of particle suspensions flow generate serious, and frustrating, operating problems. Core flow rate must be in the range of ~10^{-4} μL/s in order to achieve a flow speed of 1-10 mm/s with a core diameter of 10 to 20μm. Flow at this rate means that a leak in the plumbing that drains away core fluid can take an hour to appear as a barely visible drop, yet that drop indicates complete failure of the hydrodynamic focusing system. Keeping all external plumbing surfaces clean and dry is critically important in construction of the fluid system, allowing easy spotting of even very small drops, and hence leaks.

Gas bubbles create flow blockages or oscillations and also produce optical noise if they intercept an optic path. Surface tension forces and adhesion of a bubble to wall are remarkably

difficult to overcome by pulsing of the fluid stream, often forcing total disassembly of plumbing. To reduce formation of gas bubbles, a well-designed flow handling unit needs to have strategically located gas escapes. Also necessary are valves and injectors to allow fluid changeover in the system without draining the tubes, so that once assembled and filled with water no air enters again. One can also reduce bubble formation by using degassed water and/or using alcohol to change bubble surface tension [Crosland-Taylor 1953].

Contaminating particles in the fluids are very harmful to precise control of fluid flow since they will not only snag in a small diameter orifice such as a focusing nozzle but also adhere to inner walls of tubes and cause blockage by progressive accumulation. Even without these contaminating particles a suspension of very high particle density can lead to clumped particles being imaged instead of single particles as is assumed. Their scattered light signal can preempt the triggering pulse height discriminator, which is set for single particle scatter pulses. At the other extreme some impurities are colloidal in size range, such as bacteria or growth medium components. These generate a background aura which reduces image contrast. Pure fluid sources and in-line filters can eliminate some of these problems although unavoidable broken cells and released cytoplasm will generate optical noise. Clumping of the sample particles depends upon surface chemistry and agitation of the sample in reservoir. Stirring issues are addressed further below.

Clogging of tubes or orifices in the fluid handling unit is a common problem. Protocols for producing clean suspensions of non-clumping cells are available but the probability of failure cannot be reduced to zero. Filters are commonly used but are not perfect, since they must permit sample particles' passage. The system should be designed and constructed for easy disassembly and cleaning, which is nevertheless always time consuming. Microfluidic flow cells that are

disposable represent an alternate solution, although their functionality is presently limited. A possible quick solution is vibration or generation of a reverse or forward pulse of fluid, core or sheath fluid, to break a clog loose. A disadvantage is that data acquisition can be disrupted and/or that weak plumbing can sprout leaks under the high pressure.

Even if the core stream is narrow enough to contain only one particle at a time, the stream itself can drift about relative to the interrogating light beam and/or microscope focal plane. When this occurs the diffraction image pattern changes dramatically, unlike the case of non coherent imaging in which the image merely blurs and changes size. Thus an optical design that allows independent adjustment of the focus of interrogating beam and of the microscopic imaging unit is essential for image acquisition. For these experiments, sheath and core fluids need to be of very low flow rates, of known and controllable values, and free of pulsations. In addition the core fluid, containing suspended particles, must not lose its contents to wall adhesion or orifice clogging on its way to the optical interrogation point.

Early pump units

Several pumping systems have been designed, built and tested. The first one, shown in Fig. 3-1, is based on a Becton-Dickson FACS system developed in the early 1980s. It employs pressurized nitrogen gas with a 15 psi sheath regulator and a high sensitivity differential regulator to float core pressure to within a fraction of 1 psi (7 kPa) below the sheath pressure. After initial tests it became apparent that the flow speeds were too high for our imaging acquisition.

Therefore a hybrid system was developed. It uses a pressurized reservoir for sheath fluid and a single syringe pump for the core fluid, as illustrated schematically in Fig. 3-2. A geared variable speed DC motor with belt final drive to a lead screw gives smooth reproducible volume

control of sample. An in-line syringe stirrer was designed and built and positioned at the output (top) of sample syringe (see Fig. 3-3). While this design was effective, it was not capable of measuring and controlling the ratio between the sheath and core fluids.

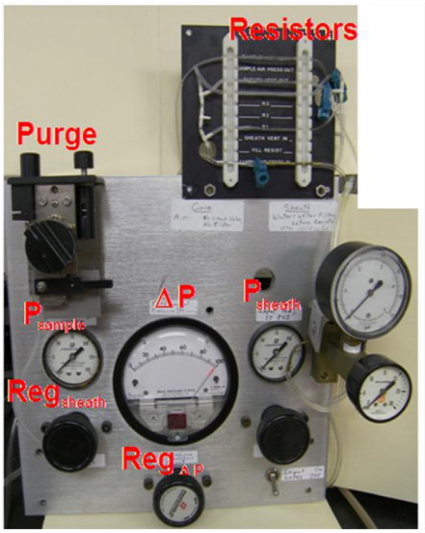

Fig. 3-1 The pressure control unit with P_{sheath} held constant by a regulator Reg_{sheath} . A smaller pressure P_{sample} is applied to the core with sheath-core difference (ΔP) controlled with a precision regulator $Reg_{\Delta P}$. Flow is stabilized by 200μm I.D. fluid resistors. Obstructions in focusing nozzle are dislodged by water pulses (Purge).

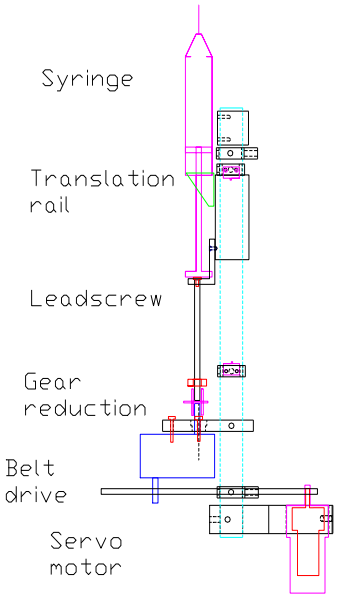

Fig. 3-2 Syringe pump with servo motor driving a lead screw. Drive is through a rubber belt and flywheel for smooth motion.

Fig. 3-3 Mechanical stirrer inside the driven syringe (at bottom) filled with sphere suspension. Small impeller at top of syringe is motorized through O-rings. Sphere suspension flows out through left side channel.

Three channel syringe pump

A three-channel syringe pump unit was built, as seen in Figs. 3-4, 3-5. Variable speed DC gear motors drive multi-ratio spur gear transmissions which in turn push syringes, using lead screws and translation shafts equipped with linear ball bearings. Minimum syringe travel speed is 10^{-6} mm/s, which yields flow rates, depending upon syringe diameter, from 70μL/s down to

$4x10^{-5}$ μL/s, a dynamic range of over 10^6. With this system, the lowest flow speed for a core stream of 5um diameter results in a 0.1 mm/s flow speed if a 0.5mL syringe is used. If a high gear ratio and large syringe are used it allows high sheath flow rate that is necessary for the submerged jet flow chamber, to be described in next chapter. The third channel can be used for possibly pumping a second sheath such as for coaxial jetting into a chamber, or for cascaded hydrodynamic focusing [Kummrow 2009].

Fig. 3-5 shows the complete syringe pump unit with the electronics at top. Optical encoders allow motor speed readout which, with transmission ratio, establishes flow rates. The entire drive assembly is mounted in a large motor driven yoke, creating a rocking motion intended to prevent particle settling in the sample syringe. However it was found that this rocking motion was not sufficiently vigorous to prevent settling.

Because the rocking motion was ineffective a second approach to keep particles from sedimentation or clustering was to build a magnetic stirrer drive coaxial with the sample syringe with a magnetic impeller inside syringe. This is a complicated device and difficult to clean. And in any case the long tube from the syringe pump to the flow chamber would still occasionally trap particles. This is because a core velocity of 1 to 10 mm/sec corresponds to a fluid velocity in the supply tube (diameter~500μm) approaching to the gravitational settling velocity of 25 micron spheres. The terminal velocity of a sphere settling in a fluid can be estimated as [Batchelor 1967]

$$u_{terminal} = \frac{\Delta\rho \;\; g \;\;\; 4/3 \;\; r_{sphere}^2}{6\eta} \tag{3.36}$$

So a 25um latex sphere drifts downward at 19um/s, a 10μm sphere at 3μm/s, biological cells should be around half of that speed (ρ_{latex} = 1.05, $\rho_{biol.}$ = 1.025). Note that most flow cytometers

employ core fluid flow speeds ranging about 1000 times greater than the above values, so settling inside the feed tubing is a much less severe issue than ours.

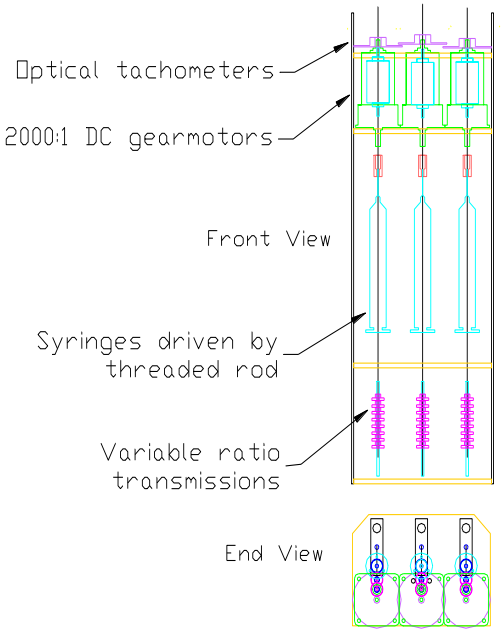

Fig. 3-4 Above is schematic of the three-channel syringe pump. Optical tachometers on high speed end of gear motors provide measure of Q. "Gas-tight" glass chromatography syringes are mounted on linear bearings and driven by lead screws.

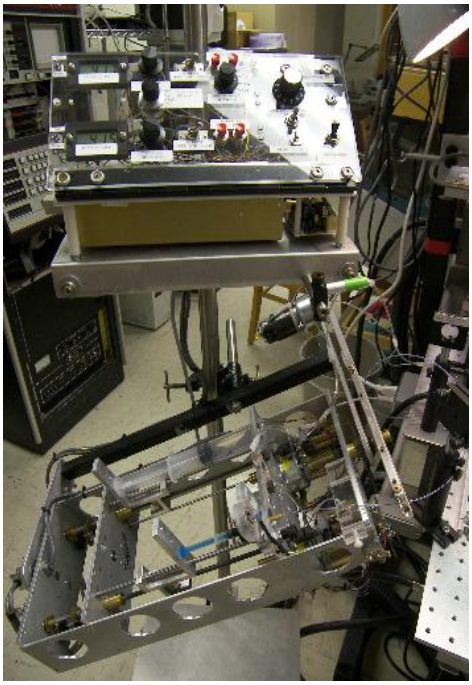

Fig. 3-5 The three-channel syringe pump. Entire drive assembly (at bottom) undergoes rocking motion to keep suspensions from settling and is tilted up when removing bubbles.

§3.2 Flow Chamber Designs

The conventional design of flow chamber in a BD FACS system

The first effort of our cytometer study was performed with a commercial Becton-Dickinson (BD) jet in air nozzle connected to a fluid control unit supplying a 15psi sheath fluid and 0.5psi differential regulator for the core fluid. The BD nozzle uses a precision machined core injection tube of 500um I.D. and a press-on 100um jeweled orifice at the end of a ¼ inch long accelerating

cone tube, as displayed in Fig. 3-6. Note that the nozzle is tapered steeply, reducing the diameter of orifice from 5000μm to 50μm over a distance of 5mm. Acceleration of cells at injector tip can be several thousand g's [Van Dilla, 1985].

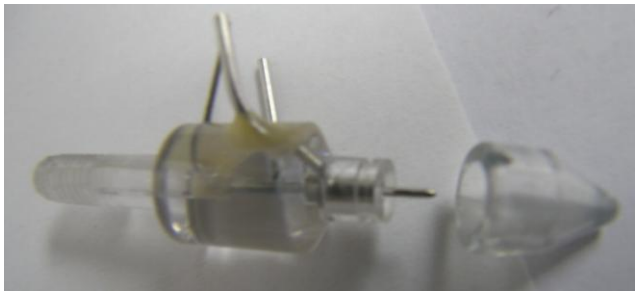

Fig. 3-6 A BD flow cytometer injector and nozzle with 80μm I.D. sapphire orifice in the apex of the nozzle. Core fluid enters the furthest left tube and has a carefully machined tip on other end. Other two tubes are for sheath fluid and de-bubbling.

Acquiring a finely focused core fluid with dye in air is straightforward, but a minimum velocity, ū, is required for a laminar jet to form in air. This is because the rate of energy into the nozzle orifice, of radius a, must be greater than the rate of surface energy necessary to form the new jet surface, (Melamed, 1990). A fluid of density ρ and relative surface tension σ will therefore require a minimum velocity of

$$\bar{u} \geq 2\left(\frac{2\sigma}{2a\ \rho}\right)^{1/2} \tag{3.37}$$

For a 100μm diameter orifice this corresponds to a velocity of 2.3 m/s., typical for many commercial instruments but 10^3 times faster than our requirement of ~2mm/s for imaging. The laser used was a 0.5mW HeNe laser. In addition to being too fast the cylindrical jet also acts as a thick lens in air. This lens effect distorts the incident laser beam from a Gaussian profile and also creates a distorted scattered light distribution, a problem for an imaging detector. In an effort to eliminate scattering of an excitation beam by the jet-in-air design, a differently shaped nozzle orifice has been reported which uses a square or triangular cross section (Eisert 1981). This creates a jet stream with optically flat-surfaces in air. Aside from the fabrication difficulty, it could not be used here because of the requirement for higher jet velocities.

Coax flow cell with circular cross section in Plexiglas and PDMS

Therefore the FACS design of the flow chamber was abandoned in favor of a chamber which progressed through several design improvements to reduce particle speed and eliminate optical scattering noise. As shown in Fig. 3-7 a casting block was made of two mating sides that were clamped together, filled with elastomer, and then opened after 36 hours. Inside surfaces of casting block are glass lined to create an optical surface in PDMS casting. An 8 mm glass rod was softened, tapered down to 0.15mm and suspended within the casting block. Removing the rod from cured PDMS without breaking requires a special technique. As seen at bottom of Fig. 3-7 the assembled flow chamber is the clear rectangular bar (with channel inside) extending from brass injector assembly at center to brass clamp at left.

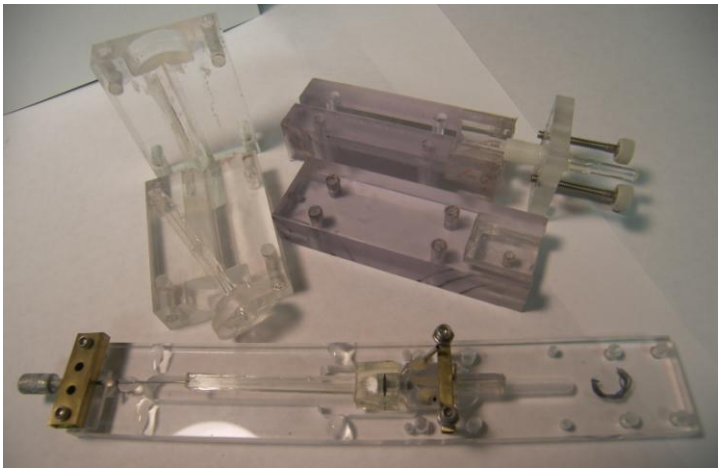

Fig. 3-7 Components of a casting system (top) built for fabrication of micro fluidic channels in PDMS flow cell (bottom).

The first microchannel flow chamber was fabricated by casting Plexiglas around a drawn glass rod. The rod was drawn down to 200um diameter and coated with release compound. This proved unsatisfactory because the release compound generated optical distortions in the channel wall cast against its surface. Polydimethylsiloxane polymer (PDMS) was then chosen and cast around 100um diameter stainless steel wire to form a microchannel. This channel was spliced via a hypodermic tube into a tapered channel made from drawn glass, and sheath and core were then injected into large end of resulting tapered cavity. It was found that drawn wire has striations

caused by the die used in its fabrication. These in turn generate unacceptable marks and distortions in the micro channel's optical surface.

To cast PDMS it is necessary to remove bubbles entrained by the mixing process in order to capitalize on its optical properties. Vacuum degassing of the mixed polymer was unsatisfactory because toluene, an ingredient in hardener, would evaporate along with air, generating lingering bubble foam. The most efficient way was to use a shallow casting form, ~1-2cm, and then bubbles will drift to surface in less than the 24 hour setting period, leaving a clear, undistorted optical medium. One disadvantage is that any fingerprint, dirt, soap etc. permanently mars the surface of PDMS.

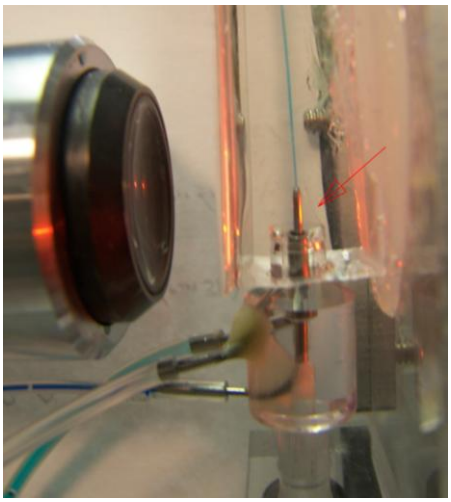

Fig. 3-8 A flow chamber with a laminar flow inside its microchannel. Core fluid is blue dyed within the sheath of water-glycerol solution and whose index is matched to the channel. Just around top of injector the cone shaped channel inner walls (arrow) are barely visible.

The next flow cell was made by a single casting around a drawn round glass rod which in turn was suspended in 1cmx1cmx10cm glass casting container. PDMS has very good release properties and forms an optically flat surface against glass. With special techniques, glass of diameters as small as 100um can be removed from a cast PDMS block. The BD injector was pressed into the PDMS base in the place where the large end of the glass casting rod had left a cavity, designed to be undersized relative to the injector diameter. A tight fit was thereby formed around the injector. As a result of the compliance of the PDMS block, smooth, if unpredictable, curves for the sheath and core acceleration zone were formed and are faintly visible in Fig. 3-8.

Water-glycerol solution as index matching medium

The sample fluid chosen was water with 25μm spheres suspended. Sheath fluid was a water glycerol mixture adjusted to match the refractive index between PDMS and water sample. A 56% by weight glycerol solution has a nominal refractive index n_D of 1.406, viscosity η of 6 mPa-s, and density ρ of 1.15 g/cm^3. PDMS refractive index is listed as n=1.406. A number of experiments were performed to use the index-matching technique as a means to eliminate scatter, reflections, and distortions from the sheath-channel interface close to the excitation beam. Fig. 3-9 shows the light scattering occurred at the fluid-to-channel-wall interface.

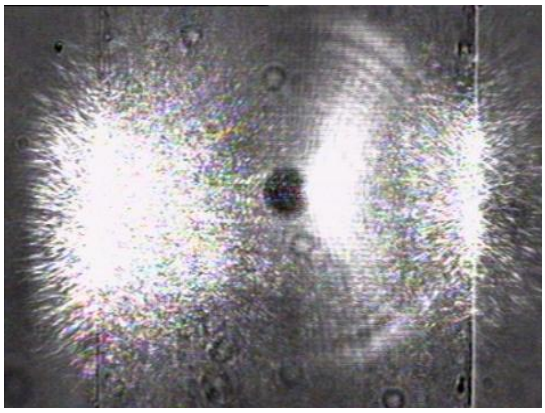

Fig. 3-9 Scattering at PDMS interface by laser from left. Flow chamber contains index matching fluid with wall. Sphere diffraction is also visible. Diameter of the channel: 200um. Its walls are visible as vertical lines on right and left sides and scattering is at these interfaces. Laser beam is from right.

It was found however that index-matching could not be perfectly realized. The residue index mismatch for the interface of very large curvature coupled with high irradiance of a focused laser incident beam can still cause considerable scattering noises in the acquired images. Fig. 3-10 shows clearly that the PDMS channel-sheath interface continues to cause scattered light even though the matching fluid was progressively stepped through the refractive index range of the polymer walls. A step change of 0.1% in glycerol content, in the concentration vicinity of 56% glycerol-water mixed solution, corresponds to a 10^{-4} change of n_D and did not eliminate the scattered light noise. Another possible cause of scattering noise could be due to particles adhering to the inner surface of the PDMS microchannel. Note that the side scattered

light signal around 90^{o} to the incident laser beam is very weak and any residue index mismatch can lead to considerable scattering noise in the images measured by a CCD camera.

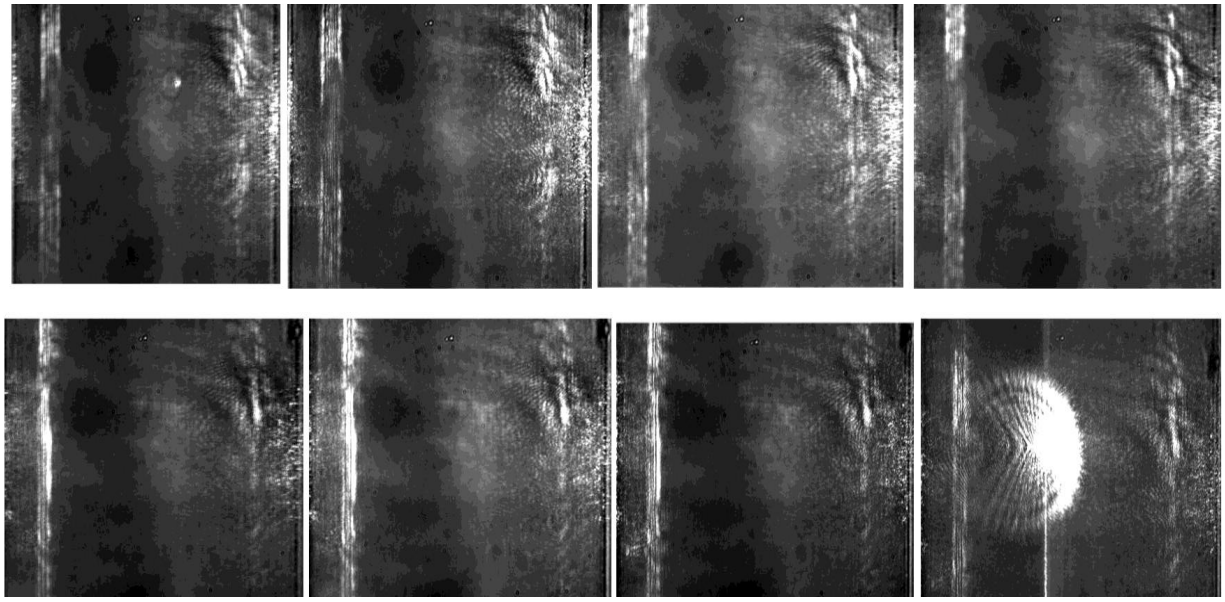

Fig. 3-10 Images of a 200μm diameter round PDMS channel filled with water-glycerol solutions of varying concentrations. Channel walls are seen as dark lines at very far left and right edges. Vertical bright lines are 45^{o} reflections from curved surface of channel. Concentrations (by weight) in images from upper left to right are 51%, 54%, 57%, 60%; from lower left to right 63%, 67%, 72 %, 72% w/ 25μm sphere. Laser beam is incident from right. Scattering is not be eliminated at any concentration.

It has been reported that optical sensing in microfluidic chips made with PDMS material can be improved by altering the hydrophobic surface property of PDMS for biological interactions, particularly adhesion, inhibit free flow [Hillborg 2000].

Sheath fluid density considerations in microchanneled chambers

The initial testing of this flow chamber design was in a horizontal position. At the low flow rates necessary for imaging, the lower fluid density would cause the core fluid to divert from the expected central position, floating toward the channel sides. If the flow chamber was repositioned on a vertical axis then the core fluid buoyancy would enhance flow characteristics, meaning a smooth, laminar flow focusing down to a small core diameter. Furthermore the

relative immiscibility between a water core fluid and a water-glycerol sheath fluid means possibly less momentum exchange at their interface. Most experiments to validate submerged jet flow modeling have used immiscible fluids because of the simplification brought by a sharp non-mixing interface between phases [Vempatti 2007]. Nevertheless, since scattering noise could not be eliminated with index-matching sheath fluid, this direction of experimentation was discontinued.

Coax flow chamber with square cross section in PDMS

To solve the problem of scattering noise generated at the cylindrical microchannel walls a square cross section flow chamber was fabricated reduce curvature. Typical flow chambers with square walls are fabricated with quartz glass of high costs. For this study a flow chamber was made similar to the previous cylindrical type but cast with a square cross section glass rod drawn to a 120um strand. At first hollow glass square tubing was tried. Square borosilicate tubing of 8mm side length (Friedrich and Dimmock Glass Inc.) was drawn to small dimensions. It was discovered that the walls became concave at small dimensions. Although square micro dimensions are available commercially, splicing a square micro glass rod onto a tapered region to accelerate the core and sheath fluids results in severe surface irregularity which in turn compromise laminar flow condition at the splice.

After multiple tests, we found that drawing solid square glass rods yielded rods of true square cross sections at small dimensions. The tapered rod was cast inside a $1cm^2$x10cm flat glass container lined with cut microscope slides and filled with PDMS. After curing and carefully withdrawing the tapered rod, a flow cell with optically flat surfaces both inside and outside was the result. A core-sheath injector similar to the BD FACS machines was pressed into

the base of the PDMS casting. Water-glycerol sheath fluid was pumped in coaxially around a water core fluid containing the particles for flow testing.

Optical artifacts of square channels and test for solution

The result of the square cross section micro channel was the immediate elimination of scattering noise interfaces of large curvature. However a remaining problem, as seen in Fig. 3-11, is optical artifacts. A 25um polystyrene sphere excited by a laser beam is expected to have a diffraction image similar to Fig. 4-8. The image pattern of Fig. 3-11 is far from the expected. Even though accurate modeling in this case is difficult to achieve, we can attribute this type of pattern to the presence of the of the microchannel interfaces. Increasing the channel cross section dimension up to 500um did not eliminate these artifacts and it remained in the field of view under different conditions of excitation and observation.

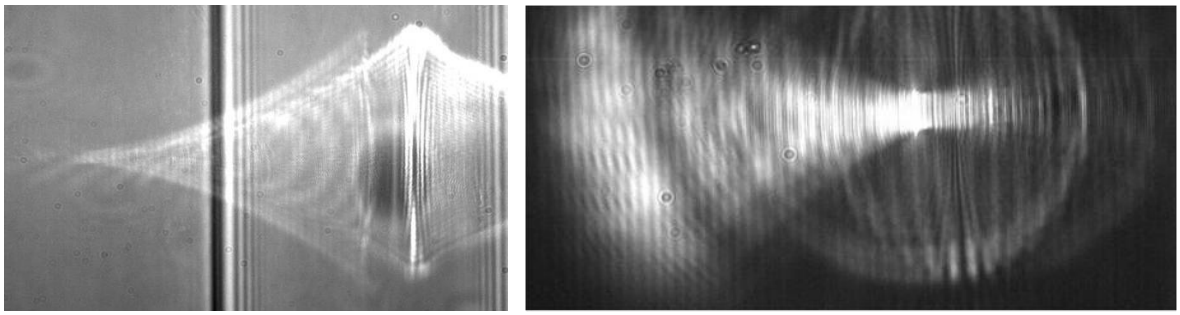

Fig.3-11 (a) Optical artifact image result using a 0.55NA objective, with laser illumination from the right side and non coherent light from behind. A 25μm latex sphere is in water coaxial within a water-glycerol index matching solution. The latter makes contact with 120um square channel of PDMS. (b) Artifact generated by sphere too close to exit nozzle. Minimum distance for noise free image appears to be about 300um for the optics used here.

A similar experiment has been performed that did not manifest this problem. Neukammer reports using a flow cell of 250um square channel of quartz or glass [2003]. A laser illuminates through one side and a microscope objective of small numerical aperture (NA) receives scatter through a perpendicular side as shown in Fig. 2-14. Although the images are of low resolution,

no artifacts are present in their image results. Rather than pursue this design further we decided to investigate another. This is the submerged jet-in-chamber in which the index mismatch at the sheath-channel interface is eliminated by using large chamber dimensions. To do this the coaxial laminar flow was injected into a flow chamber with flat optical sides and overall dimensions 1cmx1cmx6cm. Its base was sealed to the square microchannel described above. An 80um glass capillary was forced into the square microchannel end, with a smooth flow transition between capillary and the microchannel enabled by the PDMS compliance. The capillary was used to inject the core fluid into the flow chamber. Upon testing the artifacts were eliminated and background optical noise was also eliminated.

Although the submerged coaxial jet exhibited some turbulence at the flow transition zone, the main issue, apparent in Fig. 3-12, is the jets' rapid expansion upon entering chamber. This caused the ~30um diameter core to become 100um, an unacceptable diameter because particles are no longer solely confined within focal volume of imaging objective. From Eq. (2.29) and the plot in Fig. 2-7 it can be seen that the submerged jet diameter is roughly inversely proportional to the jet speed. The submerged jet design was used by [Mullaney 1969] and is shown in Fig. 2-9C. Note, however, that for higher speeds expansion of the jet is slight and creates little problem. But for the slow velocities required with imaging it becomes significant,

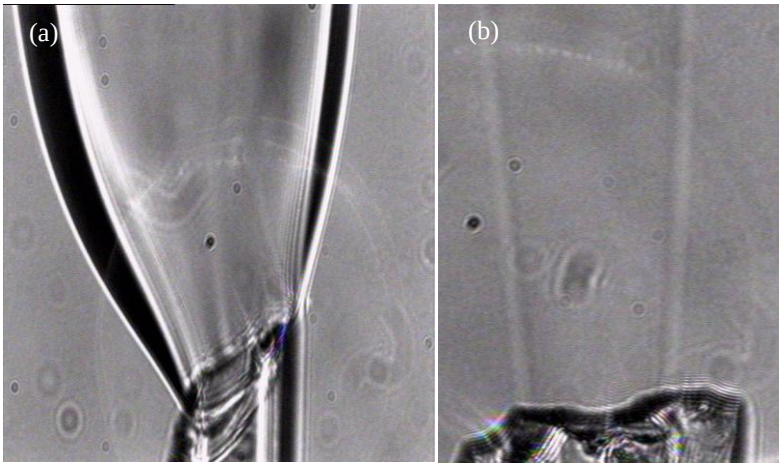

Fig. 3-12 (a) A laminar flows of sheath and core fluids jetted at 8mm/s into a static water chamber. Injector is 80μm I.D. glass hypodermic extension of the PDMS flow cell. (b) Same flow with a speed of 40mm/s.

resulting in a spreading of the particle distribution at its interrogation point. The three phase flow cell presented in next chapter deals with expanding jet problem by surrounding it with a second coaxial stream, a “momentum shield”, and also a nearby exit tube to further contract the jet.

Stirrer integral with flow chamber

To deal with this problem the particles inside syringe pump were moved to a separate reservoir. The syringe pump was used only as a hydrostatic drive for a stirred sample reservoir integral with the focusing chamber. Thus the syringe pump piston drives a second slave piston located inside a magnetically stirred sample reservoir, as seen in Fig. 3-13(a). Magnetic stirrer is at the bottom of the Y shaped glass reservoir shown in the diagram; slave piston is inside the left arm of the reservoir. As the slave piston is driven into reservoir, stirred sample or core fluid is displaced upward through a short hypodermic needle into flow chamber. The slave driven flow actually was smooth and consistent, without intermittent sticking by O-ring seals and without backlash. A small coiled tube inside slave reservoir served to purge sample reservoir of air.

By this configuration the stirred sample only travels a few centimeters vertically inside a straight, unobstructed, tube which is of small enough diameter to create a high flow speed even though the diameter of core stream is small. This hypodermic needle also serves as the injector tube for hydrodynamic focusing nozzle, seen in green in diagram 3-13(b). It was further hoped that the rotational currents created by the rotating magnetic stirrer would extend into the hypodermic needle since the vortex and needle are coaxial. However turbulence caused by stirring is also transferred through the needle and results in disturbances to laminar flow in the focusing region of flow cell. This limits stirrer operation to either very slow or intermittent use. In addition it still allows downward settling rate of large particles to compete with upward driven rate of core flow.

So the final improvement to stirring techniques is to place the reservoir directly above the flow chamber [Ludlow 1979]. In this design we are adopting a fluidic design trend here to eliminate the separations between various components of the flow unit and to use gravity to enhance and not encumber. For very slow core speeds this design enables the sample particles to be driven by both the sample syringe and by gravitational sedimentation as shown in Fig. 3-14.

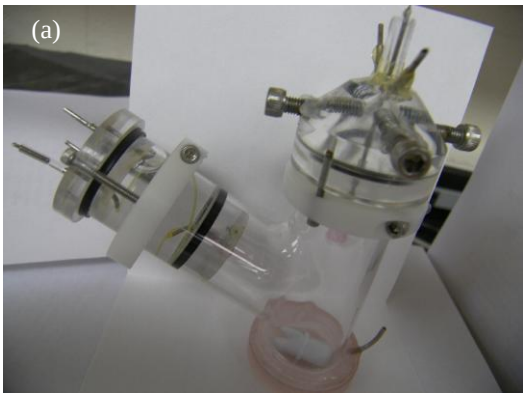

Fig. 3-13 (a) A photo of the integrated sample reservoir, stirrer and flow chamber. Slave piston is at left near bottom of side arm of Y shaped vessel. (b) The schematic of the assembly with flow chamber at top (green). Injector needle steering screws are around top of reservoir just below supply and injector tubes. Sheath and core are fed in through two small tubes flanking injector needle. Magnetic stirrer is at bottom with provision for draining reservoir.

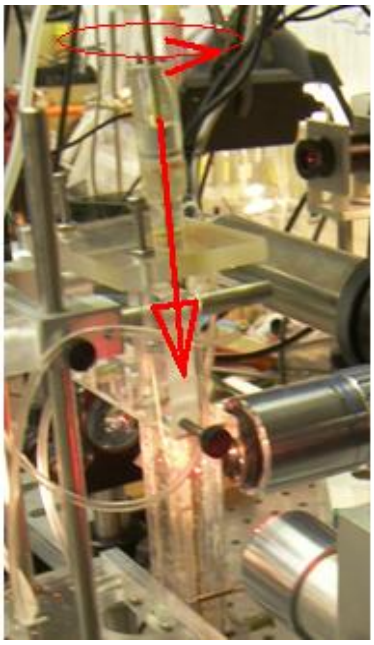

Fig. 3-14 A photo of stirring mechanism integrated with flow chamber on bottom. Stirred particles only pass directly down a 3cm core needle to chamber.

§3.3 Fluid dynamics and pressure measurement

Fluid resistor to stabilize flow

The pressure differential between core and sheath fluids at the interface where they first meet in the nozzle is small and diminishes even further for the lower flow rates needed for imaging. In fact the differential pressure regulator poses a design problem in gas pressure driven systems,

requiring precision regulators and flow restrictors. But with syringe driven flow, slight irregularity in its mechanical drive dramatically interrupts nozzle dynamics.

One solution is to place a flow resistor in series with the driven fluid such that the pressure drop of resistor is much greater than pressure gradients in nozzle. In conjunction with a small bubble placed inside the syringe the fluid flow is stabilized considerably since the resistor dampens pressure pulses and absorbs the energy stored in the bubble [Shapiro, 1985]. A stabilizing fluid resistor was made from 10 meters of 50um inside diameter (I.D.) nylon micro bore tubing. With a water pressure of 2.5 inches water (623 Pa) the resistor has the same flow rate as the typical nozzle at a pressure of 0.2 inches of water. Thus the resistor is 10 times nozzle resistance, reducing by a factor of 10 the susceptibility of flow variation to pressure variation inside nozzle.

Smoothness and oscillations

Smoothness of flow is critical for achieving a low velocity, small diameter core [Melamed 1990]. There are several sources of disrupted flow in hydrodynamic focusing: high flow ratio, wall generated turbulence, surface tension differential between phases, mechanical drive pulsing, and particle adhesion.

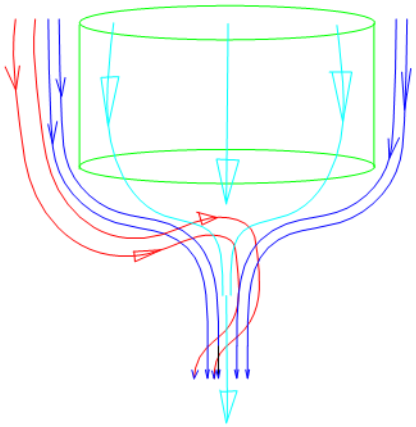

Fig. 3-15 A schematic of streamlines around the end of core injector (green). When the velocity ratio between sheath (blue) and core (turquoise) is too large, a vortex (red) will creep up injector tube, disrupting flow.

As can be seen in Figs. 3-15 and 3-16, there is a limit to the amount of focusing that can take place at the interface between sheath and core in the accelerating zone [Van Dilla 1985]. When the velocity ratio becomes too large a stable core becomes more difficult to sustain. At the injector tip small

turbulence generates wave motion across tube end which is illustrated in Fig. 3-15. In Fig. 3-16 the asymmetry of axial flow indicates unbalanced radial pressures. At lower velocities this asymmetry will cause a turbulence which travels up the inside of injector tube and results in an oscillating flow. As the core-sheath differential velocity increases, core diameter decreases but at the expense of faster radial flows, rendered asymmetric by causes such as imperfect nozzle shape [Van Dilla 1985], sheath turbulence, or core drive pulsing [Crosland-Taylor 1953].

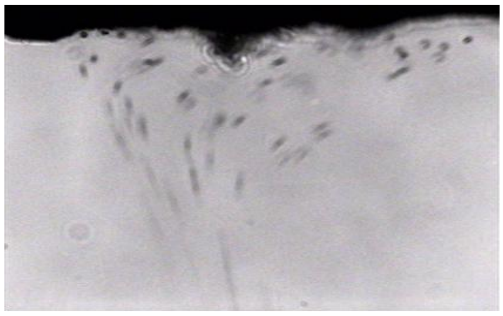

Fig. 3-16 Asymmetric jet of water suspension of 5μm spheres as a precursor to pinch off. Speed of sheath is at 14.7mm/s and that of core at 0.36mm/s.

Smoothness of flow also depends on turbulence generated by supply tube geometries just prior to nozzle. Pinkel et al. [1982] reported that a very long (as much as 25cm) straight sheath supply tube is necessary to allow smooth trajectories for sperm cells being oriented in the core stream prior to a focusing zone. Note that Re is well below the values that would cause departure from laminar flow. The need for smooth surfaces and long tubes in the focus zone approach competes with the need for a short distance between reservoir and injector to avoid particle adhesion or clogging. Fig. 3-17 shows our experimental results on fluid instability at the nozzle as a function of sheath fluid speed. Differential pressure between sheath and core is measured with a high

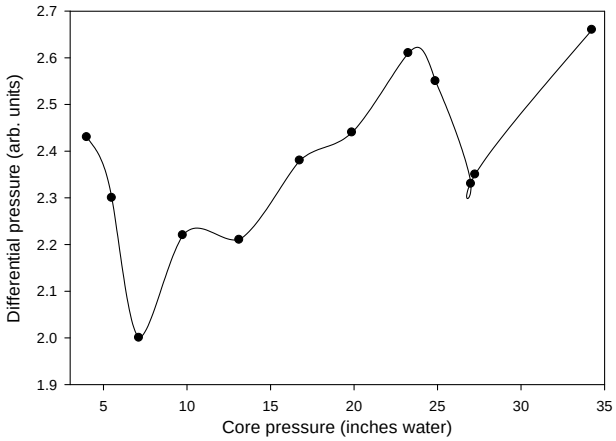

Fig. 3-17 Pressure differential at which core flow will "pinch off" due to flow instability for different values of core speed. Core pressure increase linearly with speed for same nozzle.

sensitivity electronic gauge with a sensitivity of 10 volts per inch of water pressure. From these results, the point of onset of oscillations appears random.

Additionally if core and sheath fluids have different surface tensions then an (imperfectly understood) flow mechanism can also cause pulsing [Ward 2005]. This effect can be exploited for successful micro droplet formation but is undesired for our application [Milosevic 2002]. An early design used in this study involved different fluids for sheath and core for reducing sheath-channel index mismatch. Core fluid was water and the sheath fluid was a water-glycerol mixed solution, serving as an index matching fluid between sheath and PDMS made flow chamber and surface tension could play a role in instabilities as presented in Fig. 3-18. For nozzle dynamics, constant pressure versus constant flow in a water-water system (without surface tension) may still be an issue for instabilities. Experiments clearly show an advantage for constant flow but a theoretical explanation is not available.

Pulsing due to the syringe pump originate from two sources. One is the use of rubber sealed syringe pistons, which tend to grab and release syringe walls at very slow speeds. A lubricated glass syringe with gas tight seal solves the grabbing and leakage problem. The other pulse source is due to gear drive vibration, especially in non helical (spur) gears. For this case it is suspected that at some point in the motor drive reducing gear train there is generated a pulsation which is close to the frequency to which the focusing nozzle responds. Evidence is inconclusive for this issue at present.

There is a minimum inside diameter for the sample injector tube. This diameter depends on particle size, clogging at injector entrance, and clogging from adhesion to injector walls. For very slow core fluid injection rate (0.005μL/s. in 250μm I.D. tube) the particle velocity (100μm/s)

approaches to the gravitational settling speed of ~20μm/s. The terminal velocity of a sphere settling in a fluid is given by

$$u_{terminal} = \frac{\Delta\rho \; g \quad 4/3 \; r_{sphere}^2}{6\eta} \tag{3.38}$$

So a 25μm styrene sphere drifts downward at 19μm/s, a 10μm sphere at 3um/s, biological spheres at half that speed ($\rho_{styrene} = 1.05$, $\rho_{biol.} = 1.025$).

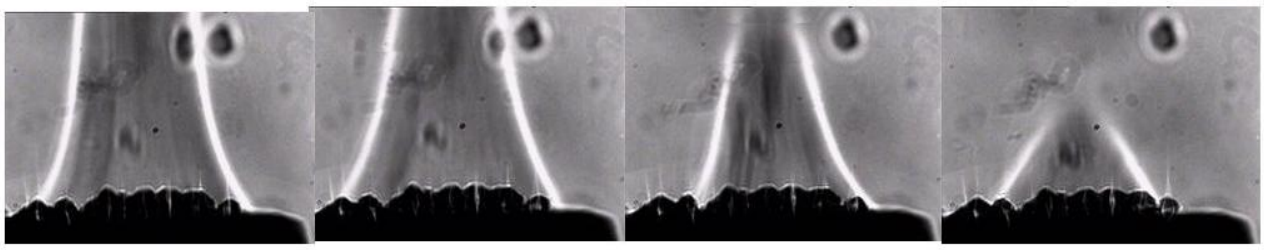

Fig 3-18 Pinchoff oscillation at low speed and high sheath-core flow rate ratio. These images show diminishing core-sheath interface over a period of several seconds for one cycle. The flow rate Q is 1μL/s for sheath and 0.01μL/s for core.

This problem may in fact set the lower velocity limit for particle laden hydrodynamic focusing. A small diameter injector tube will more easily yield a small core diameter since sheath-core velocity ratio can be smaller, and high inside velocities will prevent particle settling. A large diameter injector tube is more prone to asymmetric turbulence as displayed in Fig. 3-16, and low inside velocities will permit wall adhesion (trapping particles but not fluid). However, small diameter tubing is prone to a clogging at the injector tube inlet by clumping cells. Thus it may not be possible to focus to a small diameter a core stream that is also of low speed.

Flow and pressure measurement by regulator, syringe travel and column height

Measurement of flow, pressure, and particle velocity at various points within nozzle and nozzle chamber is problematic because of space limitations and very small pressures. Most

commercial flow cytometers use pressurized gas for fluid pressure control with mechanical pressure gauges and differential regulators. Sensitive gas pressure gauges are easier to operate, but the point where gas meets fluid must be kept constant vertically so that water column pressure does not introduce error. To determine pressures at locations inside the nozzle, core fluid tubes must connect directly to the nozzle. This presents fabrication problems and also requires the fluid-gas interface level in the core tubes to be constant and bubble free, the latter rendered more challenging since pressures are often less than 0.1 inches of water.

An advantage of syringe driven flow is easy measurement of flow rate, typically in units of μL/s (=mm^3/s). Attached to the 1:2000 gear drive motor of each of three channels of the syringe pump is an optical encoder. Its voltage output, proportional to rotation speed, is calibrated based on fluid mass output, syringe diameter, and the variable transmission gear configuration. The variable transmission consists of 26 spur gears arranged in 7 sets, to give 5 reducing speeds and 2 increasing speeds. Therefore the combined gear ratios run from 133:1 to 70×10^6:1. With a linear translator driven by a 20TPI (threads per inch) lead screw; the syringe plunger travel speed varies from 0.12 mm/s. to much less than 1 um/s, the latter exceeding translator stability limits. Flow rates are calibrated by weighing the nozzle fluid outputs.

The unit for gravity generated pressure is the total vertical drop between the surface of reservoir and the drain exit point, driving pressure being developed both before and after nozzle resistance section. This method of fluid drive is simplest and smoothest. However its flow behavior is not constant flow but constant pressure. Anticipating fluid behavior is simpler with constant flow since fluid impedance is complex inside nozzle. The dynamics inside nozzle are very sensitive; for example, any vibration of supply tubing from reservoir will severely disrupt flow which sometimes requires 30 minutes to return to equilibrium. This means pressure cannot

be varied continuously without disrupting flow if it is accomplished by vertically moving the reservoir. By contrast, syringe motor speed adjustment is non disruptive. A combination of syringe flow stabilized by a water column placed at syringe output works well but is cumbersome since overflow must be accommodated.

Pressure measurement and surface tension

The differential pressure between the sheath and core fluids is very small and difficult to measure but estimation is relatively easy by surface tension pressure of exit droplets. It was noticed that at low speeds but of high sheath-to-core differential velocities, γ, core flow pulses on and off at the same rate as exit droplets, as shown in Fig. 3-19. Pressure inside a spherical drop of radius R is given by the Young-Laplace equation as $p= 2\alpha / R$, in which α (=70 dyne/cm) is its surface tension [Batchelor 1967] Therefore for drops of 5mm diameter, pressure differential between sheath and core must be less than ~ 0.2 inches of water pressure (50 Pa). By comparison most flow cytometers operate with Δp=14 inches water (3500 Pa). Submerging the drain end will eliminate pulsing.

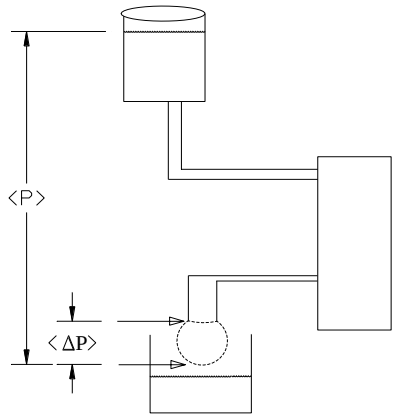

Fig. 3-19 Schematic of the reservoir of fluid passing through flow chamber in the middle and exiting into a catch basin. ΔP is the pressure in column before and after droplet breaks free of tube end.

Electronic pressure measurement

Pressure measurement using piezo-electronic sensors was studied. Silicone pressure sensors (XPC05DTH, DC001NDC4 of Honeywell and DCXL30DS of Allied Electronics Inc.) were configured to measure core pressure, differential pressure, and sheath pressure. The differential pressure sensor was sensitive to 0.02 inches water (5 Pa). However its performance was inconsistent for several reasons. One is that

direct access inside the flow chamber near the hydrodynamic focusing region is mechanically difficult and also interferes with the dynamics. Furthermore, indirect pressure sensing at the input and output feed tubes generates spurious pressure losses through resistance of associated access tubes. Also, these sensors function with active surfaces (piezo film with printed circuitry) which are incompatible with ionic fluids used as cell culture medium. To counter this problem, a dense, inert, and immiscible fluid, dibromobenzene, was injected into sensor ports to shield them from direct water contact. But with Δp on the order of 0.1 inch water, plumbing variations, possible bubbles inside the sensor, and variations of fluid density resulted in inconsistencies in the measured results. Note that a bubble in a small tube between two fluids of different surface tension can act as a blockage and/or change pressure due to its density variation.

Measuring particle velocity and core stream diameter

Speed of core fluid is measured indirectly from the total core flow rate Q and diameter of core stream at the speed measurement point. The latter can be determined from images of a fluorescence tagged core fluid or of a core fluid with a different refractive index from the sheath. Note that as diameter approaches $10\mu m$ or $20\mu m$, its large curvature makes index mismatch more pronounced and hence visible, but for a dyed fluid the diminishing absorption path length means loss of contrast. This is not the case when the core undergoes planar focusing (e.g. a microfluidic chip with vertical channel walls) [Yang 2007]. Furthermore dyed fluids are often incompatible with biological cells [Sundararajan, 2003].

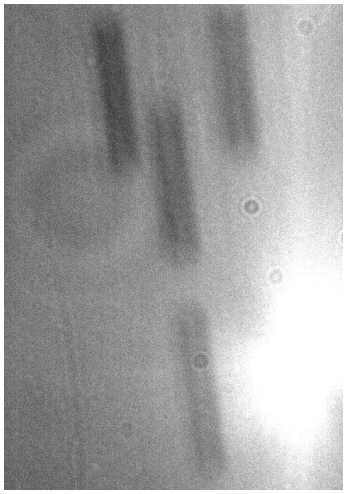

Fig. 3-20 An image with non-coherent illumination of $5\mu m$ spheres moving at 15mm/s with a 2.0 ms exposure time. Flow speed is determined by the length of blurred track.

The most direct method of measuring both speed and core stream diameter is by time exposures of entrained particles as shown in Fig. 3-20. Both stream diameter and velocities are measureable and the velocity distribution cross section will be part way between square shaped (plug flow) and parabolic (Poiseuille flow). However, if core stream position itself is drifting laterally over time then a series of images may present displaced core at multiple times and one needs to be careful in image analysis for determination of the instantaneous core diameter. Also at higher speeds particles can be too infrequent or dim to capture. Hot wire anemometer, laser scanning confocal microscopy, and laser Doppler anemometer [Rankin1983] are more accurate methods for flow speed measurement, but were not used in this study.

§3.4 Fluid dynamic modeling of two-phase flow in round and square channels

By two-phase flow, we refer to the cases in which the core and sheath in a laminar flow are fluids of different viscosity and refractive index. This section presents the results of diffraction imaging of particles flowing in the PDMS flow chambers with round and square shaped channels. Several problems were encountered but the most severe was distortion of images by the presence of nearby channel walls as illustrated in Fig. 3-11. For this reason the study was moved into another direction with the new chamber design to be discussed in Chapter 4 after preliminary experiments which are discussed here. It is possible that this direction of chamber design could be useful for future development since one group has reported positive results [Neukammer 2003].

Difficulties of maintaining particle orientation by nozzle in two-phase flow

Fig. 3-21 shows an image of 10um spheres acquired with a long exposure time under non-coherent illumination. The waviness of the blurred track of the moving sphere appears to be caused by either tumbling or sideways motion. Tumbling of particles was found as a problem to solve for oriented particle flow cytometry [Dean 1978]. In that study, scatter from sperm cells was measured using known cell orientation. The process required extremely long sheath and core feed tubes to eliminate tumbling due to turbulence. In Fig. 3-21 the particles could either be tumbling or undergoing oscillation under sideways turbulence with a fixed axial orientation. If a diffraction image is acquired over a long exposure time then the particle motion, especially tumbling, will affect the image quality.

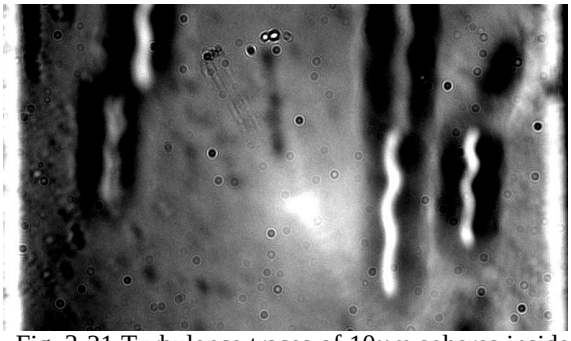

Fig. 3-21 Turbulence traces of 10μm spheres inside microchannel, whose walls can be seen at left and right edges of image.

Two-phase flow was used to eliminate index mismatch at the channel walls. The water-glycerol index matching fluid for the sheath had both greater viscosity (x6) and density (ρ=1.12) than those of the core fluid. If the flow is fast gravity has negligible effect and the orientation of flow chamber relative to the earth is not an issue. When the flow chamber was configured for a downward direction of flow at low speeds then the flotation of the less dense water core could invert flow direction as shown in Fig. 3-22, and cause mixing of core with sheath. The convoluted flow will not unravel itself, even at high speeds, without complete flushing of the flow system. A further problem with convolved flow is that the particles, normally separated from channel wall by the sheath, now adhere to the walls and cause degrading of both light

passage and smoothness of flow. Therefore operating a two-phase flow chamber requires a upward flow. Even then forming a laminar flow requires careful startup of the flow since complex flow patterns can take over laminarity even when Re is very small.

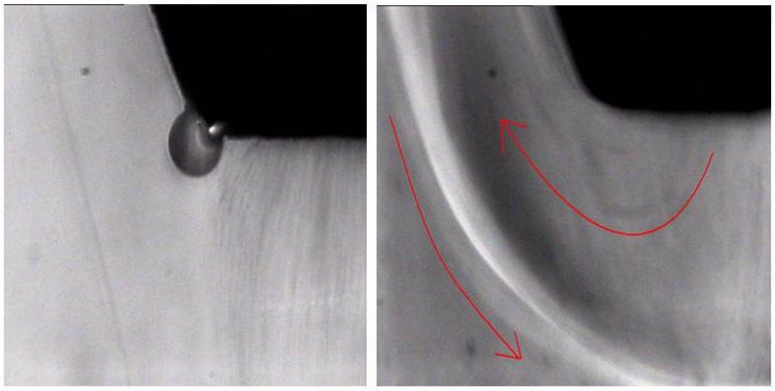

Fig. 3-22 Images of nozzle flow problems at injector tip. Left image shows a 5μm sphere cloud streaming down with a sheath streamline (black trace) enveloping along outside of injector. A gas bubble sticks on edge. The image at right shows a cloud of spheres flow back up along outside of injector.

Flow velocity and core diameter for two-phase focusing

From Equation (2.20), the resultant flow speed and core stream diameter for a two-phase flow will be higher and smaller, respectively, than for a flow of sheath and core fluids of the same viscosities. The two non-coherent images in Fig. 3-23 with the same exposure time of 0.02s show core fluids of sphere suspensions under identical flow rates for the core and sheath except that in second image the sheath is a 50% water-glycerol solution (by volume) of higher viscosity. From the track lengths, the more viscous sheath has accelerated the spheres by a factor of about 1.8. The core/sheath flow rate ratio, z, is known to be 0.14 so, from the images in Fig. 2-3, the relative diameters, w, will be 0.25 and 0.21 for the water-water and water-glycerol flows respectively. The square of the diameter ratio of $w_{wtr\text{-}wtr}/w_{wtr\text{-}glycl}$ at 1.4 for the sheath

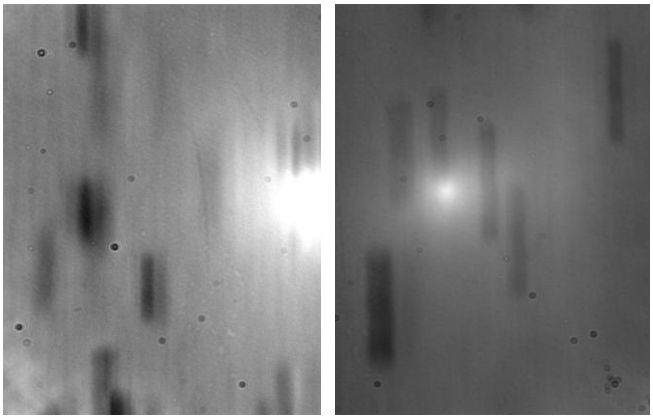

Fig. 3-23 Effect of sheath viscosity on diameter and speed of core fluid of water suspension with 5μm spheres. Both images are acquired at the same location downstream from injection point: (a) water as the sheath fluid; (b) 50% water glycerol solution as the sheath.

should be the inverse ratio of the speeds measured as 1.8 as shown in in Fig. 3-23. One source of disagreement is that the point of measurement is still within an accelerating region of the fluid with large uncertainty in speed measurement. In order to have the fully developed two-phase Poiseuille flow of Fig. 2-2, a channel of constant diameter over a distance of at least 80 radiuses is needed [Andrade 1937]. With a higher viscosity sheath, the core stream diameter can be expected to be compressed to a smaller value. From Fig. 3-24 the core diameter can be estimated by the side to side jitter of images, assuming that the jitter amplitude is equals to the core stream fluid diameter.

One may also note that the images extend outside channel walls. Flow rates were 0.04uL/s for the sheath and 0.014uL/s for the core based on calibrations from a similar microchannel, giving a flow rate ratio of z=0.35. Using Eq. (2.20) and a relative sheath viscosity of 6, the relative cores diameter should be w=0.186. From the series of images in Fig. 3-24, the ratio of core to sheath diameters is measured as 0.23. By comparison a water-water combination would give a much larger diameter ratio of 0.28. Studies on two-phase flow with the sheath confined in a channel have been reported in which experimental data was compared with numerical calculations [Rankin 1983, Vempati 2007] . The predicions by Vempatti et. al. only loosely agree with the experimental results shown here but the readers are reminded that we consider here a square shaped channel.

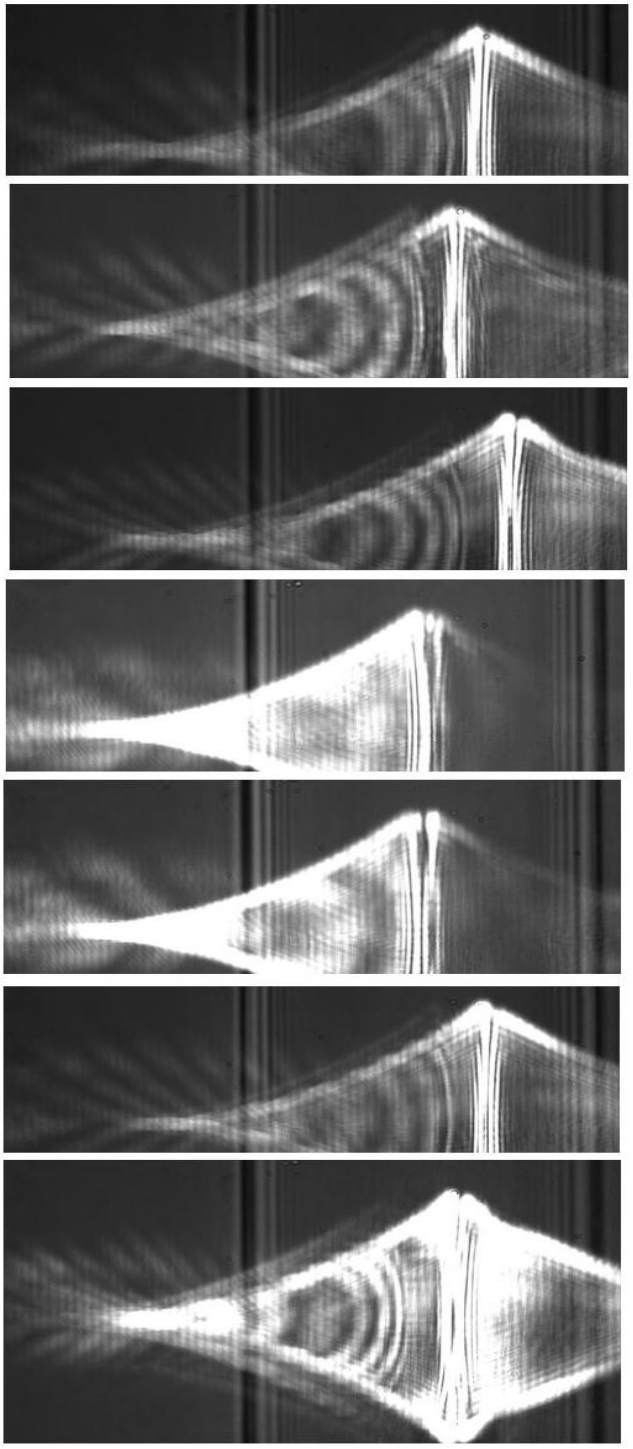

Fig. 3-24 A series of flowing 25μm spheres in core within water-glycerol sheath, which is inside a 200μm square microchannel. Channel walls are black vertical lines. Core width is indicated by the maximum left-right jitter of the sphere image centers.

Chapter 4 Development of a three-flow chamber and imaging of spheres

This chapter covers the fluidic and optical design and performance test of a three-fluid flow chamber used to realize the submerged jet design for high-contrast diffraction image acquisition.

§4.1 Chamber design

This flow chamber was designed specifically to eliminate the optical artifacts in diffraction images caused by the spurious scattering at the sheath-channel interface in the original PDMS capillary flow chamber discussed in last chapter. Recent experimental studies demonstrate that diffraction imaging of micro particles of dimensions close to wavelength with coherent light excitation [Phillips 1970, Orvyn 2000] requires isolation of the imaged particle from nearby index-mismatched interfaces. The new flow chamber design also incorporates an integrated core fluid reservoir to enable more reliable passage of particle suspensions prone to settling or clogging.

Fig. 4-1(a) shows a schematic of the design with a core drive fluid (C) driven into a sample reservoir (cyan colored). The reservoir itself is a long and thin glass tube of 10cm in length and 2mm in I.D. and the core drive fluid is made of deionized water pressurized in a syringe pump. Thus the particle concentration of the core fluid in the top part of the reservoir, where the core drive fluid enters, is reduced due to dilution over time. But because flow rates in our experiments are very low, the dilution is inconsequential for typical experimental run times. The long tube of the sample reservoir prevents complete settling of the particle suspensions without stirring for up to 2 hours for particles less than ~10μm. Since the core fluid exits at the bottom of the reservoir,

any particle settling can augment the flow and counter the decrease of particle concentration due to the dilution by the core drive fluid.

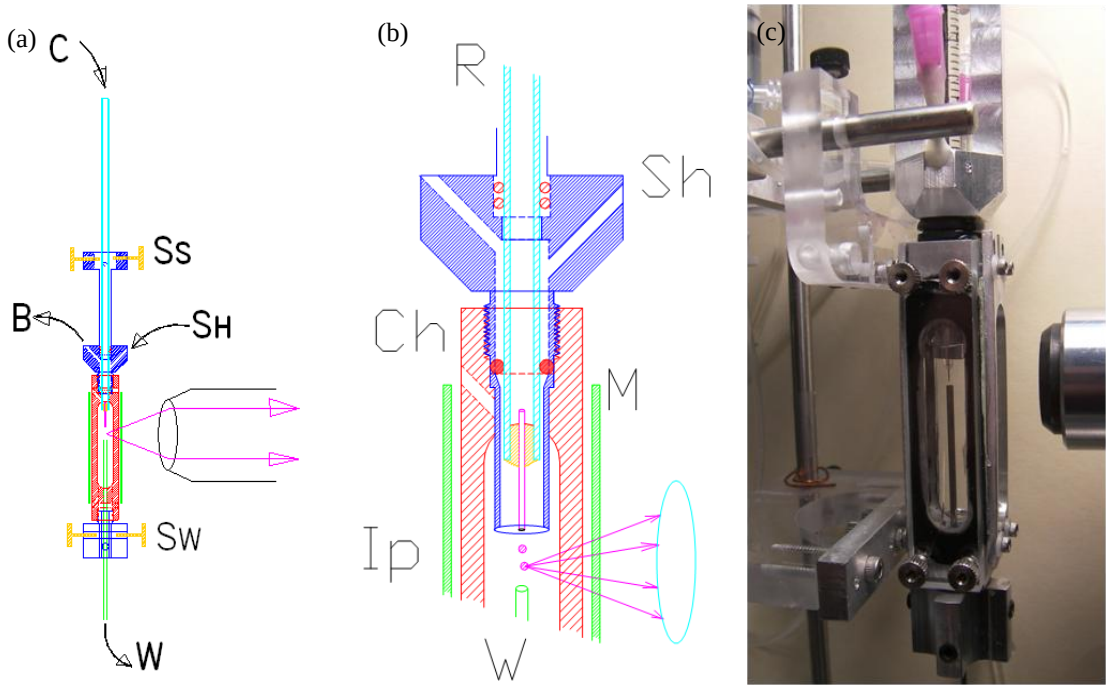

Fig. 4-1 (a) The glass reservoir (cyan colored) at top of the flow chamber with the steering screws (Ss) to center injector needle within sheath nozzle; sheath entrance port (Sh), and debubble port, B, in top of chamber; steering screws (Sw) for aligning nozzles; and waste exit needle, W. (b) A close-up view of interrogation point P inside chamber (Ch). Sheath flow surrounds and accelerates core ejected from needle (purple colored). (c) Ejector and receiver tubes visible inside glass lined flow cell. Entire assembly is translatable in x, y, z directions.

A 1cm long stainless-steel injection tube of I.D. ranging from 100um to 500um is sealed to the bottom of the sample reservoir. Its lower end is centered coaxially with sheath injector by steering screws (Ss). The short and straight injector length minimizes adherence of particles to tube wall and its end is ground to a smooth taper to reduce turbulence. The bottom of the reservoir is sealed into the flow chamber with O-rings which makes it efficient to separate the reservoir with its sample contents from the chamber. The flow chamber framework is machined from a single 15mm square aluminum block. Glass microscope slides are clamped against the four sides of the frame for optical access and can be easily disassembled for cleaning of the

chamber, as displayed in Fig. 4-1(b). Top of the chamber has provision for bubble removal (B) and sheath injection (Sh). The sheath fluid serves as a focusing means to the core fluid at two locations, radially directed momentum transfer at the core fluid injector point and flow accelerations at the exit tube, as can be seen in Fig. 2-8. The exit tube is also aligned coaxially with injector tip by steering screws (Sw). A gap between injector and exit points is adjusted to 1mm to maximize stream lateral stability (wavering) while allowing a focused laser beam to excite the particles sufficiently far from the tube ends to prevent light reflections.

A particularly difficult task is to fabricate the injector nozzle tip which is made from stainless-steel hypodermic needle tube of sizes ranging from 90 μm to 500 μm I.D. (33 gauge to 21 gauge). To do this a precision lathe chuck is used to drill a needle sized hole in a brass plate to hold the needle. The spinning needle on the lathe is then held by both the chuck and brass plate to keep it from flexing. A Dremel tool grinder is held against the spinning needle while it is viewed with a microscope mounted over the assembly. A grinder is used only to flatten the needle end. Tapering is accomplished with ~600 grit sandpaper held against the needle without any mass backing behind the paper. Thus sandpaper tracks needle end vibrations without involving inertial forces that would grind unevenly. Since the smallest sized needle has a 0.017 inches I.D. a deviation from concentricity of 0.001 inch generates a significant asymmetry in needle tip which in turn disturbs the flow symmetry and laminarity. Therefore, extreme care must be exercised to assure quality of the needle end.

§4.2 Development of the imaging unit

The entire flow cytometer system is mounted on an optical table. The microscopic imaging unit and the flow chamber unit are mounted with two sets of translation stages to allow independent 3D motion for alignment. Fig. 4-2 is an overview of the optical and electronic pathways involved.

Light path and hardware

The particles carried by the core fluid inside the flow chamber cell were excited initially with a HeNe laser of 5mW in power and 633nm in wavelength which was later replaced with a solid state laser of 50mW in power and 532nm in wavelength (Snake Creek Lasers). Cell imaging requires much larger excitation power because of the weak scattered light. The incident laser beam is expanded and then focused onto the core stream with spherical lens of focal length ranging from 60mm to 250 mm. The maximum incident power at the wavelength of 532nm was measured to be 46mW in a focal volume of 25μm diameter in air (10%-90% transmittance using a knife-edge method) by about 100μm long with a lens of 60mm in focal length. Other lenses of longer focal lengths give considerably less incident irradiance but also less stringent alignment requirement.

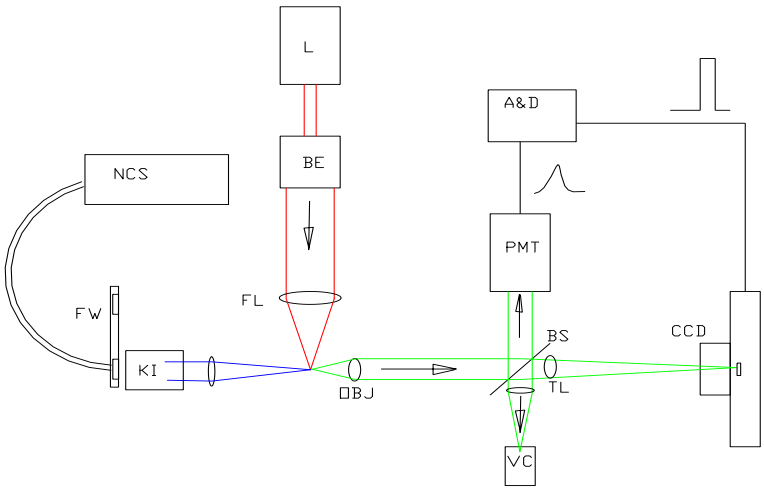

Fig. 4-2 Schematic of the optical setup: L=laser, BE=beam expander, FL=focusing lens, KI=Kohler illumination, NCS=non-coherent source, FW=filter wheel OBJ=microscope objective, CCD=CCD camera, TL=tube lens, BS=beam splitter, VC=video camera, PMT=photomultiplier, A&D= amplifier and discriminator.

The core stream was also illuminated by a non-coherent light beam using a fiber-coupled lamp light source (Dolan-Jenner DC950) for aligning the system. An in-house built Kohler illumination assembly focused the non-coherent light beam onto the gap space in the flow chamber to illuminate the core flow stream. The bright-field image is used to searching for the reference position of the microscope objective and for measurement of the particle flow speed and position by means of long-exposure tracks imaged on the CCD camera.

Microscope imaging unit

The microscopic imaging unit was assembled with a 50X objective of 0.55 NA and 13mm working distance (Mitutoyo) and two tube lenses as shown in Fig. 4-3. The objective is designed with an infinite back focal point that allows insertion of a beam splitter in the light path before the tube lens without distortion to the output light. The image passing directly through beam splitter is focused by a tube lens of 200mm focal length onto a cooled CCD camera (U2000, Apogee), and light reflected from the beam splitter is focused in another arm of the imaging unit by another tube lens of 60mm in focal length to a video camera (XC-75, Sony). Thus the image from the video camera is magnified about three times larger than the image from the CCD camera. A photomultiplier tube (PMT) is used to detect the light reflected back from the video camera chip which is sufficient to generate a pulse signal to trigger the CCD camera

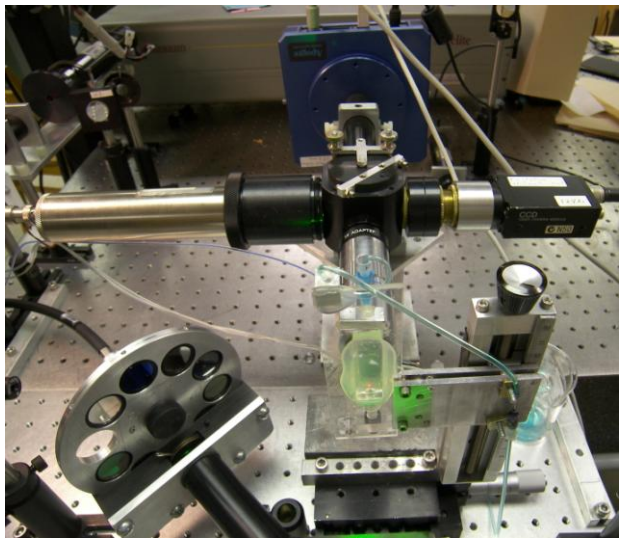

Fig. 4-3 Imaging unit with non-coherent light source using a filter wheel and Kohler illumination. The flow chamber (green colored); beam splitter ports (black); PMT to its left and video camera to its right. CCD camera (blue colored) is at rear.

for acquiring diffraction image data while the video camera provides continuous image stream for monitoring or alignment. All optical mounts and tubes are black anodized against spurious internal reflections. Since the focal lengths of the tube lenses are very long, the camera can be moved somewhat along optic axis without loss of contrast, permitting slight variability of the image magnification.

The side light scatter pulse signals from a particle entering the focal spot of the incident laser beam are detected through the imaging unit by the PMT which is biased at 750V. Its output pulse is amplified by a dual channel logarithmic amplifier and monitored on an oscilloscope whose trigger level can be adjusted to discriminate pulse heights. The sweep signal gate of the oscilloscope is utilized to trigger the CCD camera with exposure time controlled by software. Thus the trigger pulse size, shape display and discrimination are all accomplished by a single oscilloscope.

Flow chamber mounting and translation

It is required to align the focused incident laser beam, the core stream carrying the flowing particles and the field-of-view (FOV) of the objective all together. The flow chamber needs to be supported rigidly at the crossing of three optical axes with several accompanying fluidic components. By coupling the drive shafts of two precision rack and pinion vertical translators, axis C in Fig. 4-4, a translator was thus assembled that enabled open access to the flow chamber suspended between the two translators. The flow chamber, stirring mechanisms, sample reservoir, and peripheral plumbing components can thus be all moved as a unit along the three axes of x, y, z as shown in Fig. 4-4. The imaging unit is supported by another assembly of two translation stages to allow alignment against the flow chamber along the x-axis and vertically along the z-

axis. Finally the laser focusing lens is supported by a translation stage for fine alignment of the focal spot into the core stream.

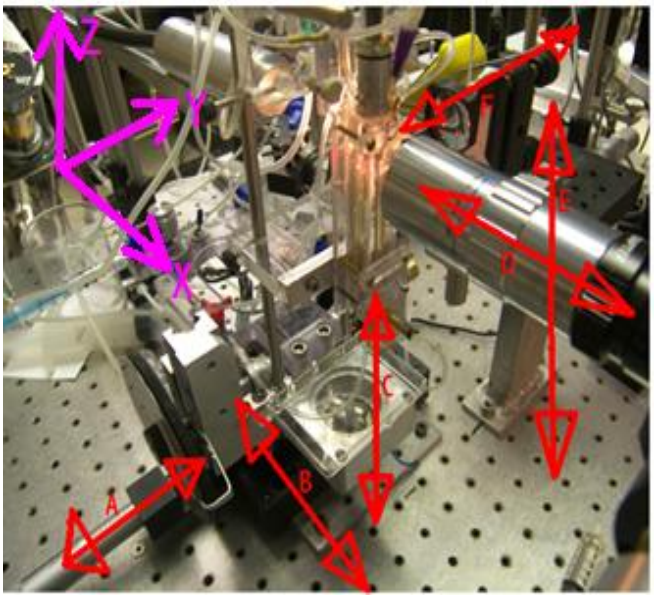

Fig. 4-4 A photo of the translation stages for flow chamber alignment. Six degrees of freedom are necessary: A,B, C for flow chamber; D and E for objective; and F for focus the incident laser beam on the core fluid.

Another triggering mechanism and optics system (not shown) was built that used a second laser beam crossing the core flow upstream from the interrogation laser beam as a probe beam for triggering the CCD camera. Interruption of transmitted beam by a flowing particle was detected from the forward scatter of the probe beam and then delayed appropriately before triggering the camera. Such a method requires highly consistent stream flow so that the flowing particle fulfills its predicted trajectory. This approach was not used in our later experiments since we found the side scatter of the interrogation beam is sufficiently strong for triggering of the CCD camera

Alignment process

Fig. 4-4 shows the six degrees of freedom necessary to excite a flowing particle in the flow chamber and acquire diffraction image data. The alignment process is critical for placing the focal spot of the interrogation beam into the core fluid and acquiring diffraction images consistently centered in the y-z plane in the FOV. Locating and retaining location of the core stream in the chamber for focusing and alignment is accomplished with several techniques. Firstly, dye can be used in the core stream to locate its y position accurately but x (related to the

objective positioning) position only weakly since core stream edge is optically blurred under non-coherent illumination due to the large focal depth. Growth medium containing fluorescent fetal bovine serum emits fluorescent light under a green beam excitation at 532nm which make it visible in comparison to the transparent sheath fluid. This is a better approach for alignment than dying the core with the methylene blue dye and since the dye may interact with the sample particles. For biological cells, growth medium is a possibility but may generate background fluorescence light in the diffraction image unless a wavelength filter is used. Another aligning means is based on viewing the flowing particles in core fluid which can reveal not only y but x-axis by their appearance as brought into the focus of the objective. Cells will exhibit either a shadow minimum or a surface glistening when focused using non-coherent light illumination. However, particle concentration in the core fluid must be very high to give continuous focusing feedback for alignment. This in turn presents problems for diffraction image data by generating interference patterns due to clustered particles or multiple particles in the FOV. By using a fluid of refractive index different from sheath fluid core stream will provide tracking information at the interface between the fluids, but bio-compatibility with cells could be an issue. Saline solution or water-glycerol solutions are possibilities.

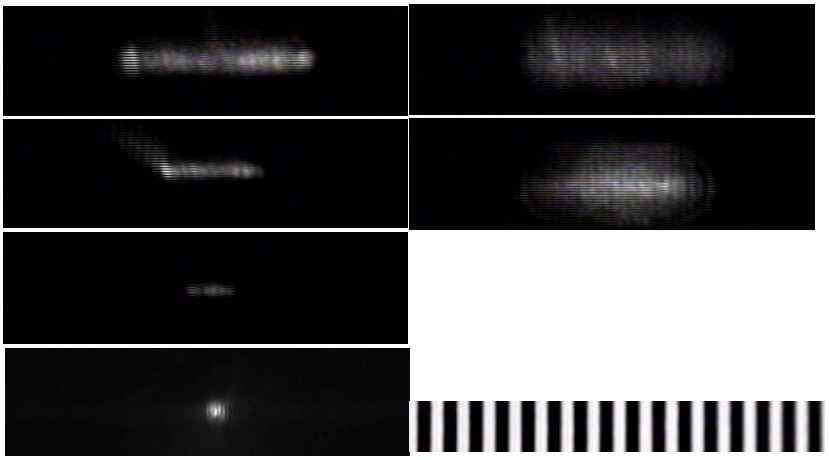

Fig. 4-5 Fluorescence images of the focal volume of the incident laser beam crossing vertically flowing core fluid. Left panel: four positions of the beam in the core fluid as it is focused from 74μm (top) down to 8μm diameter at bottom. Right panel: defocused laser with either its focusing lens (top) or with the objective (middle) translated. Bottom right: 10μm per line glass slide.

Under all conditions a problem for accurate alignment is that the tracer

fluids become less discernable as the core fluid advances and becomes focused inside the sheath. Lost visibility is due both to lessening of absorption because of diminishing core stream diameter and to lessening of interface contrast due to mixing of core with sheath. Note that the core stream can drift in two directions along the x- and y-axes relative to imaging unit, so continuous monitoring and adjustment of objective's position may be necessary. However for a core fluid that is confined within a microchanneled flow chamber there will be no drift. Locating sample stream is therefore easier in latter case.

Fig. 4-5 shows the fluorescence of core stream with a green laser beam excitation under various conditions. All six adjustments for alignment as well as core stream diameter measurement can be made from these images. In the case of alignment of a stationary target the shadow of particle can be imaged on a screen directly beyond flow chamber in the forward direction. When a sphere or cell is perfectly centered within the laser beam it will appear as a set of concentric rings on a screen.

§4.3 Measurement of scattered light with imaging sensor

Fig. 4-6 is a schematic view of the interrogation point of a flow cytometer. The laser beam, approaching from left illuminates the particle, moving upwards at speed u. Scattered light perpendicular to the incident beam radiates in direction D. There are a number of competing factors influencing the conditions for ideal interrogation of a particle in a laminar flow stream by

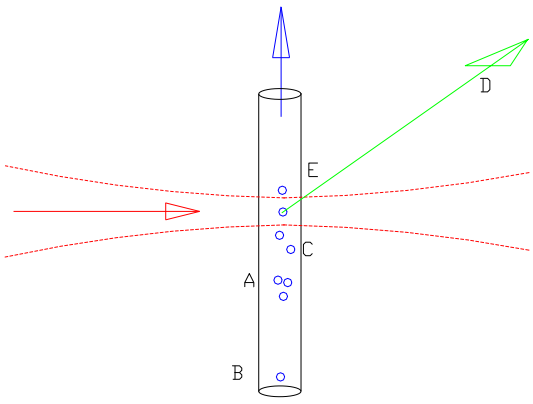

Fig. 4-6 Factors influencing imaging quality at interrogation point, E. Particles at C outside of focal volume scatter light originated at E and thus interfere with image signal.

an excitation beam. We seek maximum information about each target particle and a large number of targets. This latter is because pattern recognition is being applied to living systems which have high individual variability. Therefore it is necessary that the imaged particle is isolated from other particles, isolated from nearby index-mismatched interfaces lying in the objective's focal plane and illuminated uniformly. Any displacement of the particle from the focal spot in z direction distorts the image symmetry; in y direction distorts focus; or in x direction distorts screen centering. Also issues of particle tumbling or orientation are possibly significant.

Coincidence issues [multiple particles in beam]

In order to reduce coincidence of particle illumination, as at point A in Fig. 4-6, the average speed ū and particle concentration must be adjusted so that the detection region length Δz has an average number of particles in it at any moment, γ, of just one. A typical example might have ū =100 mm/s., Δz =20 μm, and N=5000 as number of particles per second. Thus

$$\gamma = \Delta z \frac{N}{\bar{u}} \tag{4.39}$$

However if we wish the probability of coincidence to be less than 0.01 then by Poisson's law,

$$p = \gamma^n \frac{e^{-\gamma}}{n!} \tag{4.40}$$

This is the probability of a particular number of particles in the detector span, Δz in which the average number is γ. In this case γ is about 0.2, so with a core diameter of 25 μm at 100mm/s the concentration of particles needs to be 2×10^7 particles /ml^3. This will give a probability of 0.16 for a single event at 5000Hz and an acceptably low probability of a coincidence event (two inside

the detector span) of 0.01. With diffraction images there is the possibility of a nearby particle generating optical artifacts [Ashkin 1981, Phillips 1970]. Under this constraint the nearest particle would need to be perhaps 1 mm, single events would then average 100Hz and particle concentration reduced by a factor of 5.

Optical artifacts and focus

Another factor that generates noise in coherent light imaging is optical artifacts from nearby surfaces. These surfaces could be reflective or diffracting channel walls, a refractive index mismatch between adjacent fluid streams, and possibly chemical films attached to the target particles. A closed cell flow cytometer uses an observation point inside a micro channel anywhere from 50 to several hundred microns inside dimension. Experience indicates that the lower end of this range will cause artifacts. Additionally if the channel walls are curved then image wavefront is refracted. For an integrating detector this is tolerable but not for creating an image. Since curvature of walls or coaxial stream interfaces is so large at radii of 10 to 100 μm, even a small relative refractive index of 0.001 is easily visible and will cause artifacts. [Thom 1970]

A major factor in image quality is focus. Randomly dispersed particles in the feed suspension are confined by hydrodynamic focusing to a single file, cylindrical column. However, as core diameter approaches particle dimensions, the particle edges protrude into the sheath. Minimum deviation from core axis will be about 1/2 diameter after which the particles escape core boundary into the sheath.

The beam diameter on y axis must be large enough to fully intersect particle. For typical integrating detector flow cytometers this is not so critical since total pulse energy is measured. For an imaging detector the relative irradiance across image defines the object and so needs to be

independent of observation mechanics. Thus a cell of diameter 10 μm moving at 100 mm/s requires a Gaussian beam diameter of perhaps 20 μm giving an exposure to a smaller more homogeneous part of the beam. In order to travel less than 1/10 its dimension during exposure the $\Delta\tau$ must be 10 μs. Furthermore the exposure should be timed to center of beam so that a flatter part of irradiance distribution is used and not an asymmetric portion. This last requirement constrains particle speed deviation which in turn relates to core diameter since core speed is not constant but parabolic across its diameter.

§4.4 Calculating light irradiance to camera from an illuminated particle

Fig. 4-7 is a composite schematic of light scattered at 90^o into a microscope and the resultant image. The polar graph is logarithmic, so that the objective receives only about 10^{-11} of incident irradiance. The fringes are cones of revolution about laser axis with cone apex at origin, therefore flat plane image of fringes are warped at center.

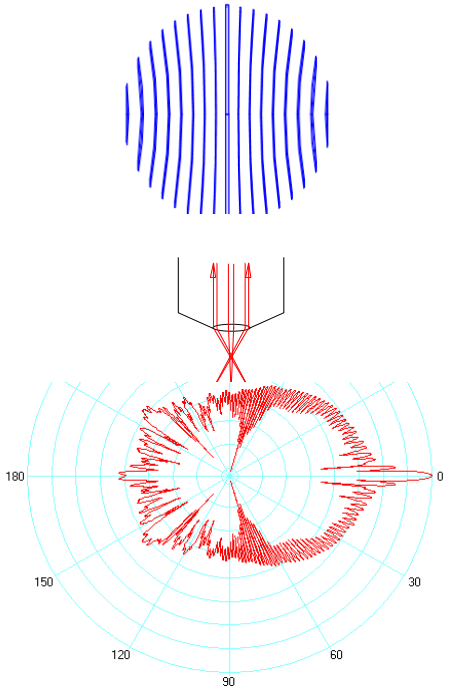

Fig. 4-7 Image generated by 90^o Mie scatter into a microscope objective (upper left). Polar log graph and sketch of projected image are of 25μm polystyrene sphere, n=1.59, in water. Laser beam is from left.

The light available from a scattering particle to a microscope objective is modeled as a spherical wavefront illuminating a concave detector on the objective lens surface. A plane wave propagates from –x direction and scatters at origin, Fig. 4-8. From Mie calculation we have irradiance as a

function of angle θ measured from +x axis, $I\ \theta$, and at distance R from origin. The objective lens on the z axis is at a distance F (lens working distance WD) from origin. From Fig. 4-8 the area of sector S is

$$A_{sector} = 2R^2 sin\theta \cos^{-1}\left[\frac{1}{(R/F)\sin\theta}\right] d\theta \qquad (4.41)$$

Therefore total flux passing into lens is

$$P_{Lens} = \int I(\theta)A(\theta)d\theta = \left(\frac{\pi}{180}\right)^2 2R^2 \int_{57}^{123} \sin\theta \left[\cos^{-1}\left(\frac{1}{1.25\sin\theta}\right) d\theta\right]. \qquad (4.42)$$

For lens-CCD magnification, M=1, incident laser irradiance I_L and NA=0.55,

$$I_{Average} = \frac{P \bullet M \bullet I_L}{\pi \bullet \Re^2}(0.69) = 2.75\,x10^{13}(M)(P)mW/m^2 \qquad (4.43)$$

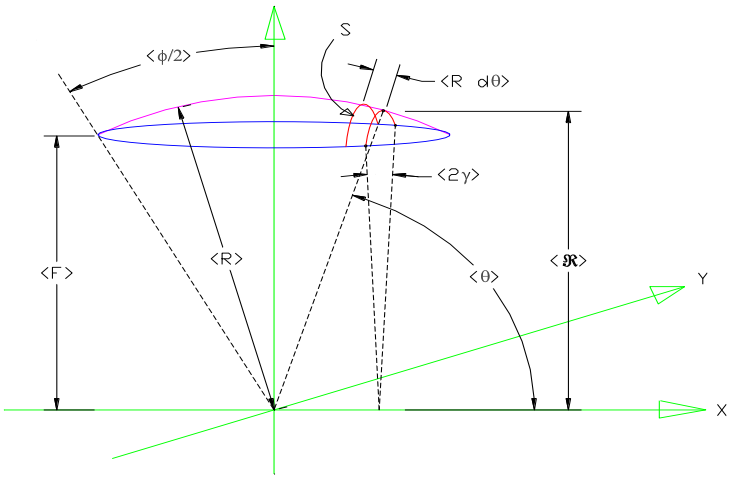

Fig. 4-8 Geometry for projection of scatter into concave microscope objective lens, purple, of curvature radius R. Target sphere is at origin, laser beam from –x direction, scattered into objective of cone angle ϕ/2 and focal length F. Arc S at angle θ from laser axis is of width Rdθ and of length 2γ(ℜ) in which ℜ=Rsinθ.

As an example the Mie calculations for three spheres of diameters 25μm, 10μm, and 5μm are calculated. Using Mie Plot 4001 [Laven 2010] software the scattered irradiance versus angle is integrated over the surface of a microscope lens focused on the sphere center. An unpolarized

incident plane wave (sun) excitation of λ =633nm scatters from these spheres in a medium of water, index of refraction n=1.33. Incident light is from 23 micron diameter (10%-90%), 3.8mW laser beam modeled as having a flat cross section at an irradiance of 9.15 x 10^6 W/m^2. Sphere indexes are either n=1.37, typical of biological cells, or n=1.59 Polystyrene from Duke Scientific. Energy flux is given in joules x 10^{-9} during a 1 ms exposure time.

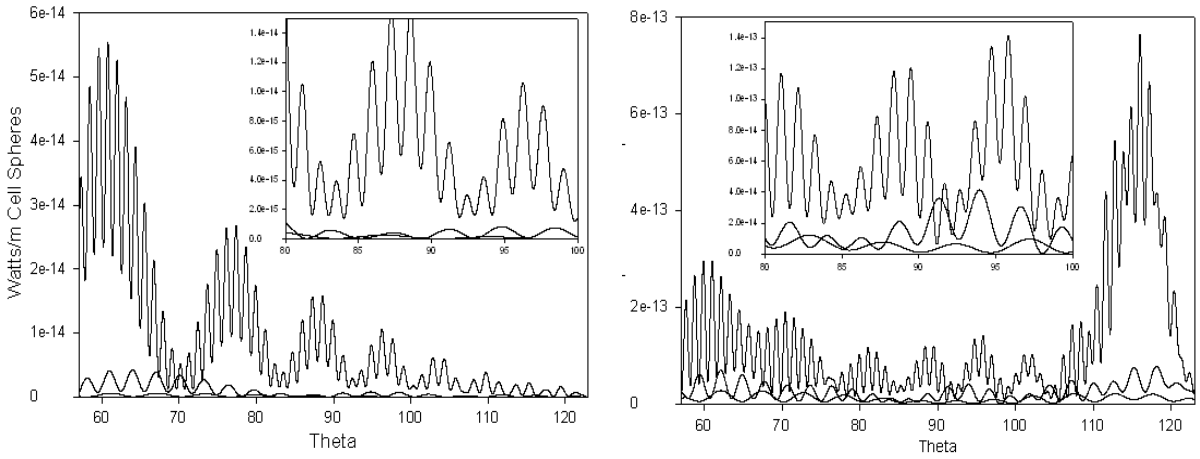

Fig. 4-9 Plots of calculated irradiance intercepted by a microscope objective by Mie calculation. Right is 5, 10, 25 μm polystyrene spheres, n=1.59; left is 5, 10, 25μm biological spheres, n= 1.37. The units are in W/m^2 with wavelength of excitation beam at 633nm and scattered irradiance values at 0.013m and scatter angle between 57°

Table 4-1 Calculated irradiances (mW/m^2) of scattered light by spheres

Diameter (μm)		**25**	**10**	**5**
Refractive index n=1.59 (polystyrene)	**Averaged irradiance**	234	46.8	19.3
	Maximum irradiance	1182	273	91
	Irradiance at θ=90°	182	27.3	18.2
Refractive index n=1.37 (cell)	**Averaged irradiance**	16.2	1.51	0.275
	Maximum irradiance	273	18.2	2.25
	Irradiance at θ=90°	27.3	1.82	0.273

Fig. 4-9 plots the irradiance in W/m^2 intercepted by the objective lens for polystyrene spheres and cell-like spheres. Peak values are lower limits of fringe imaging possible. Area under curves is average imaging irradiance. Results are summarized in Table 4-1 in which average irradiance is in mW/m^2 at CCD from scatter of a 9.1x10^6 W/m^2 excitation source. Also given in the same

table are the approximate peak irradiance of fringes within the numerical aperture of the lens; and irradiance of peak at the scatter angle of 90^o. It can be seen that biological cells will generate 15 to 70 times less available imaging light than polystyrene spheres.

Light Scattered by the flowing particles

Fig. 4-7 is a composite schematic of gathering side light scatters from a sphere with a microscope objective. A diffraction image depends on the power of incident laser beam, scattering cross section of the illuminated particle, time of flight of the particle through the incident beam, optical elements of the imaging unit and camera sensitivity. This section deals with Mie theory based calculations and experimental considerations related to the acquisition of diffraction image data by a sphere in anticipation of predicting the measurement limits with cells.

Mie based calculation of fringe peaks in the scattered light

The imaging unit used in this study has the following relevant specifications: quantum efficiency (QE) of the CCD sensor at 532nm = 53%; shortest exposure time = 1ms; pixel dimensions = 7.4um x 7.4um = 5.5 $x10^{-11}$ m^2; number of pixels = 1600 x 1200; pixel depth = 16-bit or 0 to 65,535 in pixel value; CCD sensor dimensions = 11.8mm x 8.9mm with 15mm diagonal; background noise in pixel value = 3000 (cooled) or 3440 (uncooled); objective NA = 0.55 or 33^o half angle in air; front lens diameter = 14mm; working distance (WD) = 13mm. Therefore the CCD camera used in this study can output pixel values up to 65,535, corresponding to a full well capacity of 40,000 photoelectrons per pixel of $5.5x10^{-11}m^2$ in area. So an increase in pixel value of 1,000 corresponds to 615 photoelectrons generated in one pixel if one ignores the background noise. At $3.73x10^{-19}$ J for the energy of one photon at 532nm, a light pulse of 1160 photons is needed to increase the value by 1000 at one pixel which yields the

pulse energy as $4.33x10^{-16}$ J. The scattered light arriving at this pixel must then have a fluence of $7.9x10^{-6}$ J/m^2 to generate the increase of 1000 in pixel value. If the integration or exposure time is 1ms (maximum time of flight for particle in the laser beam) then a 1000 pixel value increase represents an irradiance of 7.9mW/m^2. Based on the comparison of the angular range of the objective from its NA value and the corresponding range determined from the diffraction image, we can estimate that our imaging unit has an angular magnification approximately of 1. This leads to the conclusion that the irradiance on the CCD sensor surface is approximately the same as that on the front surface of the objective. Therefore, each 1000 change in pixel value should correspond to an irradiance level of the side light scatter of about 8mW/m^2.

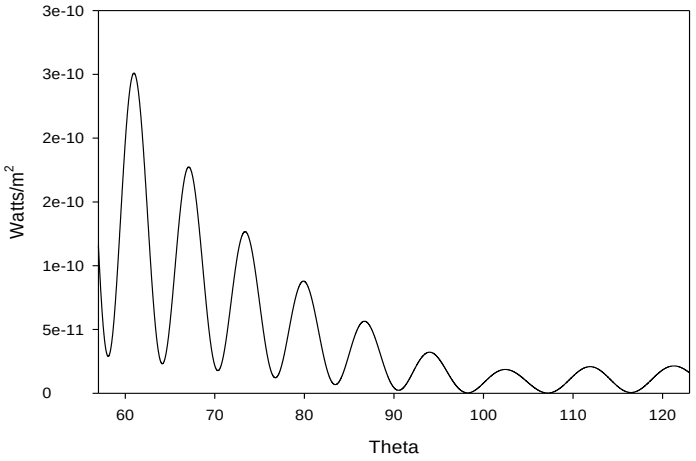

Fig. 4-10 Scattered irradiance in watts/m^2 versus angle theta from a 5μm sphere of n=1.37 in a medium of n=1.33, based on Mie scattering theory. Graph assumes plane wave, unpolarized, 633nm incident light of 1 W/m^2. Scattered irradiance is measured 13mm from sphere center.

To predict the fringe pattern and level of irradiance to the detecting camera, Mie theory based calculations of the side light scatter by a sphere are performed with results shown in Fig. 4-10. The values of diameter and indices used are those of a typical biological cell refractive index and diameter and placed in water, and for the excitation and light gathering specifications of our system. From the graph, the scattered fringe (peak) irradiance will range from $3x10^{-11}$ to $3x10^{-10}$ W/m^2 for an excitation plane wave of 1 W/m^2. With a laser beam of 3.8mW and focused to a diameter of 23μm the input excitation irradiance is $9.15x10^6$ W/m^2, if averaged over full beam

diameter. Therefore fringes output will be in a range from 0.27 to 2.7mW/m^2. As seen in the plot, any fringes in the angular range over 80^o will have peak intensities of only about 0.33mW/m^2. Including background, a pixel value of 3490 is to be expected for these fringes with the signal pixel value being 50 out of possible 65,000 pixel value full well. This is for unpolarized excitation of a 5um sphere of refractive index of n=1.37, typical for biological cells [Ding 2008]. So the peak signal is less than 1/1000 of full scale for our image sensor.

For perpendicular or parallel polarization irradiance varies by a factor of about 2, yielding corresponding pixel variation. A 10um diameter sphere is almost 4 times larger than the 5μm sphere in scattering cross sections and a 25μm is 35 times larger. Also to be noted is that exposure time used here is 1ms. If the image is not to be blurred due to motion then particle travel should be less than 1um for a 5μm particle during the 1 ms exposure time, or 1mm/s for the flow speed. This is a very slow moving stream from a flow stability point of view and particle throughput is too low to be practical for flow cytometry. For higher speeds either laser power or camera's sensitivity must increase.

Other factors may increase or decrease the peak fringe irradiance. Since the excitation laser has a small waist at the focus and the beam profile is close to Gaussian, any displacement of a particle from the focal spot will not only change the total light scattered but also distort the scattered light distribution or diffraction image pattern as illustrated in Fig. 4-11. Off center in x or z direction diminishes and distorts image pattern. Off center along y axis diminishes image irradiance and distorts from plane wave

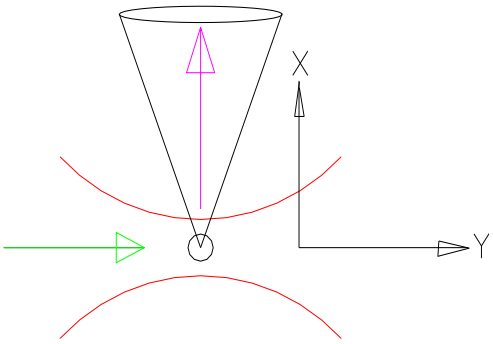

Fig. 4-11 Laser excitation from left strikes particle streaming along the z axis. Particle is in the focal waist of the laser and is also at focal point of microscope which is along x axis.

character. Losses due to the beam splitter of 50% combined with the transmission loss of 35% due to the optical elements in the imaging unit will reduce the fringe peak irradiance by another factor of six.

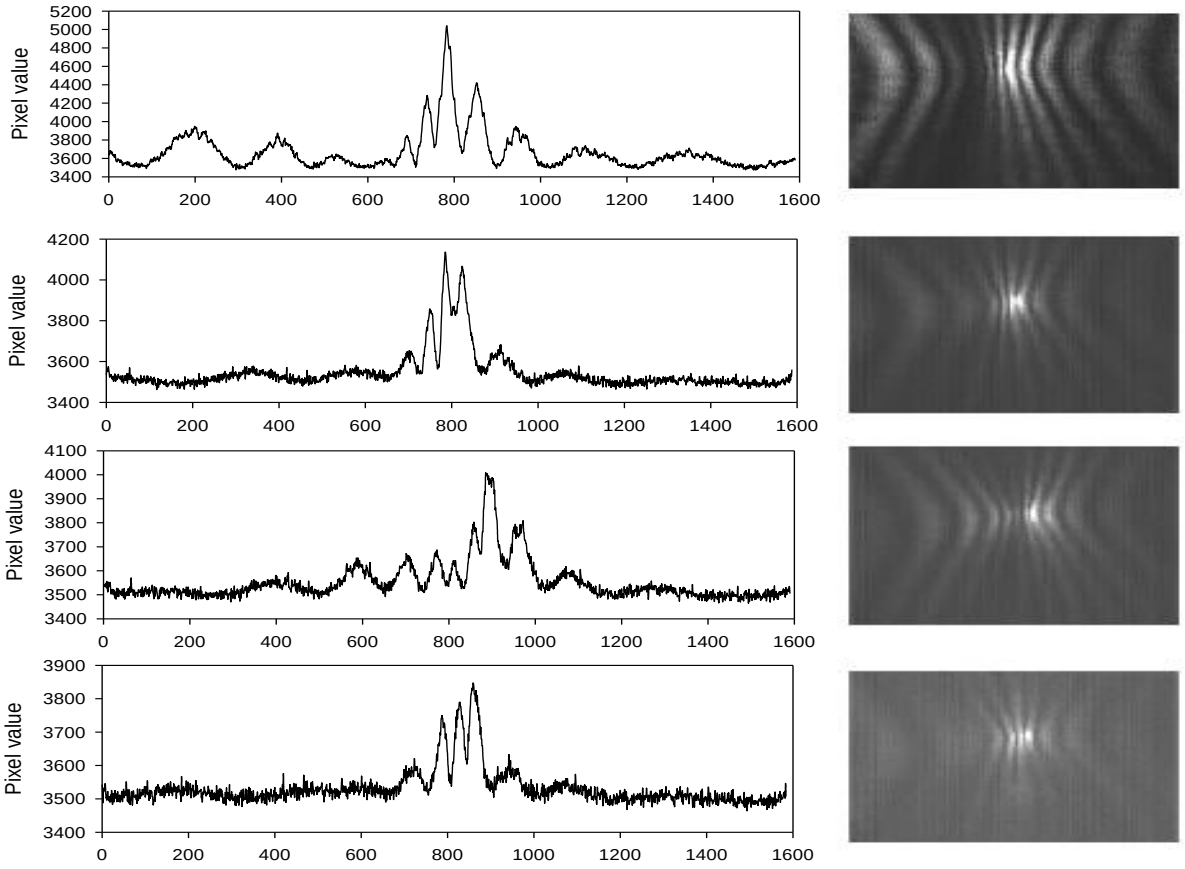

Fig. 4-12 Four images of polystyrene spheres of 10μm in diameter and their pixel value profiles. Images acquired from flowing spheres in flow chamber and with the objective translated to the defocused position of x = +200μm. The averaged pixel values (from top to bottom plots): 3590, 3511, 3516, 3509 and peak values are 6297, 4277, 4194, 3986 respectively. Background pixel value of 3400 must be subtracted to yield absolute pixel values.

Mie based calculation of the integrated scattered light

Because of the variability of peak irradiance for fringe patterns it is necessary to also calculate the total average scattered light intercepted by the objective lens. This was done using Eq. (4.5) based on the Mie theory and the results are shown in Table 4-2. Diffraction images have been

acquired from flowing spheres of 9.6μm in diameter in the core fluid of water using the CCD camera of specifications discussed above. Fig. 4-12 plots the pixel value profiles averaged over 5 rows at the center of patterns for four 9.6μm polystyrene spheres from their diffraction images shown in the right column. Fig. 4-13 is the same but for 5 and 25 um spheres. The wide variability of peak profiles among the four images is apparent, ranging from 3800 to 5000 pixel values. Absolute power levels are listed in Table 4-2 as well as predicted values based on the Mie theory from Table 2-1. Fig. 4-9 shows similar diffraction images and pixel value profiles for spheres of 5.2μm and 25μm diameters.

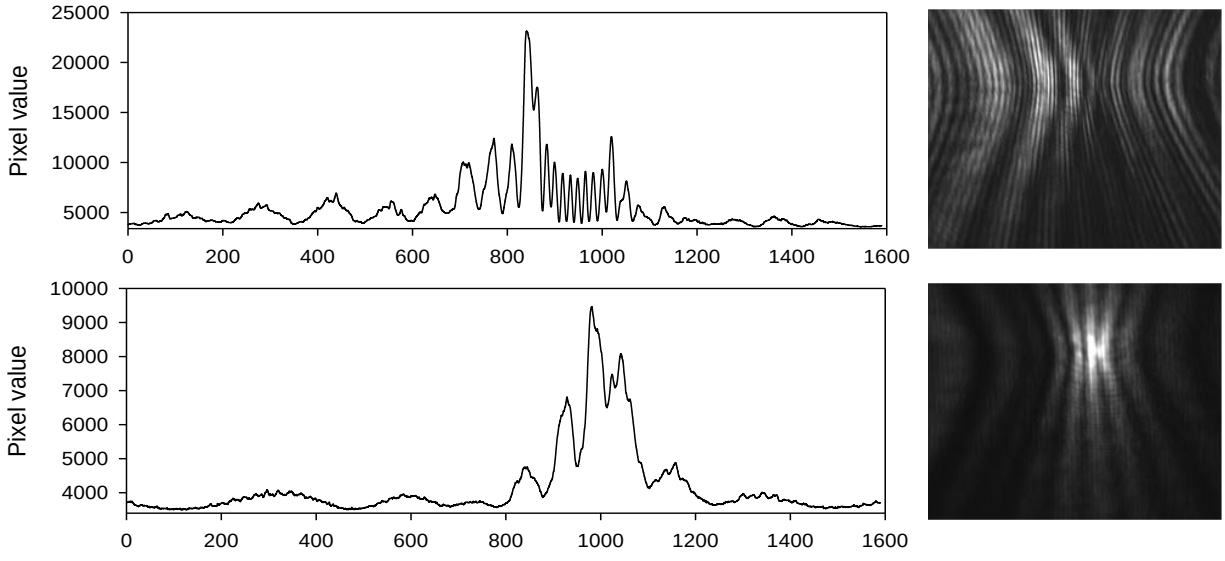

Fig. 4-13 Same as Fig. 4-12 except with spheres of 25μm (top) and 5μm (bottom) diameter.

Predicted versus measured: sources of differences

The largest source of differences comes from ignoring details of the incident beam profile which signficantly differs from the plane-wave assumed in the Mie theory. Other sources include lack of knowledge on the parameters of the optical elements in the imaging unit from

the objetive to the tube lens before the CCD camera. Another significant source in the above calculations arises because the beam diameter is comparable to particle diameter which makes it necessary to account for the beam proifle in scatteri modeling. From Fig. 4-11 it is apparent that distortions in the image due to particle positioning off of center are magnified as beam dimensions approach particle dimensions. A higher power beam with large rectangular cross section is needed, especially because very low flow speeds result in more positioning errors of the particles carried by the core stream.

Table 4-2 Calculated and measured sphere pixel values after background subtraction

Diameter (μm)		**25**	**10**	**5**
Average pixel value of image	**Predicted**	35,400	7,090	2,900
	Measured	1,500	230	1,100
Maximum pixel value	**Predicted**	179,000	41,360	13,700
	Measured	22,300	3,400	7,500
Maximum pixel value at 90^{O}	**Predicted**	27,500	4,100	2,700
	Measured	-	-	-

§4.5 Study of diffraction imaging of the spheres

Results with stationary spheres

To better anticipate imaging of light scattered by cells through an objective, we performed imaging experiments with polystyrene spheres and cells embedded in transparent gel. At issue here is how the fringe patterns in a diffraction image relate to the structure of an illuminated particle and the imaging unit itself. The sensitivity of the image patterns to variations of alignment and focusing position is critical for correct interpretation of the diffraction image for information on the particle.

Suspension of particles in a gel medium

The difficulty for imaging a stationary particle is finding a means of fixing its position relative to the incident beam without surrounding index-mismatched interfaces. Several methods were studied with varying degrees of success. One method reported by Phillips et al. [1970] involved a droplet suspended in air in a blackened chamber by an electric field controlled by an optically detected position feedback loop. This method underscores the experimental difficulties involved to fully isolate optically a particle from its surroundings under laser excitation.

Since biological cells must be in water, immobilizing particles in a clear fluid requires high viscosity. In water, polystyrene spheres of 25μm in diameter were observed to drift downward at a rate of about 10 to 20 μm/s and spheres of smaller diameter drift more slowly. Furthermore, though cells are of almost the same mass density as water, random currents in the hosting fluid cause continual motion. Various viscous fluids were tried to immobilize them. A 100% glycerol solution with a viscosity of 648 times larger than water slows the motion of cells strongly. But glycerol is not sufficiently viscous for measurements over a time of several minutes that is required to position the incident laser beam and adjust the imaging unit. We tested and finally selected KY gel, sold in drugstores, as the hosting gel for imaging spheres and cells. KY gel (ingredients: hydroxyethylcellulose, derived from cellulose fibers; chlorhexidine gluconate, glycerin; methylparaben; sodium hydroxide) has a number of advantages. It is clear with high viscosity, low cost and, more importantly, relatively compatible with cells in which can maintain viability for about 1 hour. For sphere suspensions they were mixed in the gel with a concentration designed to put one particle in an average volume of $100um^3$. Several days to a week are required to allow bubbles generated during mixing spheres into the gel to drift up and escape. Then the sphere-gel mix was injected by syringe so as to avoid new bubbles into the

bottom of a glass cuvette for imaging study. For living cells such a time period to clear bubbles was not available. Instead, we chose to inject the cell culture suspension by very a small needle into the gel in such a way as to create a thin, wispy trail of cells in the gel matrix. If the cell concentration was too high then the incident laser beam would illuminate multiple cells along its path creating multiple scattering and so reducing the contrast and accuracy of the diffraction images. Also the incident beam could be diverted by the preceding particles, making it difficult to align the objective on a targeted particle.

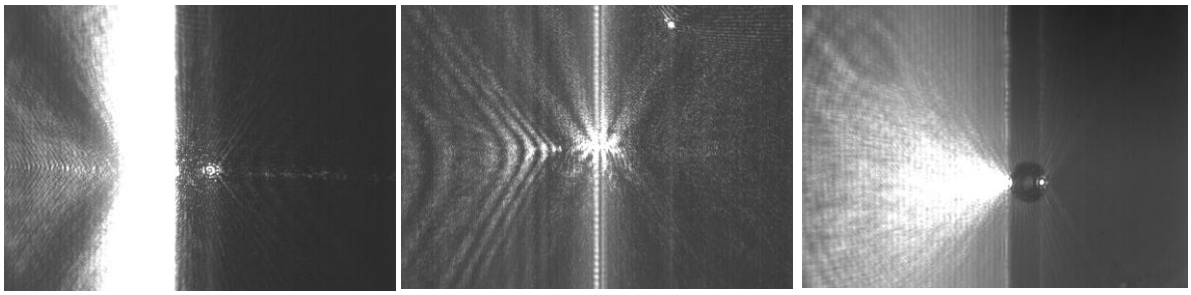

Fig. 4-14 25μm sphere at F+00 for hydroxycellulose and glycerol (KY, n=1.34); PDMS, n=1.406; and hydrolyzed silk with glycerol (clear shampoo, n=1.36). Laser is from right. Vertical lines are either the result of reflections from nearby glass walls or due to the two "dots" (Fig. 4-11), the latter most visible in far right image.

Results of imaging measurements with the particles embedded in the KY gel are shown in Fig. 4-14. The major problem was that the hydroxyethylcellulose is apparently not perfectly clear and very small particles in the gel could introduce significant background noise in the images. The gel is sufficiently viscous to make particle motion negligible for consistent measurement of multiple images. It can be seen in Fig. 4-15 that two bright "dots" of light at the spheres equator coincide with two vertical artifacts in image. The dots are not anticipated by the Mie theory and rather may be result of using objective and/or objectives position, or they may be due to the particle's morphology. In the following discussion the position of the objective is indicated by an F followed with a signed number. This refers to the position of the objective in micrometers relative to a reference position at which the objective projects a clear image of the particle under

a non-coherent illumination. For example F=+10 means the objective is moved toward the target particle by 10um from the reference position.

Although the KY gel works well, a much clearer but less practical suspension medium is the concentrated sugar solution. At non-saturating concentrations, the sugar solution does not have a sufficiently high viscosity to immobilize the spheres. Either dextrose or sucrose is heated with water at super saturated concentrations with spheres already added. The solution is poured into a cuvette while it is still hot. Measurements are made on the suspension after it cools but before crystals start to form in several hours. Although not biologically compatible, the sphere suspension in sugar solutions can be crystal clear for sphere studies.

A third suspending medium attempted was silicone oil with very high viscosity. It is clear for imaging of suspended particles. However, it is not biologically compatible and cannot mix with water. The later limitation means that spheres must be dried before mixing; otherwise the water drops trapped in oil can generate scattered light as optical noise. This process has been used with partial success and is being further improved. Others have used microscope immersion oil but with two problems [Seger 1977, Genter 1979]. Firstly a water based biological cell will either introduce water into the oil, forming interfering colloidal drops, or the cell will still drift so that only forward scatter is practically measurable (by focusing along particle drift axis and taking image as it moves through focal point). For inert particles such as polystyrene spheres, trapping them in clear

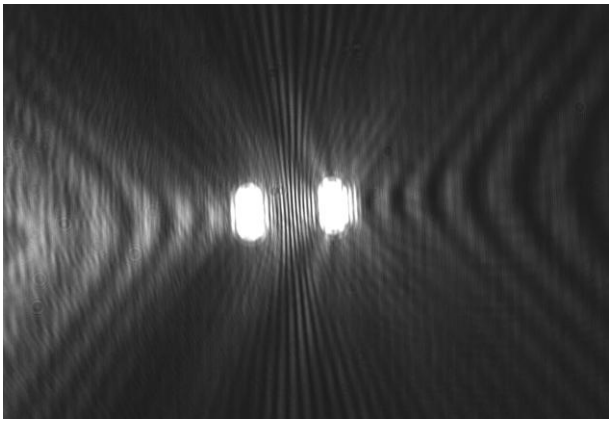

Fig. 4-15 Sphere of 25mm in diameter moving in water. Two bright areas are “dots”, blurred vertically by the motion in this case. These occur at sphere equator when the objective’s position is from F-150 to F+00.

PDMS has the advantage of permanence after the elastomer solidifies. In all the above cases optical noise was a problem. When imaging was in pure water, with walls several millimeters away, the background noise is the least. However even then diffraction images would display the two "dots" if particle was in focal plane of objective, Fig. 4-15.

Misalignment of beam with particle

The affect on the image of a particle moving off beam axis is critical since perfect alignment is not possible. Fig. 4-16 shows 25um sphere kept in focus but moved to positions off axis of a 60um diameter beam. The asymmetry of moving off axis is obvious but further studies are needed to clarify these results. We notice that even though a sphere at the edge of a beam is illuminated unevenly the image itself displays little asymmetry, the fringes being equally bright at the extremes of each image [Pernick 1978].

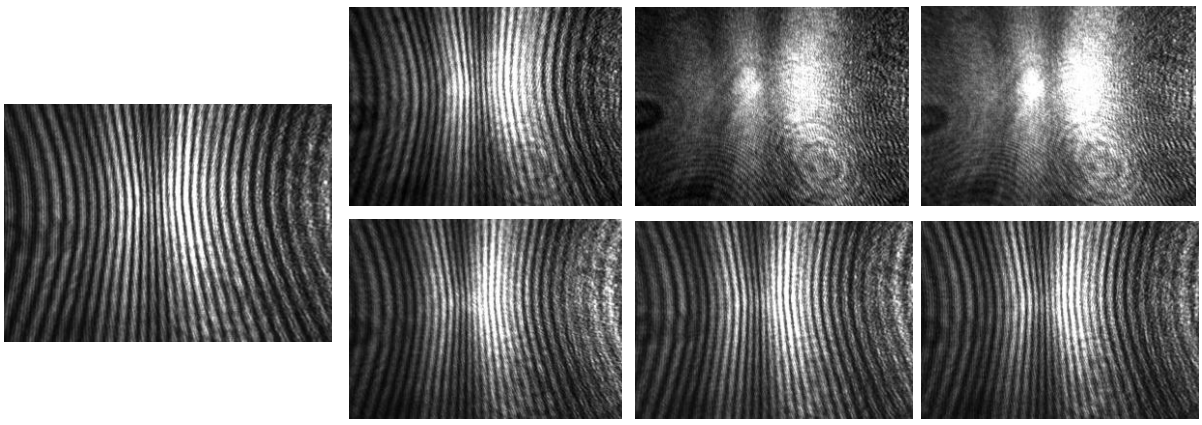

Fig. 4-16 Images of 25μm sphere kept centered and at F+200 focal position. Laser excitation beam (diameter about 60μm) is moved either toward or away from objective. Left: Δx=00; Right top row: Δx= -30, Δx= -50, Δx= -60; right bottom row: Δx=+30, Δx=+50, x=+60. Units are micrometers. Note extinction is not symmetric with respect to offset direction. Suspension medium is high concentration sugar solution. Laser beam is from right.

Images of perturbed spheres

Another issue of importance is the sensitivity of a diffraction image to small variations of particle morphology. As an example, Fig. 4-17 shows two spheres of the same 25μm diameter

with one sphere deformed. Note that parts of the fringe patterns in their diffraction images are nevertheless close to each other while the others are quite different. Fig. 4-18 displays six diffraction images acquired from identical 5μm spheres which would be indistinguishable under non-coherent light. The fringe patterns shown in these images are similar but not identical to each other. Some variations in the patterns are observable which may be attributed to the positioning fluctuation of the flowing particles relative to the incident laser beam and perhaps their diameter variation from the nominal mean value. Fig. 4-19 displays the obvious pattern change with spheres of different diameters, although particle positioning variations due to flow irregularities can change fringe spacing somewhat.

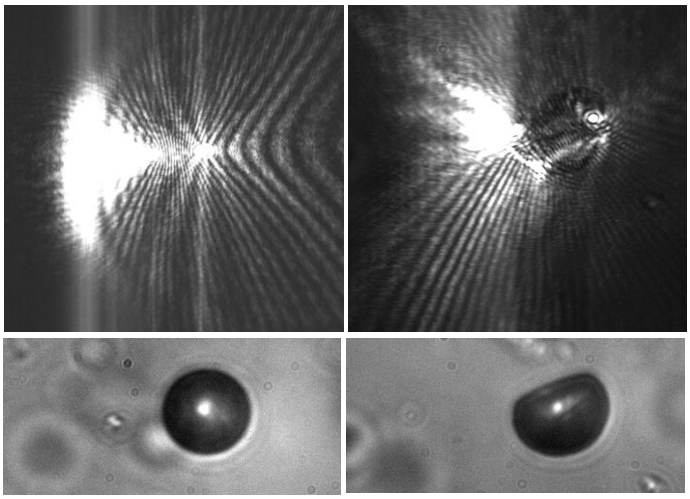

Fig. 4-17 Two spheres of same diameter suspended in gel except for a smooth dent in the one at right and their diffraction images in the upper row.

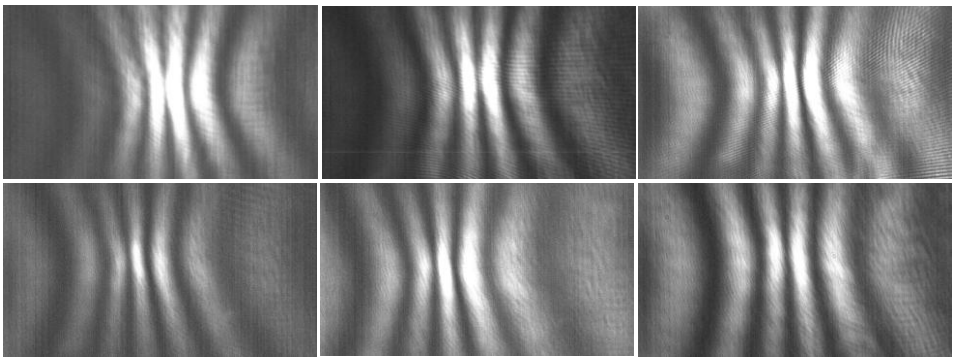

Fig. 4-18 Six images of identical 5um spheres at F+100μm focus, flowing in water at about 9mm/Sec. Variability of fringe spacing and brightness indicates limits of repeatability.

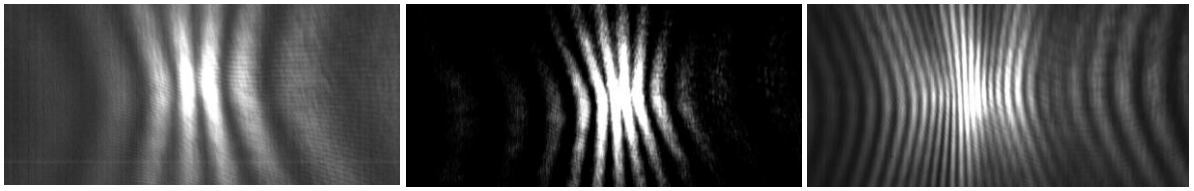

Fig. 4-19 Diffraction images acquired with flowing spheres of 5.2μm, 9.6μm, and 25μm in diameter in water with speed u=5mm/s at F+100.

Effect of focusing of the incident laser beam on diffraction imaging

Focusing the incident laser beam with a lens of long focal length has the advantage of larger focal spot which is closer to the plane-wave profile assumed in the Mie theory. Its disadvantage, however, relates to a smaller irradiance at the focal spot for excitation of scattered light. To illuminate the particle with high irradiance, a focusing lens of short focal length is needed as shown by the two diffraction images acquired with different lenses in Fig. 4-20. The fringe patterns remain the same except the image acquired with the 250mm lens appears with more uniform light distribution. An ideal excitation beam would be of a plane-wave profile or with a focal spot diameter much larger than the core fluid size that would accommodate wavering particles. At the same time the excitation beam should be narrow enough along the flow direction of the particle so that all images are acquired with the particles near the center of field-of-view to avoid multiple particles being illuminated. Usually this is accomplished with a pair of crossed cylindrical lenses [Shapiro 1985].

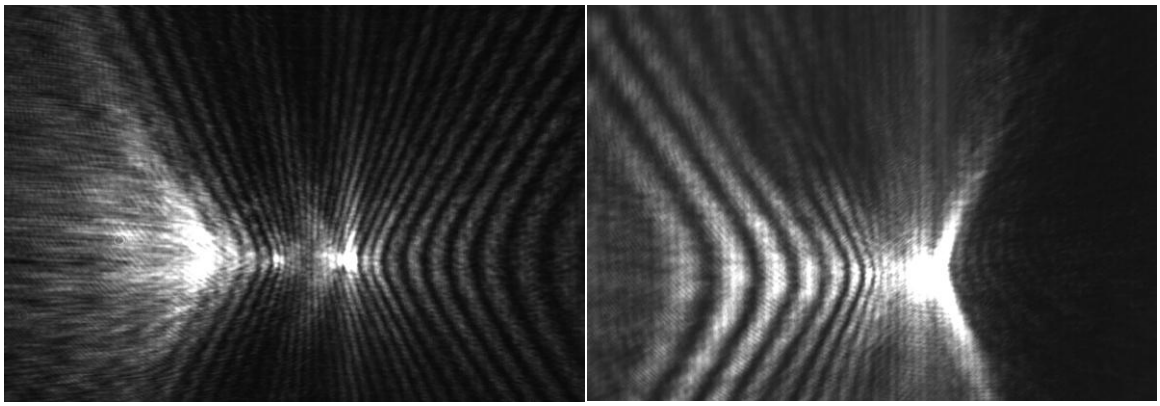

Fig. 4-20 Same 25μm spheres with objective positioned at F+50, left image was acquired with a 250mm FL lens for focusing the incident beam; right image with 50mm FL lens.

Effect of objective's position on diffraction imaging

When flowing spheres' diffraction images were acquired with the microscope objective positioned at the reference position, we found that the fringe patterns in the images do not agree with the Mie based calculations. The reference position is defined here to be the one at which a clear or high-contrast image of a particle can be obtained with the imaging unit consist of the objective and CCD camera under a non-coherent illumination. The purpose of this section is to compare the measured images with the calculated based on the Mie theory to understand the effect of objective's position relative to the particle.

Our goal is to find the condition for acquisition of diffraction images that allows one to correlate the diffraction pattern with the characteristic structure of the imaged particle only instead of those of the imaging unit. The simplest approach is to use the CCD sensor to detect light scattered by an illuminated particle directly without the objective and other optics as the cases with the photodiode array [Ludlow 1978]. This approach, however, makes alignment of the system very difficult and one typically needs a separate microscope. Our design of the imaging unit is to use the same unit for both alignment and diffraction imaging. Therefore, we have to investigate the effects of objective and tube lens which map the scattered light onto the CCD

camera, which is expected to be a projection of Mie scattering pattern for a sphere. Fig. 4-21 presents a series of diffraction images of a stationary sphere of 25 μm in diameter embedded in gel at different positions of the objective relative to the sphere. Position of the objective is given by F ±xx in microns along the x-axis relative to the reference position with positive values for moving the objective towards the particle. The reference position is marked as F+00 which is determined with non-coherent illumination. All other conditions are the same except exposure time is about ten times larger for positions >F+25μm to compensate the smaller irradiance of detected light scatters. Fig. 4-22 and Fig. 4-23 plot the fringe intensities of the sphere across its equator. The pixel positions, 1 through 1600, have been converted to the acceptance angle the objective which is 66^{o}.

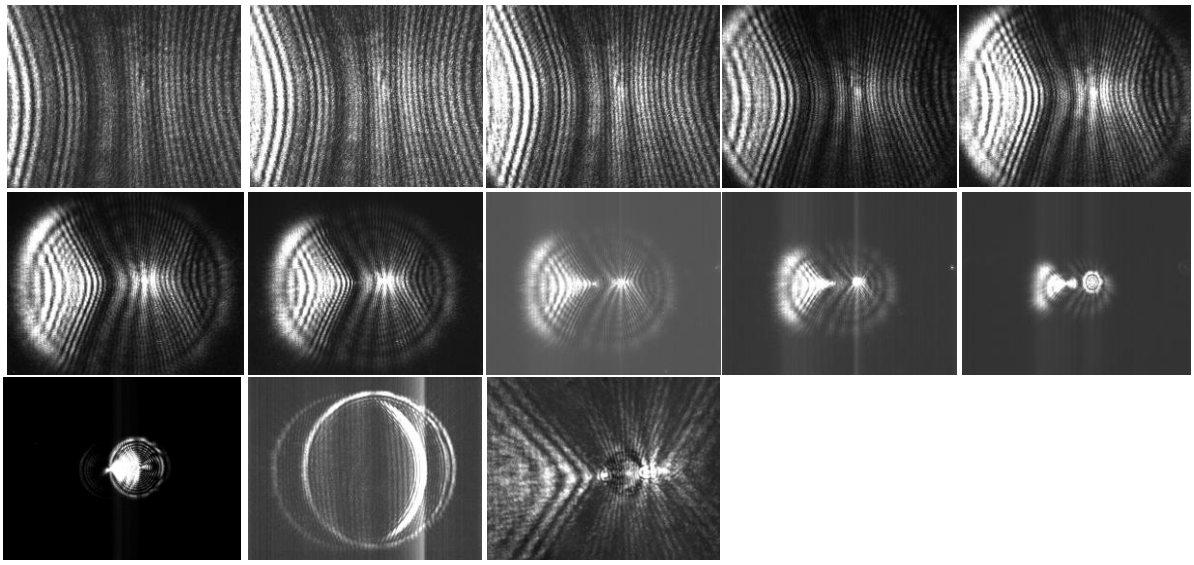

Fig. 4-21 Series of diffraction images acquired at different objective's position: (starting from upper left to lower right): F+200, F+175, F+150, F+100, F+75, F+50, F+25, F+000, F -25, F-50, F-100, F-200. The diameter of the sphere embedded in gel is 25μm with refractive index for sphere n_{sp}=1.59 and for gel of n_g=1.34. The wavelength of incident laser beam is 532nm and incident from right. All images were acquired with laser illumination except the lower right one with both laser and non-coherent illumination.

Distortions of the scattered light caused by the optics in the imaging unit in comparison to the predicted Mie projection can be seen by comparing the top plot (Mie prediction) of Fig. 4-22

with the remaining irradiance profiles of Fig. 4-22 and 4-23. As can be seen the fringe intensities are modulated with each envelope containing five to ten fringes. Therefore fringe patterns along equator may be characterized by their total number in the image, the total number contained within the angular diameter of the sphere (222 pixels or $\Delta\theta=9^o$), and the number of fringe modulation envelopes in forward and back scatter (for scattering angle of $60^o< \theta < 90^o$ and for $120^o> \theta > 90^o$ respectively). These results are listed in Table 4-3. The calculated values use a FOV of 215μm in horizontal size for images containing all fringes of 66^o acceptance angle, meaning that Mie scattering angles run from 57^o to 123^o. This does not account for light refraction at the interface between air and chamber of $1cm^2$ size, which reduces FOV.

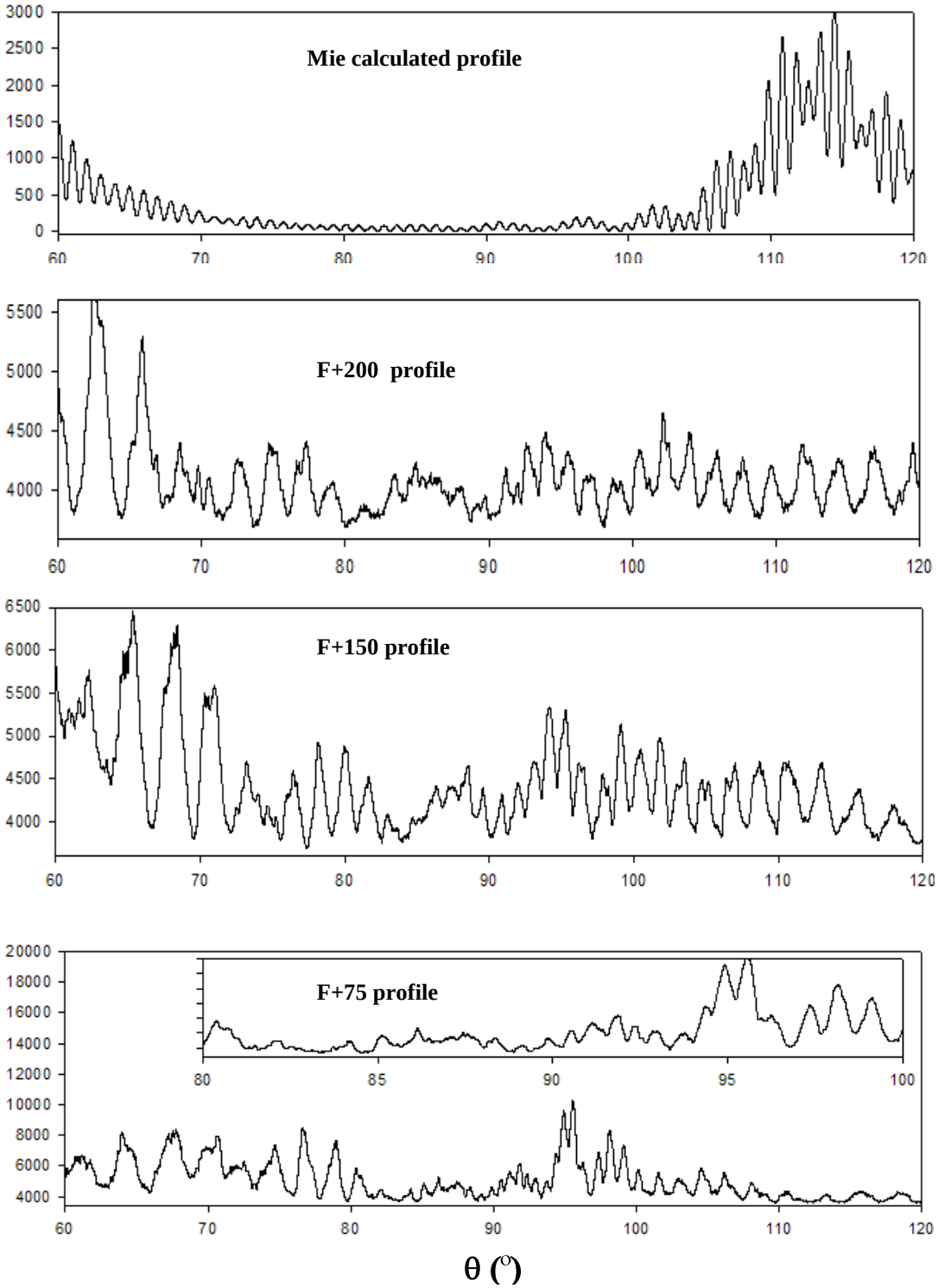

Fig. 4-22 Profiles from calculated and measured diffraction images of Fig. 4-21. Top panel is Mie theory based calculation for a 25μm polystyrene sphere of refractive index n_p=1.59 in a gel hosting medium of n_g =1.34 using 532nm unpolarized excitation. Lower panels are from diffraction images of polystyrene in gel measured with objective positioned at F+200; F+150; and F+75.

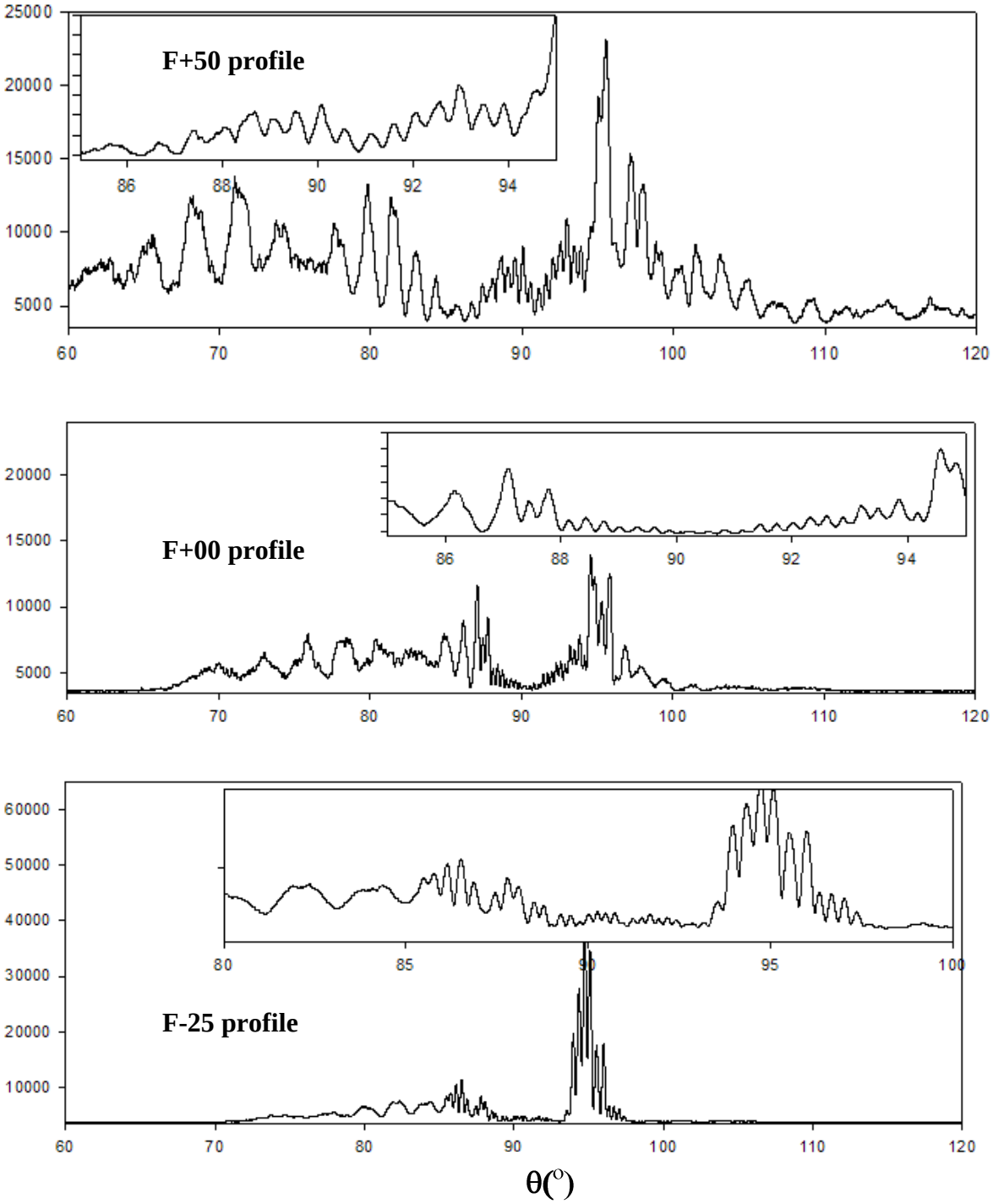

Fig. 4-23 Continuation of pixel profiles of measured diffraction images from Fig. 4-21. All are from 25μm polystyrene sphere at positions: F+50; F+00; F -25.

Table 4-3 Characterization of fringe patterns for 25μm spheres

	Number of fringes ($60^o<\theta<120^o$)	**Number of fringes ($85.5^o<\theta<94.5^o$)**	**Number of modulations ($120^o>\theta>90^o$)**	**Number of modulations ($60^o<\theta<90^o$)**
F+00 Mie results	64	11	7	1
F+200μm	31	7	2	2
F+150μm	35	7	3	3
F+75μm	40	8	4	2
F+50μm	41	16	2	3
F+00μm	41	25	1	1
F -25μm	41	30	1	1

Diffraction images acquired with the objective at positions from F+100 to F+300 look very similar to the Mie calculated images. However, our goal is to find optical markers in terms of the characteristic fringe patterns of the biological cells and we are thus only concerned with the correlation of the pattern with cellular structures and not their physical basis. The criterion for success of our study is therefore on how much information on the structural difference among different particles is carried by the image data. For images acquired at positions from F+100 to F+300 the scattered light irradiance or pixel values around the patterns decreases as the objective moves toward the particle and so do the number of fringes and the number of modulation envelopes. Fig. 4-24 summarizes these effects by plotting peak and average irradiance of the images. The peak irradiance is highest in the image acquired at about F-75 and the average irradiance diminishes as the objective moves closer to the sphere. Since the background pixel values is about 3340, so the change of pixel values from 3510 in the image at F-300 to 3430 in the image at F+200 represents a 50% change. All of this information suggests that the fringe pattern contrasts becomes lower for positions overly close to the target.

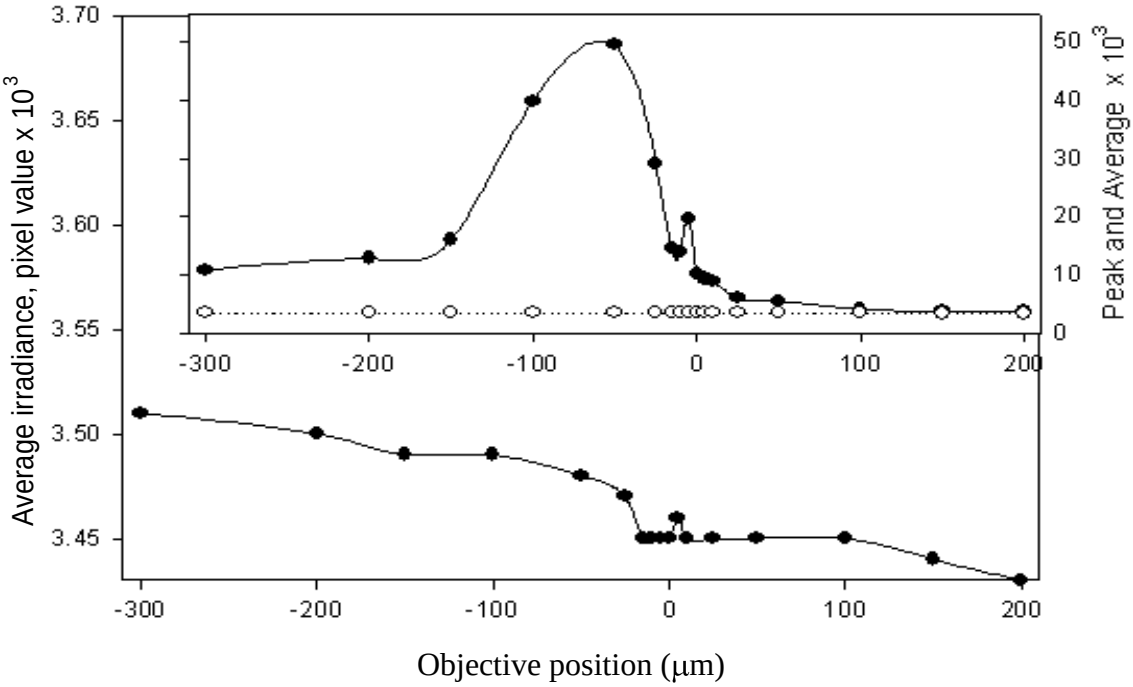

Fig. 4-24 Average (bottom) and peak and average (top) pixel values for a 25μm sphere embedded in PDMS with 532nm laser with a constant source and exposure time, as function of objective position in μm.

On the other hand, for images acquired with the objective at positions between + and – 50um from the reference position there are two bright "dots" on the equator or center pixel rows associated with the entrance and exit points of laser beam on the illuminated sphere. These patterns clearly are not predicted by the Mie theory but rather due to certain surface effects and possibly the beam profile, and likely they carry no morphological information. Our experimental results shown in Fig. 4-24 suggest the latter, indicating that focusing at these distances would reduce information available by saturating the camera CCD or obscuring dimmer fringes.

Additionally, distortions of the fringes in regions off of its equator are apparent in Fig. 4-25. Note here that the fringe constricting at the sphere equator is much greater in the image made with microscope than in Mie projection. The constricting also puts fringe density higher near center as focus approaches zero. Since the excitation is a Gaussian distribution, the irradiance

decreases from center and thus the images will not match the calculated ones based on the Mie theory. There may even be fringes at the edges of FOV that are too dim to be seen. Further experiments need to be done to resolve these differences between the measured images and Mie calculations.

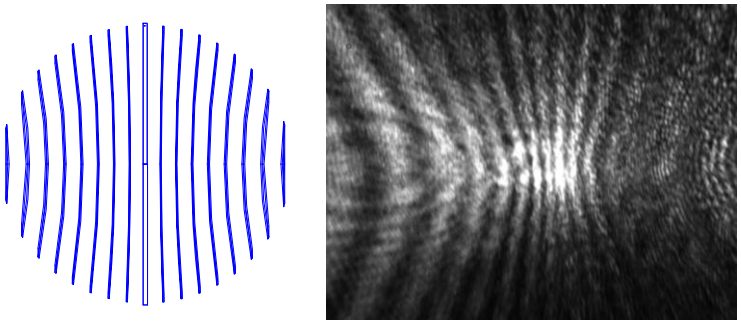

Fig. 4-25 Projection of Mie calculated fringe outlines onto a plane for a 10 μm sphere, left, and an image of a 9.6 μm sphere in suspending gel at F+75μm.

The static images can be used to examine many of the problems that might occur with moving images. Inaccurate positioning of the particle within interrogation point of laser and microscope induces significant changes in images generated. Positioning error can be along any axis, x, y, or z. The results of error are seen in average image irradiance, skewing of irradiance distribution, distortion of image features, and introduction of unexplainable image features. Most importantly it is not clear what the ideal objective focal distance should be because optical path introduces changes in image not easily interpreted such as the two bright dots that occur near where beam enters and leaves sphere. Apparently a compromise needs to be made between light energy received and interpretability of image pattern when choosing focal distance to be used. The choice of F+200 was made based upon similarity to Mie theory prediction but that choice carries with it the problem of irradiance reduction by at least a factor of ten over F+00 position. From F+25 down to larger negative focal displacements it is difficult to know if image is due to particle or mixture of particle and optics. The additional issue of particle tumbling and angular positional accuracy about x, y, z axes is discussed in Chapter 5.

Chapter 5 Diffraction imaging of flowing spheres and cells

§5.1 Fluid dynamics of particles in flow chamber

Submerged jet silhouette

Fig. 5-1(a) shows the stream profiles plotted for three flow rates according to Eq. (2.29) used to model our submerged jet flow chamber. The profiles are of the interface between sheath fluid and chamber fluid as jet moves downstream (up in plot) and for different flow rate ratios [Richards 1994, Schneider 1984, Andrade 1937]. Studies of similar fluidic configurations have been reported. The most recent one was a numerical and experimental study of submerged jet into another immiscible coaxial flow stream with both fluids confined to an outer cylinder [Vempatti 2007]. Note that the fluids cannot mix and that the jet was a single fluid stream. In our case the jet itself consists of two coaxial fluids of differing speeds and both are jetted into a third chamber fluid with all three fluids able to entrain with each other. Therefore the complexity is greater and to my knowledge no detailed calculations have been done for a three fluid submerged jet configuration. The following experiments were only designed to guide our design of a flow chamber for acquiring diffraction images.

Two images at different flow rates are presented in Figs. 5-1(b) and 5-1(c) for an 80 micron diameter jet. The imaging is possible because a 2% glycerol solution is used as an approximation of usual static fluid in chamber (water). Agreement is good between jet silhouettes calculated as shown in Fig. 5-1(a) and measured results shown in Fig. 5-1(b,c). These results provide us with

some confidence Eq. (2.29) can be used to optimize the best flow rates and their ratio for hydrodynamic focusing of particles and determination of flow speed.

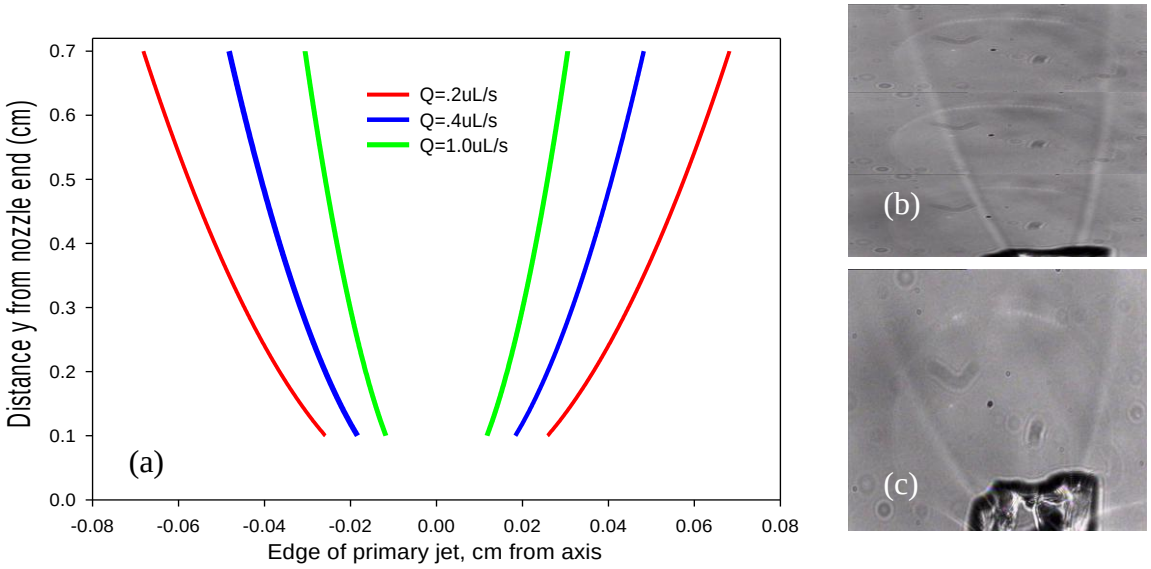

Fig. 5-1 (a) The calculated profiles from Eq. (2-29) of the interface between the sheath and chamber fluid with sheath (with core) jetted into chamber at different flow rates Q; (b) a non-diffraction image of the sheath of 2% glycerol and a core fluid of pure water injected with a nozzle of 80um in diameter at Q =1.0 μL/s, the vertical dimension of image is about 1.2 mm; (c) a similar image of the same nozzle at a smaller flow rate of Q = 0.2 μL/s.

Focusing nozzles

The goal of hydrodynamic focusing with a submerged coaxial jet is to stably reduce the diameter of the core fluid to about 25 μm from its value that is about ten times greater at the nozzle of fluid injection. Various combinations of sheath and core tubing diameters and flow rates can be chosen to optimize flow characteristics. The two plots shown in Figs. 5-2 and 5-3 are experimental results performed to help select operating parameters using measurement techniques described in Chapter 3. Experimental results presented in Fig. 5-2 indicate, as expected, that a smaller diameter nozzle core tube allows tight hydrodynamic focusing and in a shorter distance at all sheath and core flow speed ratios. The data represented by the symbols are fitted with an exponential decay curve as $y = A + B*(e^{-Cx})$ in which y is the core diameter and x

is the ratio of flow speeds. The fitting parameters were found of the following values: A= 44, 14, 8, 7(μm); B= 92, 90, 104, 124(μm); C= 0.31, 0.37, 0.56, 1.8(μm) if the core tube inside diameters are of these values, respectively: 110μm, 180μm, 340μm, and 510μm. With the exponential fitting curves, one can estimate the core fluid diameter for any value of the flow speed ratio for nozzle design. For a constant core tube diameter, however, a sheath tube of larger diameter allows better hydrodynamic focusing than that with a sheath tube of smaller diameter because there is less total momentum to transfer. These results agree qualitatively with published studies but more detailed studies would be useful to improve further [Rankin 1983, Van Dilla 1985, Vempatti 2007]. The conclusion based on these experiments is that the smallest possible core tube and a sheath tube of quite large diameter with slow moving sheath fluid is the best combination for hydrodynamic focusing of the particles. Keep in mind that a core tube of small diameter often causes particle clogs so the final choice depends upon how reliable of a core fluid stream is desired.

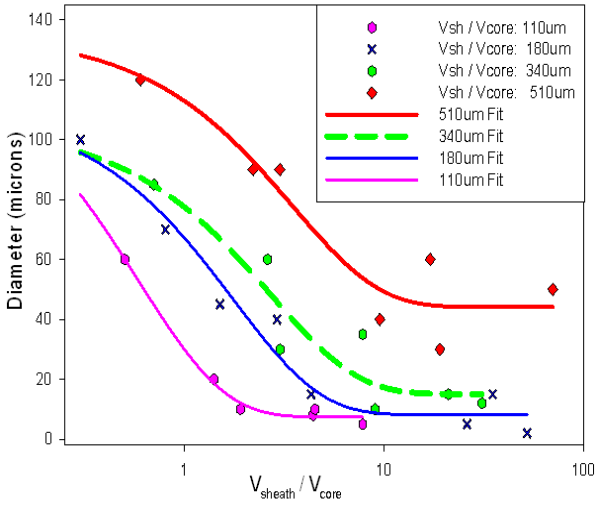

Fig. 5-2 Core stream diameter versus sheath/core flow speed ratio for several core tube diameters. Sheath tube inner diameter is kept constant at 6.76 mm and average sheath flow speeds range from 0.28 mm/s to 8.8 mm/s. Core flow speed inside injector tube average velocities range from 4 mm/s to 576 mm/s. See text for curve fitting.

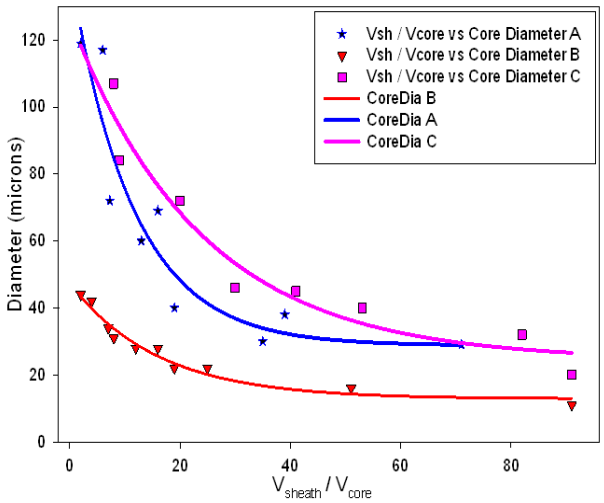

Fig. 5-3 Core stream diameter versus sheath-core flow speed ratio for different nozzle designs. Nozzle A: 3670μmx340 μm; Nozzle B: 2420μmx260 μm; nozzle C: 1250μmx260 μm. Diameters are inside dimensions. The lines are exponential decay fit.

§5.2 Imaging of Flowing Particles

Particle density in stream

For the core flow stream the inside chamber particle concentration must be kept low enough to prevent multiple scattering inside the focal point of the incident laser beam. In fact the nearest particle needs to be considerably further than the diameter of laser beam. This is because scattered light from a target particle is returned back to it by scatter from nearby particles in the flow stream. The nearby particle may be well outside of imaging FOV and still generate enough interference to degrade the image of target particle. To eliminate interference Eq. (4.2) is used to calculate the acceptable particle concentration in the core fluid. However, the required detection span Δz between neighboring particles (or surface) will be the minimum distance over which the scattered electromagnetic wave from a nearby particle will interfere with that of the targeted particle.

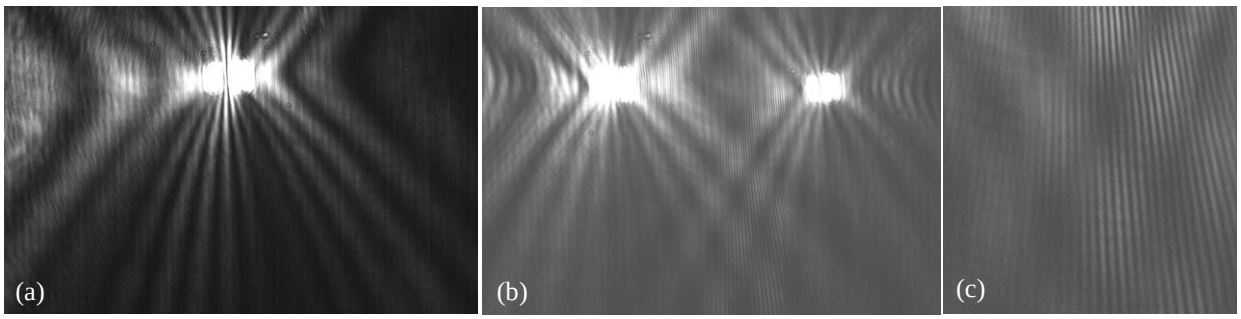

Fig. 5-4 Different interference fringes observed in diffraction images of polystyrene spheres of 9.6μm in diameter: (a) a single flowing at high speed which causes a blurring bright spot at center; (b) two spheres in the same FOV; (c) a close-up view of the lower center region in the (b) image.

Fig. 5-4 illustrates the effect of scattering by multiple particles. For imaging parameters used here the detection span has been found to be in the hundreds of microns which is larger than that for conventional non-imaging flow cytometry where fluorescence based signals are not sensitive

to the presence of another particle within the field-of-view (FOV) of the collection optics. Fig. 5-4(c) presents an example of fine structure of scattered light interference due to the presence of the two particles seen in Fig. 5-4(b). Notice also that the overall contrast has been reduced in comparison to the image shown in Fig. 5-4(a) which has no nearby particle.

Exposure time and flow speed

As exposure time increases for imaging moving particles the resultant images degrade due to motional blurring and it is useful to test the amount of blurring that can be tolerated for later analysis. For a polystyrene sphere the fringes patterns in its diffraction image are aligned along motion direction so that blurring effect is not readily observable. Biological cells do not have such high symmetry so their fringe patterns in the diffraction images are mostly two-dimensional array of light "islands" of various shapes and texture [Neukahammer 2003]. Thus the blurring effect is more significant to the diffraction image analysis of cells. However a cell's diffraction image may be blur-free and still have a diffuse appearance. In these cases it is difficult to distinguish the effects of motion blurring from the speckles in a diffraction image due to field interference. Figs. 5-5 and 5-6 are two tests of blurring effect due to motion of cells with varying camera exposure times. For the NALM-6 cells of diameters around 15μm there is no clear evidence of motional blurring in Fig. 5-5, even though motion during exposure ranges from 0.25 to 4.5μm. By comparison the

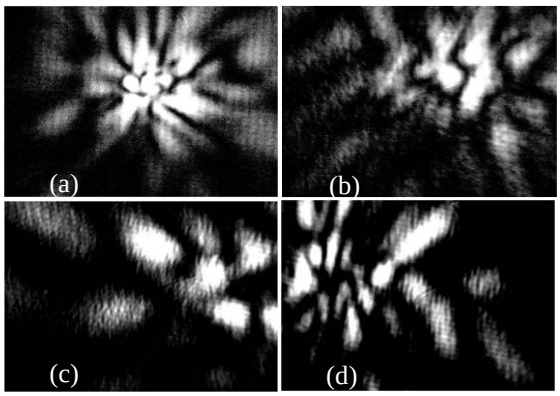

Fig 5-5 Diffraction images of NALM-6 cells acquired with different exposure times at a flow speed of v=3mm/s: (a) 80μs, (b) 200 μs, (c) 500 μs, (d)1500 μs. Incident beam wavelength is 532nm and FOV is 65μm x109μm.

diffraction images of U-937 shown in Fig. 5-6 were acquired with the objective set at the F+00 positions so their fringe patterns exhibit higher contrasts. It is clear from these images that blurring begins to affect fringe patterns when exposure time is increased somewhere beyond one millisecond, corresponding to a moving distance of 1.2μm or about 10% of cell size. We can conclude that effect of motion blurring can be kept reasonably low on diffraction images for one millisecond exposure times with flow speeds between 1 and 5 mm/s.

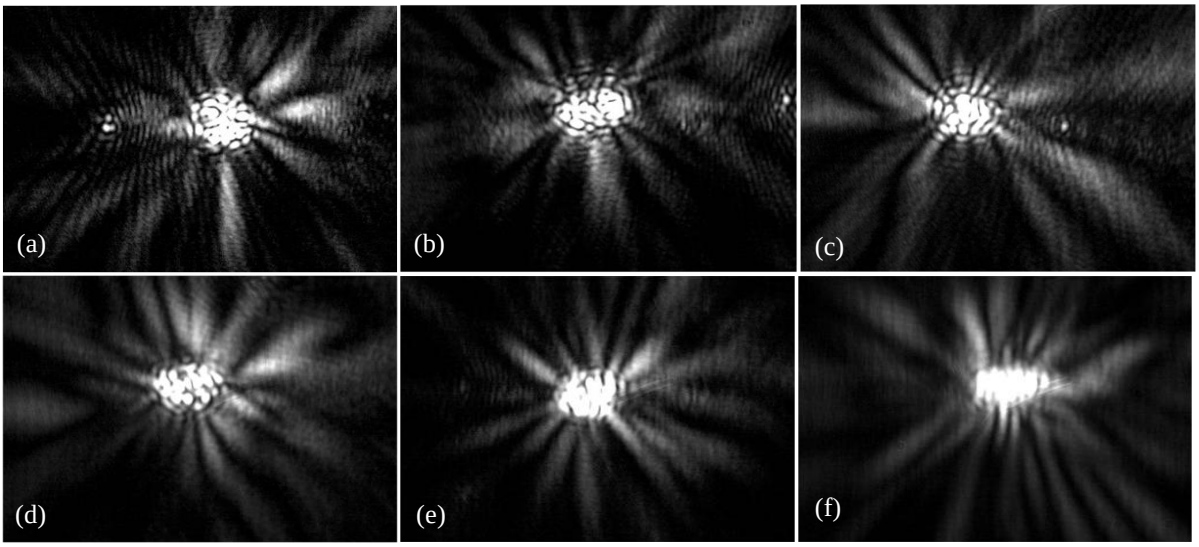

Fig. 5-6 Diffraction images of U-937 cells acquired with different exposure times at flow at speed of v=1.25mm/s : (a) 200μs, (b) 400μs, (c) 800μs, (d) 1500μs, (e) 3000μs, (f) 6000μs. Incident beam wavelength is 532nm and the position of objective is at F+00.

Effects of concentration and position of the objective on cell imaging

We embedded cells in KY gel to study the effects of cell concentration and positioning of the microscope objective on diffraction imaging. If the concentration of cells in the gel is too low then it becomes very hard to position them into the FOV, remembering that sample must be searched in three dimensions by translating the gel sample. If concentration is too high then scatter of the excitation beam by cells in the pathway of the beam and secondary scatter generates optical noise such as the vertical band seen in Fig. 5-7, which was acquired with the

objective positioned at F+00 since pixel values are greatest at this position. As with the sphere images it is not known exactly which objective position x is the best choice to acquire diffraction images and extract information on a cell's morphology. For stationary particles the scattered irradiance plays no role in image quality since long exposure time can be used. For flowing cells the positions of the objective past F+50 provide diffraction images of significantly smaller pixel values. Figs. 5-8 and 5-9 show effect of microscope objective position on cell images of MCF-7 cells and B16F10 cells, which are the cell equivalent diffraction images of spheres shown in Fig. 4-21. These cells were viable and mixed into a KY gel filled cuvette while trying to limit air bubbles which cause unacceptable scattering. As is readily apparent, different objective positions change the fringe patterns in the diffraction images. Typically the images acquired at negative positions (objective pulled away from the imaged cell) have higher contrast, higher total fluence, and higher fill of the FOV than those acquired at positive positions. The total light fluence corresponding to the images acquired at positive positions is less than 1/10 of that at F+00. At positions near the focal position F+00 fluence and contrast are high but most energy is focused at the center of FOV making feature analysis difficult. It is a possibility that images taken far from the F+00 focal position such as at F-300 could be the most useful for discriminating cell morphology even though they are far from the Mie prediction. Additional study is needed to determine why images at F+00 do not agree with the Mie prediction. Most likely the cause is non-planarity of excitation light wavefront and microscope optics of high NA.

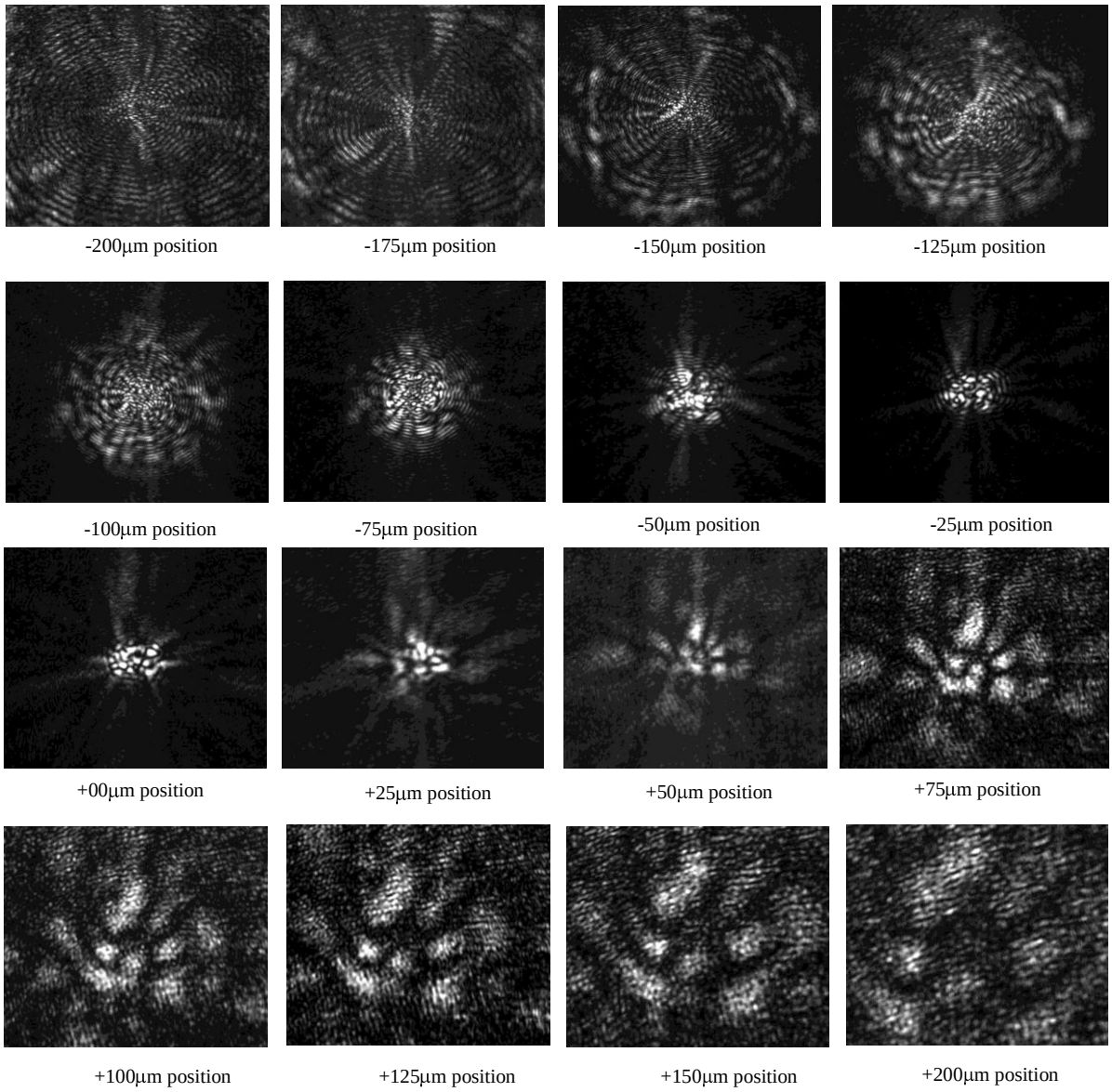

Fig. 5-8 Diffraction images of MCF-7 cells embedded in gel at different objective positions. Positions are labeled under each image as the distance from the focusing position under non-coherent illuminations. The laser beam is incident from right side of particles and has a wavelength of 633nm.

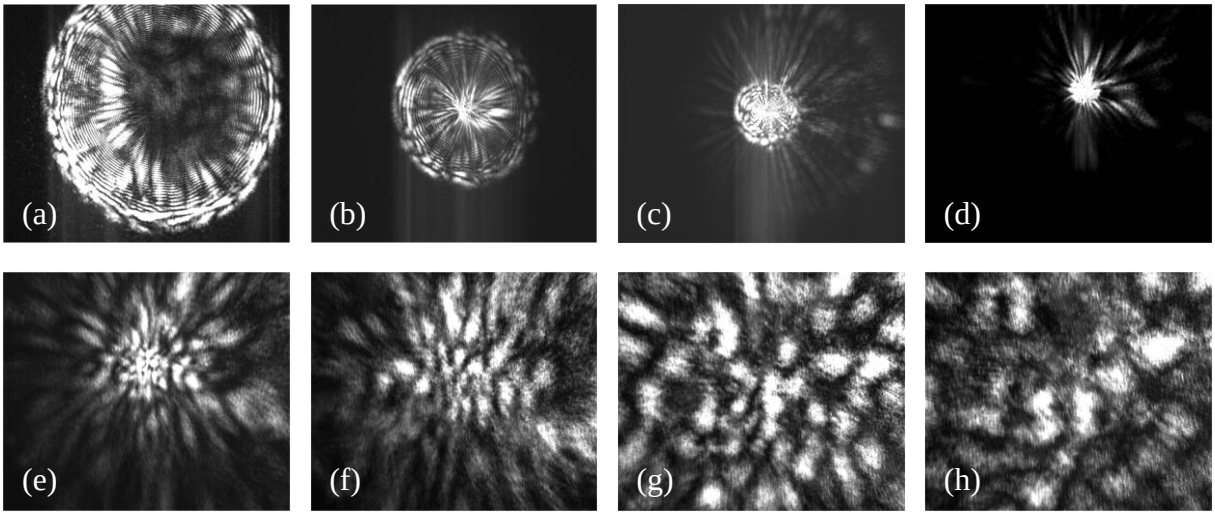

Fig. 5-9 Diffraction images of B16F10 cells in gel with 532nm wavelength laser excitation at different objective positions: (a) F-300, (b) F-200, (c) F-100, (d) F 00. (e) F+100, (f) F+200, (g) F+300, (h) F+400.

§5.3 Diffraction Imaging of Cells: Results and Variability

The Figs. 5-10 to 5-16 on the following pages present the diffraction images acquired from individual flowing cells of six cell lines of Jurkat derived from human T cells, Tramp-C1 vector derived from human epithelial prostate cells, NALM-6 derived from human B cells, U-937 derived from human monocytes, B16F10 derived from mouse melanoma cells, and MCF-7 derived from human breast cells respectively. All images are taken with the core fluids made of PBS solution with some growth medium present, at F+100 focal position, at speeds ranging from 2 to 8 mm/s, with exposure time of 1 millisecond, and a laser excitation beam of 47 mW in power and 532nm in wavelength. The incident beam is focused to a focal spot of 25μm in diameter at the center of FOV. Each figure of 10 diffraction images is taken from individual cells of the same cell line and the two columns are from two different cell samples. Thus the variability of the diffraction images within the same sample run and the same cell line can be observed. The objective position of F+100 was chosen because it reliably allows adequate image brightness even though it is not at the ideal position (F+200) we found in the imaging of spheres

for matching with Mie theory based calculations. The images were selected from collections of images based on their centeredness within the FOV, their isolation from nearby cells, and on having average pixel values close to the collection average. The least controlled instrument variable is cell positioning along the axis (x) of the microscope objective. This later of course has a large effect since it alters the targets relative positioning both to the excitation beam and the objective.

A large number of images are presented here because their variability is not quantifiable except by visual observation, i.e. an algorithm for analysis of diffraction images is not yet available to extract image features for classification of cells, which will be pursued in the near future. The goal of this dissertation research is to develop a flow cytometer that can allow rapid acquisition of diffraction image data from individual cells with high contrast and collect preliminary data from biological cells to allow future algorithm development. Here we would like to present some qualitative discussion on what type of patterns in these diffraction images consistently represent themselves and can be related to specific cell morphological characteristics. Image noise masking these patterns is of several types. One is measurement noise such as the variations caused by a particle being incorrectly centered in the FOV of the microscope objective. The other is particle noise such as varying cell size or shape or surface that is a normal variation of cells but not the one being investigated. Also if the imaging process is poorly understood then differences between instrument designs can introduce noise. This latter noise source for example has resulted in significant differences between our diffraction images and those of Neukhamer [2003]. The images following were all done with our flow cytometer using the same chamber, flow nozzles, fluid medium, optics, and camera. Therefore image variations within a single cell line and a single sample run must be due primarily to cell

positioning or cell morphology. Positioning refers to the x, y, z position of the flowing cell at interrogation point of the incident beam, as shown in Fig. 4-11, and to the three angular positions about these axes (tumbling) although linear and angular position of a cell will usually not have a precise meaning since their geometry is so irregular. What is meant by cell morphology are all the parameters to characterize a cell's structure including size, shape, surface texture, and the sought after internal structural characteristics.

A cursory look at the images reveals some obvious inter cell line variability such as the fine structure of the B16F10 cells, extra long radial light islands of Tramp-C1, irregularity of NALM-6, and diffuseness of Jurkat. Possibly the fine structure of the B16F10 diffraction patterns indicates a consistently larger cell volume relative to other cell lines. But the other diffraction pattern differences between cell lines suggest that their origin may be the cell morphology. A similar analysis of diffraction images has been reported applying the characterizations of length, concentricity, and radial orientation of light islands [Aptowicz et al. 2005]. Using just visual observation to evaluate a large collection of diffraction patterns for each cell line indicates that the pattern variability is too large and the characterization too subtle to reliably discriminate between different cells and different cell lines. The next section provides some discussion on human and computer pattern recognition.

Concerning the images we note that cleaning chamber between different runs of the cell samples is not always perfect. For example the bottom right image from the Jurkat image set may be a stray cell in flow chamber from the Tramp-C1 sample. Likewise a 25μm polystyrene sphere, Fig 5-16, was observed in the run of an MCF-7 cell sample but conveniently serves as a calibration for that sample. This indicates the need for design and use of disposable cell sample holders.

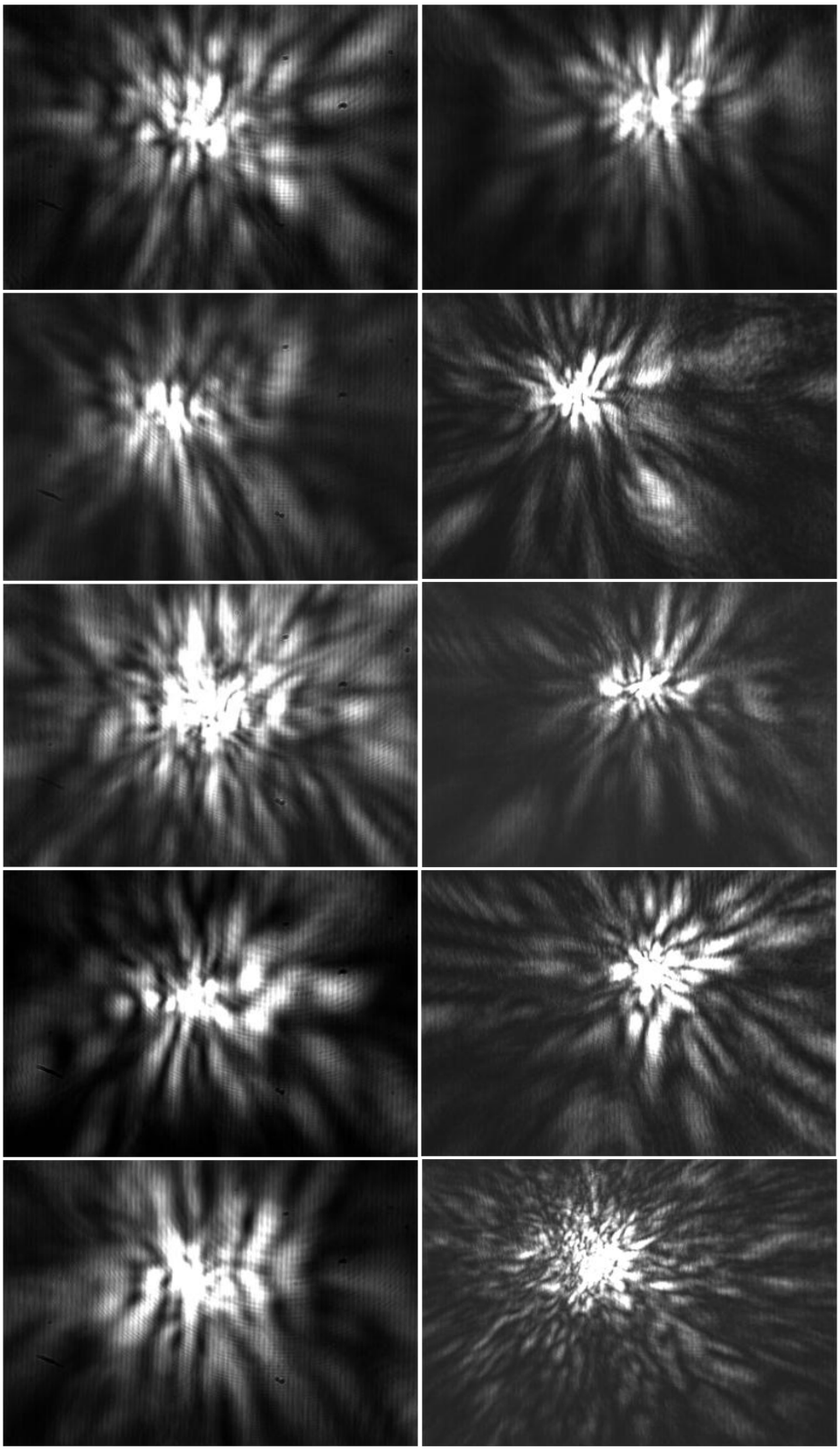

Fig. 5-10 Diffraction images of individual Jurkat cells acquired with the wavelength of incident laser beam at 532nm.

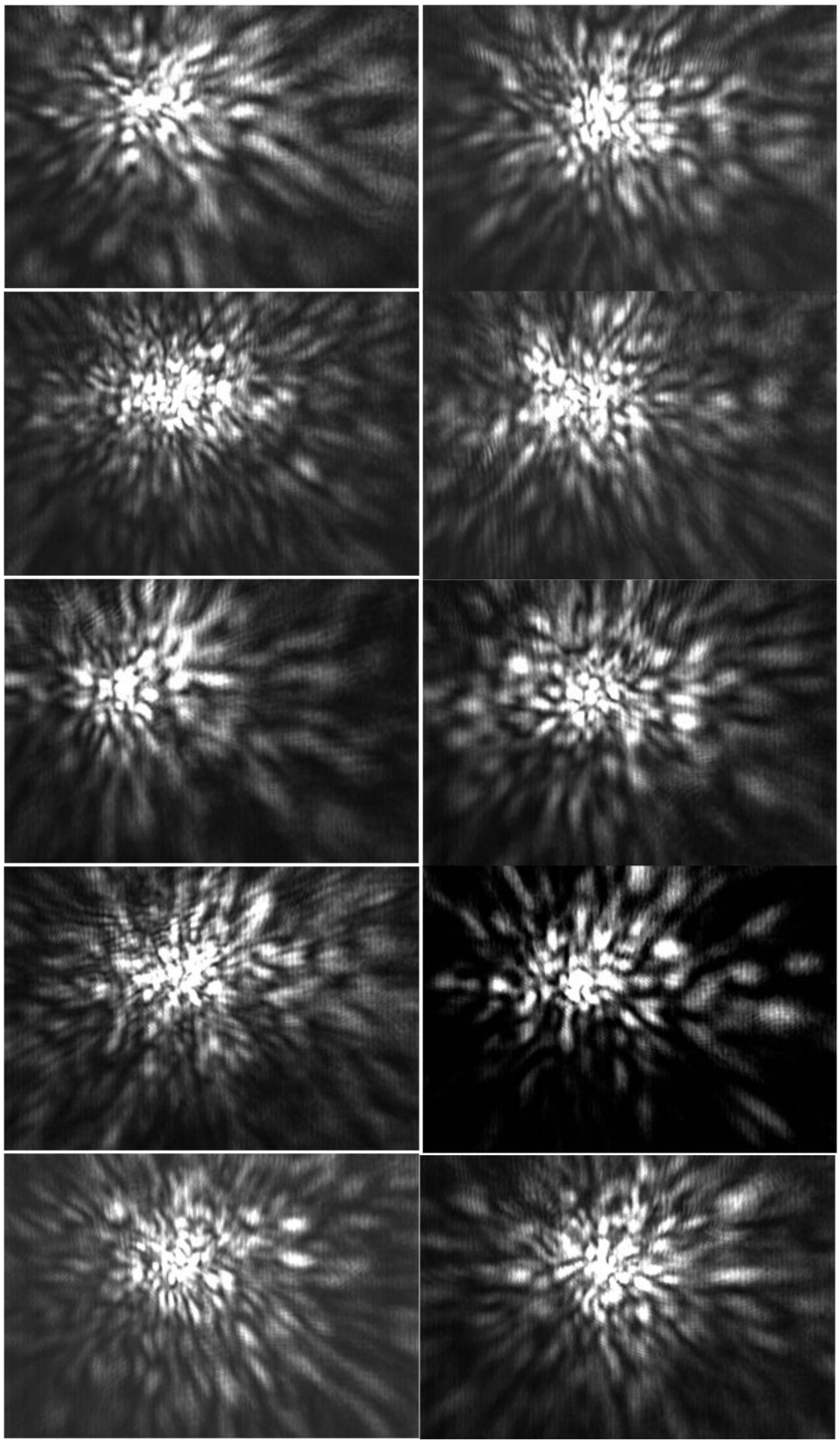

Fig. 5-11 Diffraction images of individual Tramp-C1 cells acquired with the wavelength of incident laser beam at 532nm.

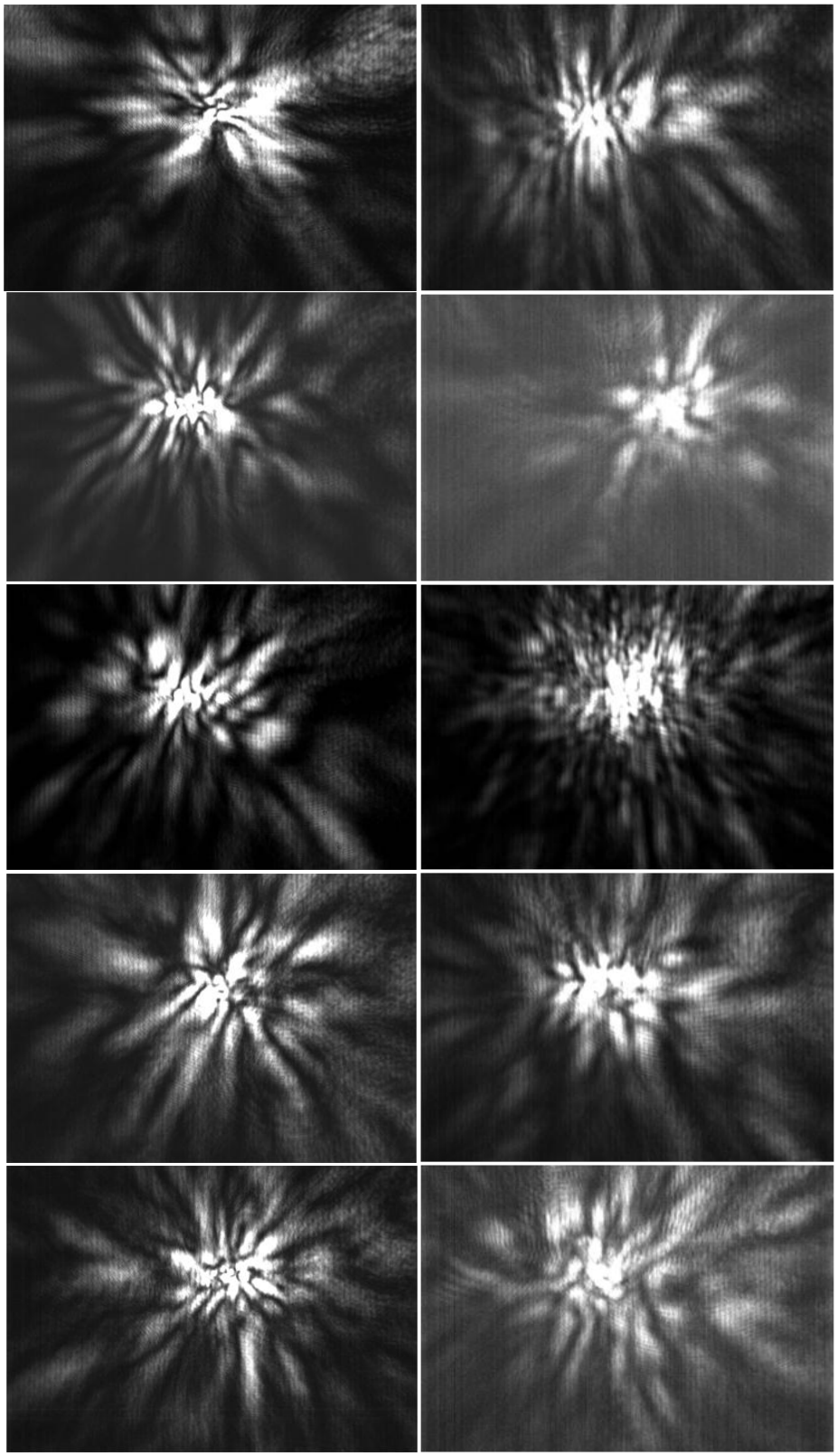

Fig. 5-12 Diffraction images of individual NALM-6 cells acquired with the wavelength of incident laser beam at 532nm.

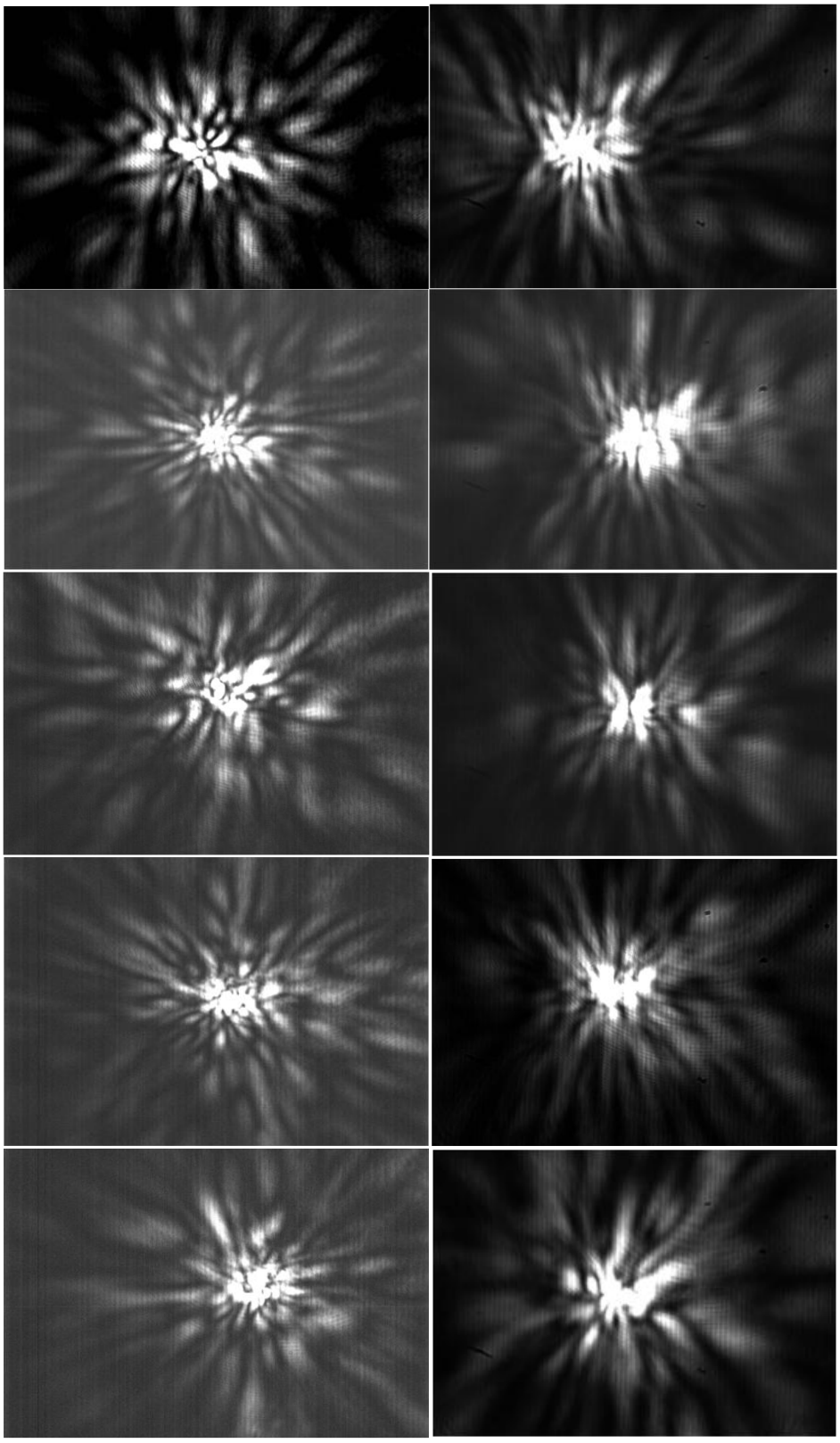

Fig. 5-13 Diffraction images of individual U-937 cells acquired with wavelength of incident laser at 532nm.

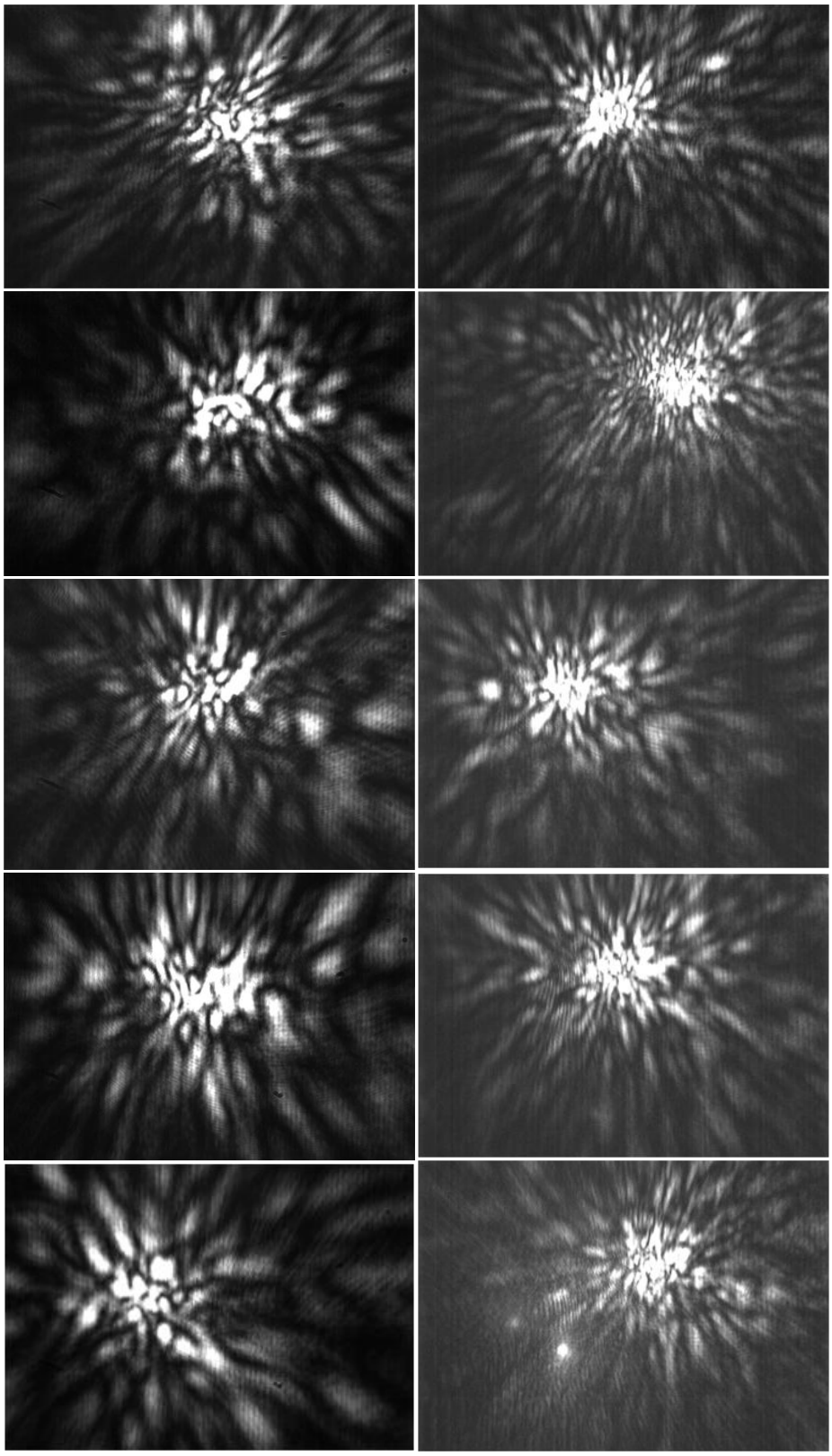

Fig. 5-14 Diffraction images of individual B16F-10 cells acquired with wavelength of incident laser at 532nm.

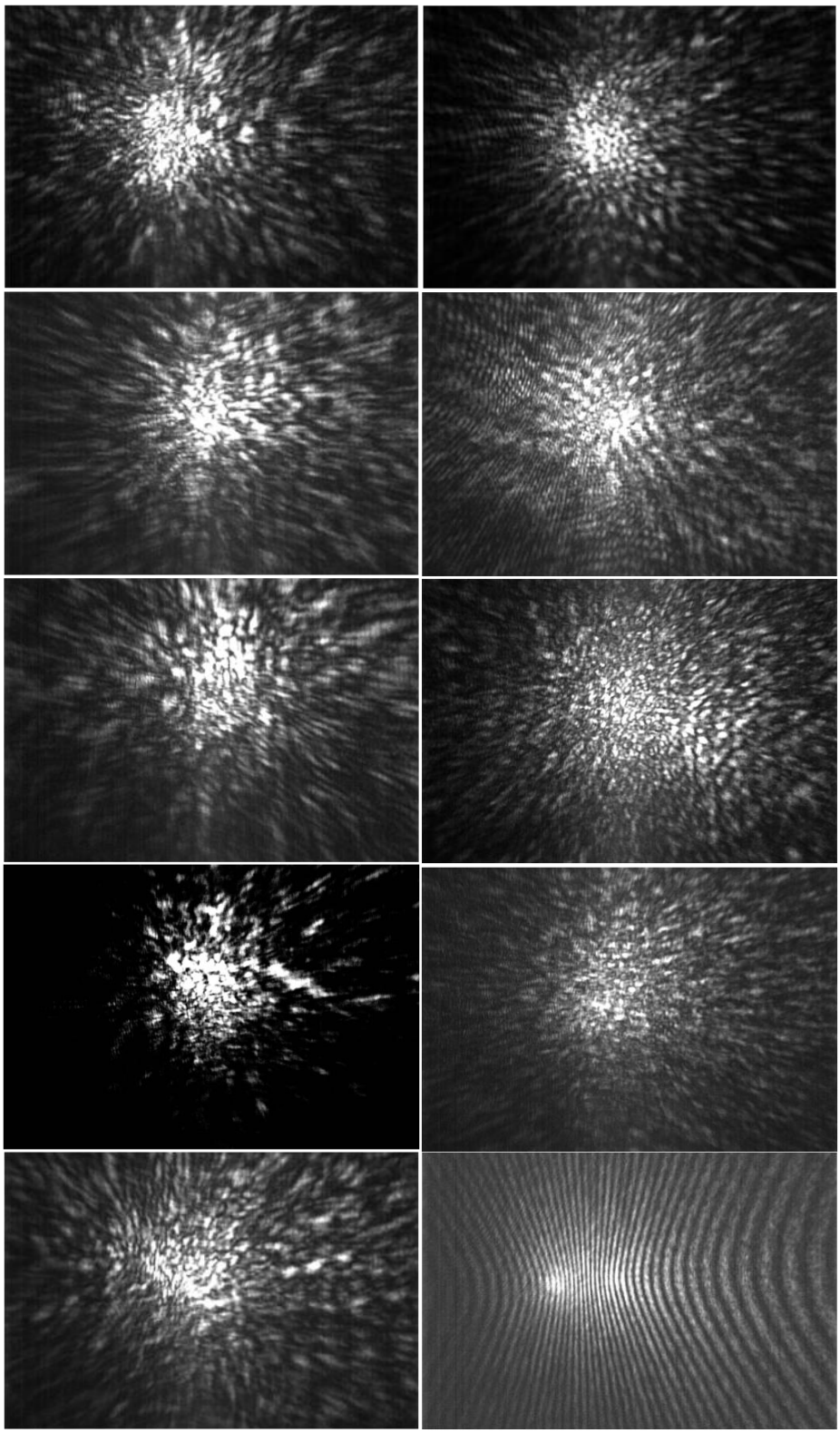

Fig. 5-15 Diffraction images of individual MCF-7 cells acquired with wavelength of incident laser at 532nm. Fig. 5-16 (Bottom right) A stray 25 μm sphere serves as calibration.

Human and machine pattern recognition

The purpose of this dissertation study is to acquire high contrast diffraction images from flowing particles with the goal of extracting useful morphological information. Beyond the cursory view and analysis applied to the preceding images it remains to consistently extract useful information from the diffraction images. One method is to develop machine operated pattern recognition algorithms and the other is human pattern recognition. Machine analysis is certainly the only option for processing image data from vast numbers of cells but implementing that goal is challenging. Note for example that even with the advanced image analysis algorithms available today nearly all routine pathology examination of tissue and blood smear slides is not accomplished automatically but manually by specialists. One reason is that digitizing a typical slide at resolutions sufficient for pathology examination requires 500 times the stored information as a typical camera photograph [Perkel 2010]. The other is that some human assessments still cannot be converted into a machine algorithm because even the most powerful computers are still not sophisticated enough in image analysis compared to the human brain. Both of these reasons are applicable to analyzing our diffraction images. These images are representations of a three dimensional object.

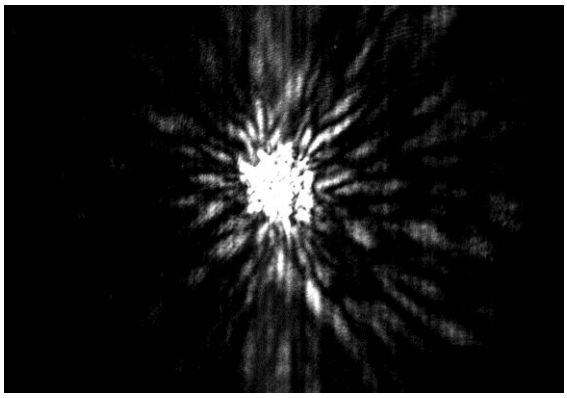

Fig. 5-17 MCF7 breast cancer cell in water at 2mm/s speed, 532nm wavelength excitation.

It is logical then that much more information is contained in a cells scatter than can be displayed in a typical 2 dimensional image format. In similar manner a detailed confocal image contains the information of several dozen 2 dimensional images. Also, development of pattern recognition algorithms is easier if it is known

what pattern is to be extracted and insight into algorithm development can come from human pattern recognition.

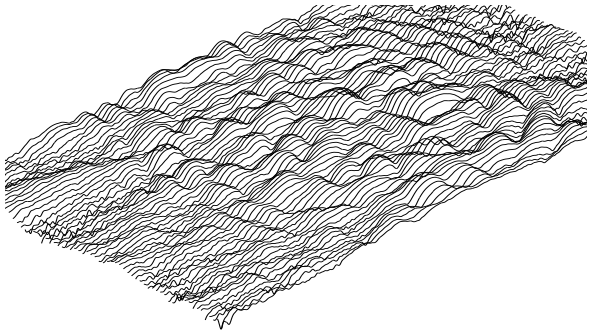

Fig. 5-18 Log plot of pixel values from part of Fig.5-17. It is 136 pixels wide by 240 pixels long, MCF-7 cells in water.

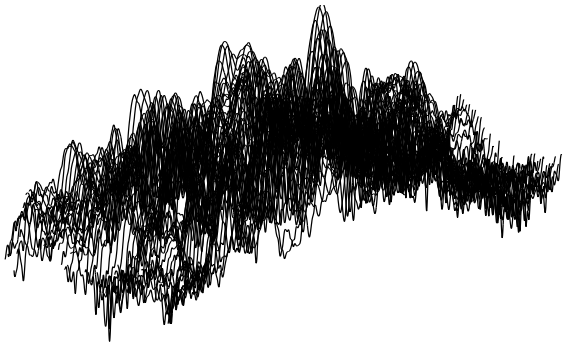

Fig. 5-19 Same as Figs. 5-17 and 5-18 but in a region of higher intensity variations, 120 pixels x 260 pixels long.

To illustrate the above arguments we start with an MCF-7 cell diffraction image moving slowly in water and imaged with the objective positioned at F+00 as presented in Fig. 5-17. At the F+00 position most image features are concentrated in a small region of FOV which was so chosen because the software used here can only process a limited number of pixels. We wish to display the image in such a way that human pattern recognition might readily pick out some significant repeating marker in the diffraction patterns to be then associated with a cell characteristic. The human eye cannot perceive all the gray scales in this image. However, display of the same image with a different gray-scale or contrast setting one can be observe some other features. But if the pixel values are displayed on the z axis of a three dimensional plot then the eye can pick out more information as in Fig. 5-18. This logarithmic plot is only a small region of Fig. 5-17 comprising 136x240 pixels. Note that more features can be recognized in this type of display. If however as shown in Fig. 5-19 the contrast is too large or the region selected contains too many pixels then the eye is rapidly confused as is apparent. In both of these plots a

background pixel value of 3400 was subtracted, every other curve was discarded and the remaining curves were fitted to a spline function to smooth the image.

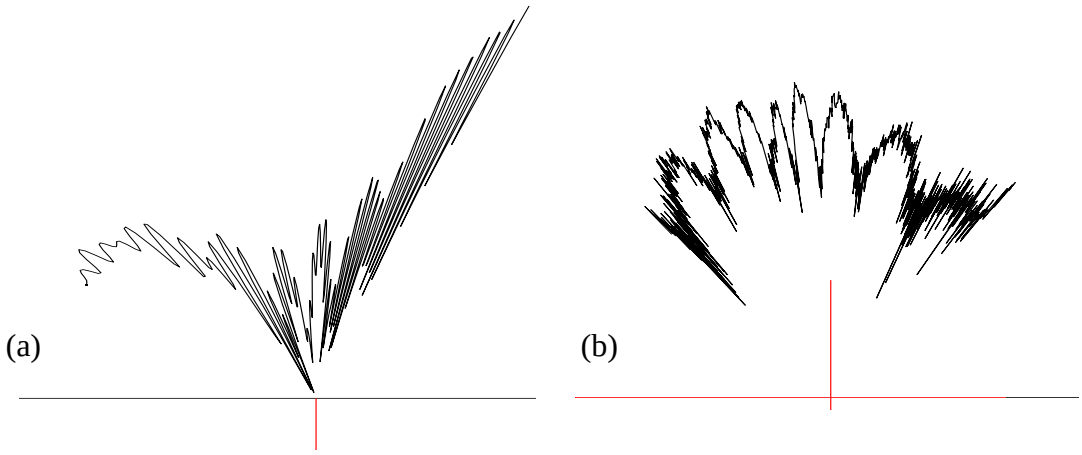

Fig. 5-20 Polar log plots, similar to Fig. 4-7, of 5μm polystyrene sphere scatter at 532 nm wavelength, unpolarized coherent excitation in water. Mie calculation plot (a) and measured (b) from our flow cytometer. Plots are side scatter fluence at equator from 60^o to 120^o. Vertical lines indicate sphere center.

Furthermore, there is apparently other noise in the images that can complicate the process of image analysis using machine algorithms. Two polar plots of the side scatter from a 5μm polystyrene sphere are presented in Fig. 5-20 for scattering angles ranging from 60^o to 120^o. The left is from the Mie theory based calculation and the right is the equator pixel value profile of a measured diffraction image from a flowing sphere in water. The polar plot is a more realistic representation of scatter signal. The xy plots in Figs. 5-18 and 5-19 are over a much smaller angular range (~ 5^o instead of 60^o) so Cartesian coordinates are adequate. A rapid drop off of fluence away from 90^o for the measured sphere (right plot) is a product of non-planar illumination cross section and uncertain lens effects. But the attention here is that by enlarging this plot it becomes apparent that the measured image has much higher spatial frequency components, presumably noise. Noise like this makes machine pattern recognition much more

difficult. This is another reason to assist development of machine pattern recognition with human pattern recognition.

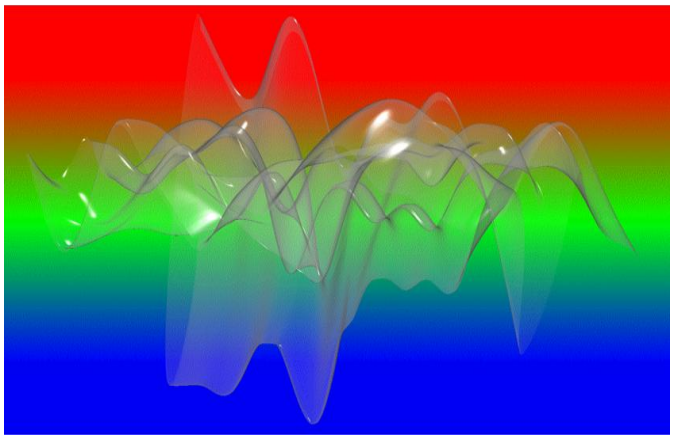

Fig. 5-21 Side view transparency rendering of a small region, 40x40 pixels, from Fig. 5-19.

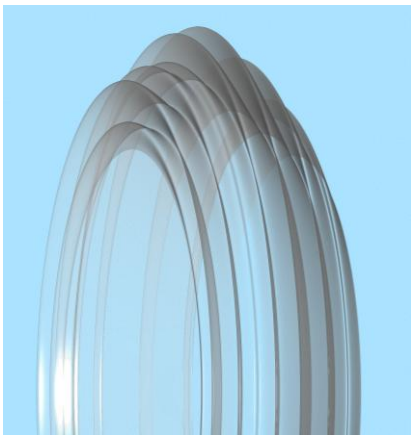

Fig. 5-22 Three dimensional rotation of left side of polar log Mie plot of Fig. 5-20.

Fig. 5-21 is a small region of Fig. 5-19, about 35 pixels square (or 4.4 microns square on the cell), made with computer assisted drawing (CAD) and is from the same perspective. The CAD software enlists artificial transparency, reflectivity, and refractive index of the modeled surface with a gradient color background to generate the rendered image. Its purpose is to give the eye cues to assist in untangling a complex image. The transparency attribute allows hidden forms to become apparent. A continuation of this display technique is seen in Fig. 5-22. Here the side scatter calculated with the Mie theory is presented in three-dimensions (both θ and ϕ directions) with θ from about 100^o to 120^o. Each lobe of Fig. 5-20(a) is seen as a rounded cone in Fig. 5-22. Although this conveys no more information than the two dimensional plot it is clear that if the diffraction image did not have axial symmetry, such as a cell, then this type of display would be much different. It would then appear as a series, such as in Fig. 5-21 but extending outward in every polar direction. The above is a more accurate and intuitive geometrical presentation of the scattering process. Image features in every polar direction θ, ϕ would be visible as a whole with r

proportional to the fluence value of scattered light. Therefore the small surface area of Fig. 5-21 would become part of the surface of a complete sphere representing all scattering of target cell as emanating from its center. This technique requires of course that scatter information is acquired from multiple viewpoints.

Summarizing our results presented in this chapter we can conclude that variations in cell diffraction images are correlated to the morphological differences that can be expected from differing cell lines. The correlation remains to be explored for cell classification at this point and no pattern features have been rigorously associated with cell lines but a clear potential is demonstrated. Also by improving on image display techniques we can expect to be able to readily notice cell differences from their diffraction images. In chapter 6 the plans for strengthening cell morphology analysis with diffraction images will be discussed.

Chapter 6 Summary and Future Research

§6.1 Summary

Through this dissertation study we have established the foundation for development of a new method for the rapid assay of large cell populations which is termed diffraction imaging flow cytometry [Jacobs, 2009a, Jacobs, 2009b]. In comparison to existing flow cytometry methods, the new method provides 2D image data that are highly correlated to the 3D morphologic features of biological cells. To achieve this goal, we have investigated issues of fluidics, microchannel fabrication, and optical imaging in addition to acquisition of diffraction images of microspheres and six types of cultured biological cells. Through a series of experiments on fluidics we were able to produce well focused laminar flow with core speed down to 1 mm/s and a core fluid diameter down to 15 microns, although smaller core and sheath fluids were subject to clogging. Several flow chamber designs were studied to reduce or eliminate optical noise associated with the index-mismatched chamber-sheath interface. The most promising was a square microchannel flow cell in PDMS and a three fluid submerged jet chamber. Both designs allow the elimination of the optical noise, yielding high-contrast diffraction images with low background. A microfluidic device fabrication technique, different from soft lithography, was successfully developed for constructing a tapered microchannel flow cell with optically flat surfaces. It is an inexpensive alternative to quartz flow cells. Methods for acquiring diffraction images with static spheres and cells that allow for extraction of features sensitively dependent on the imaged particle's morphology were also developed. Several immobilizing fluids were

investigated so that static images of cells clear of interfering surfaces could be used to anticipate imaging of flowing targets.

We have also performed detailed investigation on how to acquire diffraction images with a microscope objective that can exhibit high correlation to the 3D morphological features of the imaged particle instead of the imaging system itself. In previous reports, imaging sensors are placed directly against the flow chamber to detect directly the spatial distribution of scattered light. This approach allows direct comparison of measured image data with calculated ones, especially in the case of spheres where the Mie theory provides very accurate modeling results. However, several disadvantages exist for this approach. First, a separate microscope is often needed to align the incident laser beam and its focus on the core fluid and related imaging system. Second, direct placement of CCD sensor requires the sensor be placed very close to the flow chamber. The small separation makes it is very difficult to add optical elements such as wavelength filters or polarizers between the chamber and the sensor, which are needed for investigation of morphological features related to dispersion and polarization changes of the scattered light. In our imaging unit, we incorporated an infinity-corrected microscope objective of long working distance, whose output is focused to infinity or in parallel light beam form. The use of this objective enables us to combine the alignment of the flow chamber with the acquisition of diffraction images. This design has the benefit of easy incorporation of optical elements as needed. In results presented in Chapter 4, we have shown that the diffraction images should be acquired by translating the imaging unit from the focusing position obtained for non-diffraction imaging by about 100 to 200μm toward the chamber. This result [Jacobs, 2009a] is critical to obtain diffraction image data that are highly correlated to the 3D morphology of the

imaged particle with the objective that the images are particularly useful for investigation of highly unsymmetrical cell morphology.

Diffraction imaging studies were made of six cell lines. Differences between cell lines were obvious in most cases and less dramatic to visual observation in closely related types such as NALM-6 and Jurkat cells. These two cell types are derived from human B and T lymphocytes, respectively, and are expected to have similar morphology. In fact, even manual microscopic examination fails to separate T and B cells unless with they are stained with fluorescent antobodies. Many different variables enter into a diffraction image and elimination of instrument induced variations is critical. One induced variation could be eliminated by more accurate and rapid positioning of cells into the interrogation point by fluidics. Also the use of an objective lens to project a diffraction image of a 3D object into a camera CCD is not well understood. The distortions or artifacts due to the imaging system have required positioning the objective at de-focused locations as described earlier, which sacrifices much detected light intensity for high-contrast image data. However using a de-focused objective position does not dismiss the correctness or utility of images acquired at other objective positions but only means more study is needed for interpretation.

§6.2 Future Research

The series of experimental investigations carried out in this dissertation study yield a solid foundation for a new approach to rapidly analyze 3D morphology based features of large populations of biological cells and point to a clear direction of what can be done. The optical unit

of this instrument, supplied with a serial flow of cells from a fluidics unit, has yielded high contrast diffraction images containing much information about cell morphology. The limited camera sensitivity requires slow flow speed and sufficiently long exposure time, which has been kept at a minimum of 1 millisecond for nearly all of the results presented in this dissertation.

Several options are available to improve the optical unit. To increase cell throughput the excitation fluence would need to be increased up to the limits of cell heat damage, about a factor of ten. By increasing power further but expanding the beam diameter another major source of instrument induced image variability could be eliminated, which is image distortion due to cell positioning error within a non-uniform portion of the excitation beam intensity profile. A more sensitive, but expensive, camera, such as an intensified CCD, would permit faster image acquisition. Even with all the preceding improvements there are two optical issues that would still need to be addressed. One is our experimental result that the microscope objective must be translated 200μm toward cell from the non-coherent focus position to realize good agreement with Mie predicted diffraction images in the cases of spheres. This translation comes at the expense of a 90% reduction in light fluence. The second issue to address is the acquisition and display of the three dimensional diffraction scatter field on a two dimensional surface. A corollary to this latter issue is that, unless the camera and optics has infinite resolution, an increase in the number of cameras and solid angle intercepted θ, ϕ, will certainly increase the amount of cell morphology information available. And this information if displayed as a three dimensional surface corresponding to the three dimensional scatter intensity will be in a form more intuitive and transferable between similar instruments.

A possible way to address the above issues is an extension of previously tested instruments into three dimensions. The wavefront from an excited particle would be received by a spherically

arranged array of image conduits, a coherent fiber optic bundle, with one end pointed towards target cell and the other end directly touching a flat CCD chip. This duplicates optically in the three dimensions instruments already proven to work in two dimensions by Salzman, Bartholdi, and others [1975, 1980]. None of the distortions that we experienced in 3-dimensions were found in their two dimensional plots of sphere scatter. Therefore by using image conduits each with a concave ground surface facing the illuminated particle and positioned at the focal distance of the concave surface, the scatter wavefront in three dimensions is acquired. With the distortion eliminated the F+00 position can be used in turn to increase light gathered tenfold over the F+200 position. With a spherical array of 12 image conduits distributed around a fluidics supplied illuminated cell at its center and with the image conduits pentagonal in cross section 12 of them would close pack as a dodecahedron, intercepting 100% of the particle scatter. Side scatter gathered would be ten times greater than our present single-lens imaging configuration and forwardly scattered light would give even more information. Furthermore the image variations generated by particle orientation would be eliminated since all views of particle are gathered simultaneously. One of the intercepting solid angles would still be fitted with our present camera and optics for purposes of triggering, polarization, wavelength studies, and alignment. However, mounting polarizers or filters at the image conduit entrances would be complicated.

Another advantage of a spherical imaging flow chamber is that it readily lends itself to an intuitive and standardized graphical display of data. This display would be as a semitransparent object with spherical polar coordinates r,θ,ϕ in which r is cell scatter fluence and θ, ϕ are used to mark the angular positions of corresponding three dimensional camera pixel positions. Basics of this kind of display are shown in Figs. 5-21 and 5-22 in which all surfaces of a three dimensional

object including its back side are simultaneously apparent. Thus the angular orientation dependence of cell images is eliminated. The application of computerized pattern recognition to analysis of diffraction images could therefore begin with human pattern recognition applied to the images as the source of insight into what machine vision should be looking for.

Finally the fluidic unit that supplies targets in a focused stream for the optical unit also can be improved. The first issue is clogging of core feed tube by slow moving cells when feed tube is of diameter less than ten cell diameters. The diameter of feed tube from our experiments sets the lower limit on focused diameter of core stream. Therefore more careful experiments need to be done to determine the best factors to prevent particle adhesion to tube walls and particle clogging of the tubes entrance. A compact syringe pump for a fluid supply can be built incorporating what has been learned so far. Outside of these improvements more advanced flow techniques such as electrokinetically driven flows may enable the slow speed high focus necessary for consistent diffraction imaging [Dittrich 2007].

Appendix

Material	Properties
PDMS	n_{633}=1.406 n_{532}=1.411
Silicon Oil	n=1.404 viscosity = 10^6 cSt
Spheres	n=1.59 density = 1.05g/cm^3
KY gel	n=1.34
Clear shampoo	n=1.36
Glycerol solution 56%	n=1.406 viscosity = 6mPa s
Saline solution	n=1.3345

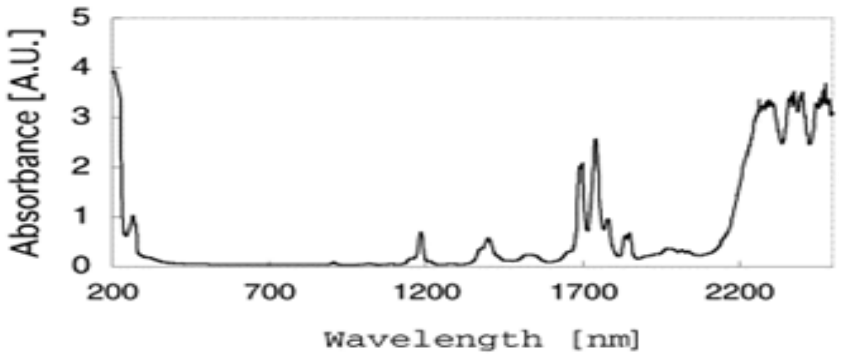

Figure 58 Optical properties of polydimethylsiloxane (PDMS)

REFERENCES

E. Andrade and L. Tsein, (1937) "The Velocity-Distribution in a Liquid-Into-Liquid Jet" Proc. Phys. Soc.**49**, 381-390.

K.B. Aptowicz, (2005) Angularly-Resolved Elastic Light Scattering of Micro-Particles Yale University PhD Dissertation.

J.A. Armstrong, (1956) "Histochemical Differentiation of Nucleic Acids by Means of Induced Fluorescence" Exptl. Cell Res. **11**, 640-643.

A. Ashkin and J. Dziedzic, (1981) "Observation of Optical Resonances of Dielectric Spheres by Light Scattering" Applied Optics **20** (10), 1803-1814.

M. Bartholdi, G. C. Salzman, R.D. Hiebert, and M. Kerker, (1980) "Differential Light Scattering Photometer for Rapid Analysis of Single Particles in Flow" Appl. Opt. A **91**, 1573-1581.

G.K. Batchelor , (1967) *An Introduction to Fluid Dynamics*. Cambridge University Press.

C.F. Bohren and D.R. Huffman, (1983) *Absorption and Scattering of Light by Small Particles* New York: John Wiley & Sons.

A.G. Borovoi, and E.I. Naata, (1998) "Scattering of Light by a Red Blood Cell" Journal of Medical Optics **3**, 364-372.

R. C. Braylon, N.A. Benson, V. Nourse, and H. S.Kruth, (1982) "Correlated Analysis of Cellular DNA Membrane Antigens and Light Scatter of Human Lymphoid Cells" Cytometry **2**, 337-343.

R.S. Brock, X.H. Hu, D.A. Weidner, J. R. Mourant, and J.Q.Lu, (2006) "Effect of Detailed Cell Structure on Light Scattering Distribution: FDTD Study of a B-cell with 3D Structure Constructed from Confocal Images", Journal of Quantitative Spectroscopy & Radiative Transfer **102**, 25-36.

A. Brunsting and P. F. Mullaney, (1972) "Light Scattering from Coated Spheres: Models for Biological Cells" Appl. Optics **11**, 675-680.

F. C. Cheong, B. Sun, R. Dreyfus, J. Amato-Grill, KeXiao, L. Dixon, and D. Grier, (2009) "Flow Visualization and Flow Cytometry with Holographic Video Microscopy" Optics Express **17** (15).

W. H. Coulter, (1949) "Means for Counting Particles Suspended in a Fluid" U.S. Patent 2,656,508 Issued October 20, 1953.

P. J. Crosland-Taylor, (1953) "A Device for Counting Small Particles Suspended in a Fluid Through a Tube" Nature **171**, 37 – 38.

R. Curbelo, E. Schildkraut, T. Hirschfeld, R. Webb, M. Block, H. Shapiro, (1976) "A Generalized Machine for Automated Flow Cytology System Design" J. Histochem. Cytochem. **24**, 388.

H. Davey and D. Kell, (1996) "Flow Cytometry and Cell Sorting of Heterogeneous Microbial Populations: the Importance of Single-Cell Analyses" Microbiological Reviews **60** (4), 641–696.

P. Dean, D. Pinkel, and M. Mendelsohn, (1978) "Hydrodynamic Orientation of Sperm Heads for Flow Cytometry" Biophysical Journal **23** (1), 7-13.

H. Ding, J.Q. Lu, W.A. Wooden, P.J. Kragel,and X.H. Hu, (2006) "Refractive Indices of Human Skin Tissues at Eight Wavelengths and Estimated Dispersion Relations between 300 and 1600 nm" Physics in Medicine and Biology **51,** 1479-1489.

P. S. Dittrich, F. Malik, and P. Schwille, (2007) *Microfluidic Technologies for Miniaturized Analysis Systems Chapter 14*, Springer US.

R. Drezek, A. Dunn, and R. Richards-Kortum, (1999) "Light Scattering from Cells: Finite-Difference Time-Domain Simulations and Goniometric Measurements". Applied Optics **38** (16), 3651-3661.

G. B. Dubelaar and P. L. Gerritzen, (2000) "CytoBuoy: a Step Forward Towards using Flow Cytometry in Operational Oceanography" Sci. Mar. **64**(2), 255-265.

W. Eisert, and M. Dennenloehr, (1981) "Nozzle Design for the Generation of Plane Liquid Surfaces" Cytometry **1** (4), 249-253.

F. C. Genter and G. C. Salzman, (1979) "A Statistical Approach to the Classification of Biological Cells from Their Diffraction Pattern." The Journal of Histochemistry and Cytochemistry" **27** (1), 268-272.

M. Hammer, D. Schweitzer, E. Michel, E. Thamm, and A. Kolb, (1998) "Single Scattering by Red Blood Cells" Applied Optics **37,** 7410-7418.

E. Hecht, and A. Zajac, (1987) *Optics* Reading, Mass., Addison-Wesley Pub. Co.

H. Hillborg, J. F. Ankner, U. W. Gedde, G. D. Smith, H. K. Yasuda and K. Wikström, (2000) "Crosslinked Polydimethylsiloxane Exposed to Oxygen Plasma Studied by Neutron Reflectometry and other Surface Specific Techniques" Polymer **41** (18), 6851-6863.

H. R. Hulett, W. A. Bonner, J. Barrett, and L. A. Herzenberg, (1969) "Cell Sorting: Automated Separation of Mammalian Cells as a Function of Intracellular Fluorescence". Science **166**, 747-749.

K. Jacobs, Q. Jun Lu, and Xin-Hua Hu, (2009a) “Development of a Diffraction Imaging Flow Cytometer” Opt. Lett. **34**, 2985-2987.

K. Jacobs , L.V. Yang , J. Ding , A. E. Ekpenyong, and R. Castellone, J. Q. Lu , X. H. Hu, (2009b) “Diffraction imaging of spheres and melanoma cells with a microscope objective” Journal of Biophotonics 2 (8-9), 521-527.

M. H. Julius, R. G. Sweet, C. G. Fathman, and L. A. Herzenberg, (1975) “Fluorescence-activated cell sorting and its applications” In: Richmond CR et al., ed. *Mammalian Cells: Probes and Problems*. Oak Ridge, Tenn., Technical Information Center

G. Karniadakis, and A. Beşkök, and N. R. Aluru, (2005) “Microflows and Nanoflows: Fundamentals and Simulation” Interdisciplinary Applied Mathematics **29.**

Y. L. Kim, Y. Liu, R. Wali, R. H. Goldberg, K. Alexey, C. K. Kromin, and V.Backman, (2003) “Simultaneous Measurement of Angular and Spectral Properties of Light Scattering for Characterization of Tissue Microarchitecture and Its Alteration in Early Precancer” IEEE Journal of Selected Topics in Quantum Electronics **9** (2).

R. E. Kopp, L.J. Mendelsohn, J.P. Pernick, B.Stone and H.R. Wohlers, (1976) “Coherent Optical Processing of Cervical Sytologic Samples” J. Histochem, Cytochem **24**, 122-137.

A. Kummrow, A. Theisen, J. Frankowski, M. Tuchscheerer, A. Yildirim, H. Brattke, K. Schmidt, and M. Neukammer, (2009) “Microfluidic Structures for Flow Cytometric Analysis of Hydrodynamically Focussed Blood Cells Fabricated by Ultraprecision Micromachining” Lab Chip **9**, (7), 972-981.

A.J. Lacey, (1999) *Light Microscopy in Biology: a Practical Approach* Oxford, England; New York, Oxford University Press.

P. Laven, (2003) “Simulation of Rainbows, Coronas, and Glories by use of Mie Theory” Applied Optics **42** (3), 436-444.

G. B. Lee and C. I. Hung, (2001) “Hydrodynamic Focusing for a Micromachined Flow Channel” Journal of Fluids Engineering **123**(3), 672-679.

S.S. Lee and S.I. Izuo, (2000) “A CAD Study on Micro Flow Cytometry and its Application to Bacteria Detection” Advanced Technology R&D Center, Mitsubishi Electric Corporation.

W. Y. Lee, D. S. Lim, S. H. Ko, Y. J. Park, K. S. Ryu, M. Y. Ahn, Y. R. Kim, D. W. Lee,and C.W. Cho, (2004) "Photoactivation of Pheophorbide A Induces a Mitochondrial-Mediated Apoptosis in Jurkat Leukaemia Cells" J Photochem Photobiol B **75**(3), 119-26.

B. Lewin, (2007) *Cells* Sudbury, Mass., Jones and Bartlett Publishers.

I. K. Ludlow and P. H. Kaye, (1979) "A Scanning Diffractometer for Rapid Analysis of Microparticles and Biological Cells" J. Colloid Interface Sci. **69,** 571-589.

M. R. Loken, R. G. Sweet, and L. A. Herzenberger, (1976) "Cell Discrimination by Multiangle Light Scattering" J. Histochem. Cytochem. **24,** 284-291.

I.K. Ludlow, and P. H. Kaye, (1979) "A High Speed Laser Diffractometer" J.Phys. Instrum. **12**, 690-693.

J. Q. Lu, P. Yang, and X. H. Hu, (2005) "Simulations of Light Scattering from a Biconcave Red Blood Cell using the FDTD Method" Journal of Biomedical Optics **10**, 024022.

J. Maddox, (1994) "Towards More Measurement in Biology" Nature **368**, 95.

V. P. Maltsev, (2000) "Scanning Flow Cytometry for Individual Particle Analysis." Review of Scientific Instruments **71**(1), 243-255.

M. R. Melamed, and T. Lindmo, (1990) *Flow Cytometry and Sorting* New York, Wiley-Liss: xii, 824.

G. Mie, (1908) "Beiträge Zur Optik Trüber Medien Speziell Kolloidaler Metallösungen" Ann. Phys. **25**, 377- 445.

I. N. Milosevic and E. K. Longmire, (2002) "Pinch-off Modes and Satellite Formation in Liquid/Liquid Jet Systems" International Journal of Multiphase Flow **28.**

J. R. Mourant, (1998) "Mechanisms of Light Scattering from Biological Cells Relevant to Noninvasive Optical-Tissue Diagnostics" Applied Optics **37**, 3586.

J. R. Mourant, and M. Canpolat, (2000) "Light Scattering From Cells: the Contribution of the Nucleus and the Effects of Proliferative Status." Journal of Biomedical Optics **5**, 131-137.

P. F. Mullaney, V. Dilla, M.A. Coulter, and J.R. Dean, (1969) "Cell Sizing: a Light Scattering Photometer for Rapid Volume Determination" Rev. Sci. Instrum. **40** (8),1029-1032.

J. Neukammer, C. A. Gohlke, A. Höpe, T.Wessel, and H. Rinneberg, (2003) "Angular Distribution of Light Scattered by Single Biological Cells and Oriented Particle Agglomerates" Appl. Opt. **42**, 6388-6397.

N. Guyen, Nam-Trung, (2008) *Fundamentals and Applications of Microfluidics* Artech House Microelectromechanical Systems Library.

S. H. Ong, D. Horne, C. Yeung, and P. Nickolls, (1987) "Development of an Imaging Flow Cytometer". Analyt. and Quant. Cyt. and Hist. **9** (5), 375-382.

E. Ortyn, D. Perry, V. Venkatachalam, L. Liang, B. Hall, K. Frost, and D. Basiji, (2007) "Extended Depth of Field Imaging for High Speed Cell Analysis" Cytometry **71A**, 215-231.

D.A. Ortyn,W.E. LiangL, V.Venkatachalam, and P. Morrissey, (2007) "Cellular Image Analysis and Imaging by Flow Cytometry" Clinics in Laboratory Medicine **27**, 653-670.

B. Orvyn, and S. Izen, (2000) Imaging of Transparent Spheres Through a Planar Interface Using a High-Numerical-Aperture Optical Microscope" JOSA A, **17** (7), 1202-1213.

J. Perkel, (2010) "Digitizing Pathology" Bioscience Technology **34** (2), 1-12.

B. Pernick, M. R. Wohlers, and J. Mendelsohn, (1978) "Paraxial Analysis of Light Scattering by Biological Cells in a Flow System" Appl. Optics **17**: 3205-3215.

D. Phillips, P. Wyatt, and R. Berkman, (1970) "Measurement of the Lorenz-Mie Scattering of a Single Particle" Journal of Colloid and Interface Science **34** (1), 159-162.

C. Pinkel, S. Lake, B. Gledhill, M.Van Dilla, D. Stephenson, and D. Watchmaker, (1982) "High Resolution DNA Content Measurements of Mammalian Sperm" Cytometry **3**(1),1-9.

C.Pnueli and C. Gutfinger, (1992) *Fluid Mechanics*, Cambridge University Press.

L. Prandtl, and O. Tietjens, (1934) *Applied Hydro- and Aero-Mechanics* New York: McGraw-Hill Book Co., Inc.

G. W. Rankin, K. Sridhar, M. Arulraja, and K. R. Kumar, (1983) "An Experimental Investigation of Laminar Axisymmetric Submerged Jets" J. Fluid Mech. **133,** 217-223.

J. R. Richards, (1994) *Fluid Mechanics of Liquid-Liquid Systems* PhD Dissertation, University of Delaware.

M. Rozycka, S. Lenczowski, W. Sawicki, W. Baranska, and K. Ostrowski, (1982) "Optical Diffraction as a Tool for Semiautomatic, Quantitative Analysis of Tissue Specimens" Cytometry **2**, 244-248.

G.C. Salzman, S. B. Singham, R. G. Johnston, and C. F. Bohren, (1990) "Light Scattering and Cytometry". *Flow Cytometry and Sorting*, Second Edition, pages 81-107. Wiley-Liss, Inc.

G. C.Salzman, J. M. Crowell, C. A. Goad, K. M. Hansen, R. D. Hieert,and P. M. LaBauve, J. C. Martin, M. Ingram, and P. F. Mullaney, (1975) "A Flow-System Multiangle Light Scattering Instrument for Cell Characterization" Clin. Chem. **21**, 1297-1304.

W.Sawicki, W.Baranska, and K.Ostrowski, (1982) "Optical Diffraction as a Tool for Semiautomatic, Quanitative Analysis of Tissue Specimens" Cytometry **2**, 244-248.

L. Schiller, (1922) ForschArb. Ver. Dtsch. Ing. No.248.

H. Schlichting, and K.Gerstan, (2000) *Boundary-Layer Theory* McGraw Hill, New York, 8th ed.

W. Schneider, (1984) "Decay of Momentum Flux in Submerged Jets" J. Fluid Mech. **54** 91-110.

W. H. Schuette, and E. Carduccu, (1985) "The Relationship Between Mean Channel Selection and the Calculated Coefficient of Variation" Cytometry Technical note **6**, 487-491.

W. H. Schuette, S. E. Shackney, F.A. Plowmam, H. W. Tipton, C. A Smith, and M. A. MacCollum , (1984) "Design of Flow Chamber with Electronic Cell Volume Capability and Light Detection Optics for Multilaser Flow Cytometry" Cytometry **5,** 652-656.

G. Seger, M. Achatz, H. Heinze, and F. Sinsel, (1977) "Quantitative Extraction of Morphological Cell Parameters From the Diffraction Pattern", J. Histochem. Cytochem. **25**, 707-718.

H. M. Shapiro, S. D. Bryan, L.E. Lipkin, P. G.Stein, and P. F. Lemkin, (1971) "Computer-Aided Micro Spectro Photometry of Biological Specimens" Exp Cell Res. **67**, 81-9.

H. M.Shapiro, (1985) *Practical Flow Cytometry* New York, N.Y.

H.Steen, andT.Lindmo, (1985) "Differential of Light Scattering Detection in an Arc-Lamp-Based Epi-Illumination Flow Cytometer" Cytometry **6**, 281-285.

P. G. Stein, L. E. Lipkin, and H. M. Shapiro, (1969) "Spectre II: General-Purpose Microscope Input for a Computer" Science **166**, 328

J. A. Steinkamp, M. J. Fulwyler, J. R. Coulter, R. D. Hiebert. J. L.Horney, and P. F.Mullaney, (1973) "A New Multiparameter Separator for Microscopic Particles and Biological Cells" Rev. Sci. Instr. **44**, 1301-1310.

T. R. Stovel, L.A. Herzenberg, and R. G. Sweet, (1978)"A Means for Orienting Flat Cells in Flow Systems" Biophys J. **23**(1) 1–5.

Xuan-Tao Su, and K. Singh, (2008) "Measurements of Light Scattering in an Integrated Microfluidic Waveguide Cytometer" J. Biomed. Opt. **13** (2), 4024.

Xuan-Tao Su, K. Singh, W. Rozmus, C. Backhouse, and C. Capjack, (2009) "Light Scattering Characterization of Mitochondrial Aggregation in Single Cells" Optics Express **17,** (16).

N. Sundararajan, M. Pio, L. Lee and A. Berlin, (2004) "Three Dimensional Hydrodynamic Focusing on PDMS Microchannels" J. Microelectomechanical Systems **13** (4), 2004.

.

M. V. Dilla, P. Dean, O. Laerum, and M. Melamed, (1985) *Flow Cytometry: Instrumentation and Data Analysis* Academic Press.

B. Vempati, M. V. Panchagnula, A.Oztekin, and S. Neti, (2007) "Numerical Investigation of Coaxial Liquid-Liquid Flows." ASME Journal of Fluids Engineering **129**, 713-719.

J. Visser, V.Engh, G.J.Van, and C. W.Bekkum, (1980) "Light Scattering Properties of Murine Hemopoietic Cells" Blood Cell **6**, 391-407.

Z. Wang, J. El-Ali, M. Engelund, T. Gotsæd, I. Perch-Nielsen, K. Mogensen, D. Snakenborg, J. Kutter, and A. Wolff, (2004) "Measurements of Scattered Light on a Microchip Flow Cytometer with Integrated Polymer Based Optical Elements" Lab Chip **4**, 372-377.

T. Ward, M. Faivre, M. Abkarian, and H. Stone, (2005) "Microfluidic Flow Focusing: Drop Size and Scaling in Pressure versus Flow-Rate-Driven Pumping" Electrophoresis **26,** 3716-3724.

J. Wilson, (2007) *Measurements and Interpretations of Light Scattering from Intact Biological Cells* PhD Dissertation, University of Rochester.

J. Wilson, C. Bigelow, D. Calkins, and T. Foster, (2005) “Light Scattering from Intact Cells Reports Oxidative-Stress-Induced Mitochondrial Swelling” Biophysical Journal **88,** 2929-2938.

S. Yang and W. H. Hseih, (2007) “Hydrodynamic Focusing Investigation in a Micro-Flow Cytometer” Biomedical Microdevices **9**, 113-122.

K. S. Yee, (1966) “Numerical Solution of Initial Boundary Value Problems Involving Maxwell's Equations in Isotropic Media” IEEE Transactions on Antennas and Propagation **14**, 302- 307.

A. Yu, C. Lau, J. Tunnell, M. Hunter, M.Kalashnilov, C. Fang-Yen, S. Fulghum, K. Badizadegan, K, D. Ramachandra, and M. Feld, (2006) “Assessing Epithelial Cell Nuclear Morphology by Using Azimuthal Light Scattering Spectroscopy” Optics Letters **31** (21), 3119-3121.

G. Zabow, (2001) “Guided Microfluidics by Electromagnetic Capillary Focusing.” Applied Physics Letters **80**(8), 1483-1485.